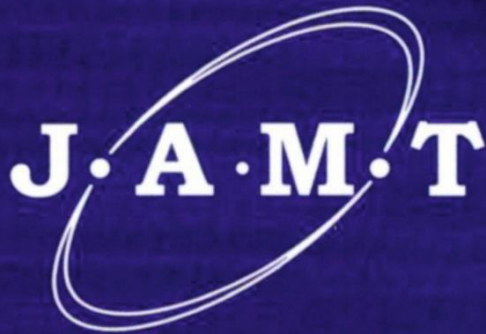


ISSN 2782-2192 (Print)

ISSN 2782-2206 (Online)

Journal of Advanced Materials and Technologies

J·A·M·T



**Vol. 9, No. 3.
2024**



ISSN 2782-2192 (Print)
ISSN 2782-2206 (Online)
DOI: 10.17277/issn.2782-2192



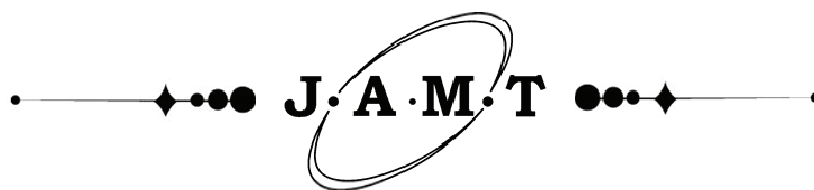
Journal of Advanced Materials and Technologies

**Vol. 9, No. 3.
2024**

**Том 9, № 3
2024**

16+

© Tambov State Technical University, Tambov, Russian Federation, 2024
© Merzhanov Institute of Structural Macrokinetics and Materials Sciences of Russian Academy of Sciences,
Chernogolovka, Moscow region, Russian Federation, 2024
© Design by TSTU Publishing, 2024



Journal of Advanced Materials and Technologies

Scientific Journal

“**Journal of Advanced Materials and Technologies**” is a peer-reviewed scientific journal of research in materials science and related issues in materials physics and mechanics.

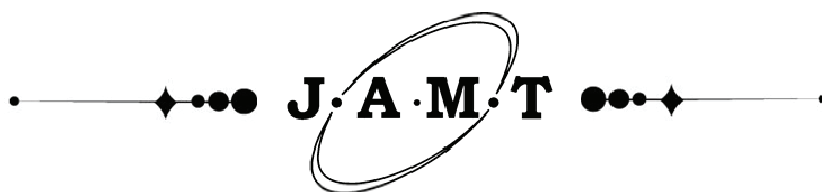
“**Journal of Advanced Materials and Technologies**” publishes original articles, reviews, short reports written by both renowned scientists and young researchers that contribute to the development of modern materials science.

The journal promotes research and exchange of information in the field of theoretical and practical research into materials science, modeling of processes involved in the creation of new materials, including nanomaterials, their properties and application.

The journal papers and metadata are available at Chemical Abstracts, CAS (American Chemical Society), Google Scholar, WorldCat, ROAR (Registry of Open Access Repositories), OpenAIRE (OpenAIRE - Open Access Infrastructure for Research in Europe), BASE (Bielefeld Academic Search Engine), RePEc: Research Papers in Economics, EBSCO.

ISSN 2782-2192 (Print), ISSN 2782-2206 (Online)

<i>Rename information</i>	Advanced materials & technologies (2016-2021) Print ISSN 2414-4606, Online ISSN 2541-8513
<i>The journal was founded</i>	2016
<i>Publication frequency</i>	Quarterly
<i>Founders</i>	Tambov State Technical University (TSTU), Merzhanov Institute of Structural Macrokinetics and Materials Sciences of Russian Academy of Sciences (ISMAN)
<i>Postal address</i>	TSTU: Bld. 2, 106/5, Sovetskaya St., Tambov, 392000 ISMAN: 8, Academician Osipyan St., Moscow region, Chernogolovka, 142432
<i>Editorial office address</i>	Bld. 2, 106/5, Sovetskaya St., Tambov, 392000
<i>Contacts</i>	Phone + 7 4752 63 03 91; amt.journal@yandex.ru
<i>Printing House</i>	TSTU Publishing, 112A, Michurinskaya St., Tambov, 392032 Phone + 7 4752 63 03 91; + 7 4752 63 07 46
<i>Website</i>	http://amt.tstu.ru/
<i>E-mail</i>	amt.journal@yandex.ru
<i>Phone</i>	+7 4752 63 92 93
<i>Subscription</i>	The electronic version of the Journal is freely available on the journal’s website, as well as in open access databases. The subscription index for the Journal printed version in the unified catalog “Press of Russia” is 80453
<i>Editor-in-Chief</i>	Mikhail I. Alymov, D. Sc. (Engineering), Professor, Corresponding Member of the Russian Academy of Sciences



Journal of Advanced Materials and Technologies

Научный журнал

«Journal of Advanced Materials and Technologies» – научный рецензируемый журнал, посвященный исследованиям в области материаловедения и примыкающих вопросов физики и механики материалов.

Журнал «Journal of Advanced Materials and Technologies» публикует оригинальные статьи, обзоры, краткие сообщения, содействующие развитию современной науки о материалах, подготовленные как известными учеными, так и молодыми специалистами.

Миссия журнала – обмен актуальной научной информацией в области теоретических и практических исследований и моделирования процессов, связанных с получением, определением свойств новых материалов, в том числе наноразмерных, и их применения.

Средство массовой информации периодическое печатное издание, журнал «Journal of Advanced Materials and Technologies» зарегистрировано Федеральной службой по надзору в сфере связи, информационных технологий и массовых коммуникаций. Регистрационный номер СМИ ПИ № ФС 77-74804 от 25.01.2019.

Журнал входит в перечень рецензируемых научных изданий (перечень ВАК Минобрнауки РФ) от 16 декабря 2021 г. по научным специальностям: 1.4.15 – Химия твердого тела; 2.6.6 – Нанотехнологии и наноматериалы; 2.6.13 – Процессы и аппараты химических технологий; 2.6.17 – Материаловедение.

Материалы журнала размещены в РИНЦ, Chemical Abstracts, CAS (American Chemical Society), Академия Google (Google Scholar), WorldCat, СОЦИОНЕТ, ROAR (Registry of Open Access Repositories), OpenAIRE (OpenAIRE - Open Access Infrastructure for Research in Europe), BASE (Bielefeld Academic Search Engine), RePEc: Research Papers in Economics, EBSCO.

ISSN 2782-2192 (Print), ISSN 2782-2206 (Online)

Сведения о переименовании	«Advanced materials & technologies» (2016–2021) Print ISSN 2414-4606, Online ISSN 2541-8513
Журнал основан	2016 г.
Периодичность	4 раза в год
Учредители	Федеральное государственное бюджетное образовательное учреждение высшего образования «Тамбовский государственный технический университет» (ФГБОУ ВО «ТГТУ»), Федеральное государственное бюджетное учреждение науки Институт структурной макрокинетики и проблем материаловедения им. А. Г. Мерджанова Российской академии наук (ИСМАН)
Адреса учредителей	ФГБОУ ВО «ТГТУ»: 392000, Тамбовская область, г.о. город Тамбов, г. Тамбов, ул. Советская, д. 106/5, помещ. 2, ИСМАН: 142432, Московская область, г. Черноголовка, ул. Академика Осипьяна, д. 8
Адрес издателя	ФГБОУ ВО «ТГТУ»: 392000, Тамбовская область, г.о. город Тамбов, г. Тамбов, ул. Советская, д. 106/5, помещ. 2
Адрес редакции	392000, Тамбовская область, г.о. город Тамбов, г. Тамбов, ул. Советская, д. 106/5, помещ. 2
Контакты	Тел.: + 7 4752 63 03 91; amt.journal@yandex.ru
Адрес типографии	392032, Тамбовская обл., г. Тамбов, ул. Мичуринская, д. 112А Тел.: + 7 4752 63 03 91; + 7 4752 63 07 46
Сайт	http://amt.tstu.ru/
E-mail	amt.journal@yandex.ru
Телефон	+7 4752 63 92 93
Подписка	Подписку на печатную версию журнала можно оформить по объединенному каталогу «Пресса России». Подписной индекс – 80453
Главный редактор	Алымов Михаил Иванович, д. т. н., профессор, член-корреспондент РАН

EDITORS

- Mikhail I. Alymov**, D. Sc. (Eng.), Professor, Corresponding Member of the Russian Academy of Sciences (RAS), Director of Merzhanov Institute of Structural Macrokinetics and Materials Sciences RAS (ISMAN), Chernogolovka, Moscow Region, Russian Federation
- Mikhail N. Krasnyansky**, D. Sc. (Eng.), Professor, Rector of Tambov State Technical University (TSTU), Tambov, Russian Federation
- Alexey G. Tkachev**, D. Sc. (Eng.), Professor, Head of Department of Technologies and Methods of Nanoproducts Manufacturing, TSTU, Tambov, Russian Federation
- Irina V. Burakova**, Ph.D., Associate Professor of Department of Technologies and Methods of Nanoproducts Manufacturing, TSTU, Tambov, Russian Federation
- Imran Ali**, Ph.D., FRSC, Professor, Department of Chemistry, Jamia Millia Islamia (Central University), New Delhi, India
- Vyacheslav M. Buznik**, D. Sc. (Chem.), Professor, RAS Academician, All-Russian Scientific Research Institute of Aviation Materials, Moscow, Russian Federation
- Stepan N. Kalmykov**, D. Sc. (Chem.), Professor, RAS Academician, Dean of the Faculty of Chemistry at the Lomonosov Moscow State University, Moscow, Russian Federation
- Valeriy P. Meshalkin**, D. Sc. (Eng.), Professor, RAS Academician, Head of Department of Logistics and Economic Informatics, Mendeleev University of Chemical Technology of Russia, Moscow, Russian Federation
- Tatyana P. Dyachkova**, D. Sc. (Chem.), Professor, Director of Center for Collective Use of Scientific Equipment “Production and Application of Multifunctional Nanomaterials”, TSTU, Tambov, Russian Federation
- Jesus Iniesta Valcarcel**, Ph.D., Associate Professor, Department of Physical Chemistry, University of Alicante, Alicante, Spain
- Rami J. Sldozian**, PhD, Lecturer at the Department of Applied Science, University of Technology, Baghdad, Iraq
- Ruslan Kh. Khamizov**, D. Sc. (Chem.), Professor, Director of Vernadsky Institute of Geochemistry and Analytical Chemistry of RAS, Moscow, Russian Federation
- Mikhail L. Kheifetz**, D. Sc. (Eng.), Professor, Director of Institute of Applied Physics of National Academy of Science of Belarus, Minsk, Belarus
- Roman B. Morgunov**, D. Sc. (Phys. and Math.), Professor, Leading Researcher, Institute of Problems of Chemical Physics RAS, Chernogolovka, Moscow Region, Russian Federation
- Fadei F. Komarov**, D. Sc. (Phys. and Math.), Professor, Academician of the National Academy of Sciences of Belarus, Head of Elionics Laboratory at A. N. Sevchenko Institute of Applied Physical Problems of Belarusian State University, Minsk, Belarus
- Stephane Mangin**, Ph.D., Professor, Physics of Matter and Materials Department, Institute Jean Lamour, University of Lorraine, Nancy, France
- Vladimir F. Pershin**, D. Sc. (Eng.), Professor, Professor at the Department of Technologies and Methods of Nanoproducts Manufacturing, TSTU, Tambov, Russian Federation
- Dimiter Stavrev**, D. Sc. (Eng.), Professor, Professor of Department of Materials Science at the Technical University of Varna, Varna, Bulgaria
- Alexander M. Stolin**, D. Sc. (Phys. and Math.), Professor, Head of Laboratory, ISMAN RAS, Chernogolovka, Moscow Region, Russian Federation
- Yoshifumi Tanimoto**, Ph.D., Professor, Hiroshima University, Japan
- Vener A. Valitov**, D. Sc. (Eng.), Leading Researcher, Institute for Metals Superplasticity Problems of the Russian Academy of Sciences, Ufa, Russian Federation
- Sergey M. Arakelian**, D. Sc. (Phys. and Math.), Professor, Head of the Department of Physics and Applied Mathematics, Vladimir State University, Vladimir, Russian Federation
- Arif A. Babaev**, D. Sc. (Phys. and Math.), Professor, Head of the Laboratory of Optical Phenomena in Condensed Matter, Institute of Physics of Dagestan Scientific Center of Russian Academy of Sciences, Makhachkala, Republic of Dagestan, Russian Federation
- Evgeniy I. Terukov**, D. Sc. (Eng.), Professor, Deputy Director for Science of R&D Center of Thin-Film Technology for Energetics under Ioffe Institute, St. Petersburg, Russian Federation
- Valeriy Yu. Dolmatov**, D. Sc. (Eng.), Head of Research Laboratory at the “Special Construction and Technology Bureau “Technolog”, St. Petersburg, Russian Federation
- Valeriy V. Savin**, D. Sc. (Phys. and Math.), Leading Researcher, Head of the Laboratory of Physical Materials Science, International Research Center “X-ray Coherent Optics”, Immanuel Kant Baltic Federal University, Kaliningrad, Russian Federation
- Gennady E. Selyutin**, Ph.D., Associate Professor, Senior Researcher, Federal Research Center “Krasnoyarsk Science Center” of Siberian Branch of the Russian Academy of Sciences, Krasnoyarsk, Russian Federation
- Vladimir V. Petrov**, D. Sc. (Phys. and Math.), Professor, Saratov State University, Saratov, Russian Federation
- Yury E. Kalinin**, D. Sc. (Phys. and Math.), Professor, Voronezh State Technical University, Voronezh, Russian Federation
- Vladimir S. Sevostyanov**, D. Sc. (Eng.), Professor, Head of the Department “Technological Complexes, Machines and Mechanisms”, V. G. Shukhov Belgorod State Technological University, Belgorod, Russian Federation
- Victor M. Mukhin**, D. Sc. (Eng.), Professor, D. Mendeleev University of Chemical Technology of Russia, Moscow, Russian Federation
- Vladimir D. Vermel**, D. Sc. (Eng.), Professor, Head of the Scientific and Technical Center of the Scientific and Production Complex, Central Aerohydrodynamic Institute, Zhukovsky, Moscow Region, Russian Federation
- Nadezhda V. Usoltseva**, D. Sc. (Chem.), Professor, Director of the Research Institute of Nanomaterials, Ivanovo State University, Ivanovo, Russian Federation
- Lyaylya A. Abdrahmanova**, D. Sc. (Eng.), Professor, Kazan State University of Architecture and Engineering, Kazan, Russian Federation
- Vyacheslav A. Sergeev**, D. Sc. (Eng.), Professor, Director of the Ulyanovsk branch of Kotelnikov Institute of Radioengineering and Electronics of Russian Academy of Science, Ulyanovsk, Russian Federation
- Irina V. Zaporotzkova**, D. Sc. (Phys. and Math.), Professor, Director of the Institute of Priority Technologies, Volgograd State University, Volgograd, Russian Federation
- Vladimir E. Guterma**n, Ph.D., Professor, Leading Researcher, Southern Federal University, Rostov-on-Don, Russian Federation
- Valeria S. Tafintseva**, Ph.D., Researcher, Department of Physics, Faculty of Science and Engineering, Norwegian University of Life Sciences, Norway
- Vyacheslav M. Tyutyunik**, D. Sc. (Eng.), Professor, Director General of International Nobel Information Centre (INIC), Ltd., TSTU, Tambov, Russian Federation
- Translator:** Natalia A. Gunina, Ph.D., Associate Professor, Head of Department of International Professional and Scientific Communication, TSTU, Tambov, Russian Federation

СОВЕТ РЕДАКТОРОВ

- Альмов Михаил Иванович**, д.т.н., профессор, член-корреспондент РАН, директор Института структурной макрокинетики и материалаоведения им. А.Г. Мерджанова РАН (ИСМАН), Черноголовка, Московская область, Россия
- Краснянский Михаил Николаевич**, д.т.н., профессор, ректор, Тамбовский государственный технический университет (ТГТУ), Тамбов, Россия
- Ткачев Алексей Григорьевич**, д.т.н., профессор, заведующий кафедрой «Техника и технологии производства нанопроductов», ТГТУ, Тамбов, Россия
- Буракова Ирина Владимировна**, к.т.н., доцент, доцент кафедры «Техника и технологии производства нанопроductов», ТГТУ, Тамбов, Россия
- Али Иман**, PhD, FRSC, профессор кафедры химии, Джамяя Миллия Исламия (Центральный университет), Нью-Дели, Индия
- Бузник Вячеслав Михайлович**, д.х.н., профессор, академик РАН, Всероссийский научно-исследовательский институт авиационных материалов, Москва, Россия
- Калмыков Степан Николаевич**, д.х.н., профессор, академик РАН, декан химического факультета Московского государственного университета им. М. В. Ломоносова, Москва, Россия
- Мешалкин Валерий Павлович**, д.т.н., профессор, академик РАН, заведующий кафедрой «Логистики и экономической информатики» Российского химико-технологического университета им. Д. И. Менделеева, Москва, Россия
- Дьячкова Татьяна Петровна**, д.х.н., профессор, директор центра коллективного пользования научным оборудованием «Получение и применение полифункциональных наноматериалов», ТГТУ, Тамбов, Россия
- Иньеста Хесус Валькарсель**, Ph.D., доцент кафедры физической химии Университета Аликанте, Аликанте, Испания
- Слдоэьян Рами Джозеф**, к.т.н., преподаватель кафедры прикладных наук, Технологический университет, Багдад, Ирак
- Хамизов Руслан Хажсетович**, д.х.н., профессор, директор, Институт геохимии и аналитической химии им. В. И. Вернадского РАН, Москва, Россия
- Хейфец Михаил Львович**, д.т.н., профессор, директор института, Институт прикладной физики НАН Беларуси, Минск, Беларусь
- Морзунов Роман Борисович**, д.ф.-м.н., профессор, главный научный сотрудник, Институт проблем химической физики РАН, г. Черноголовка, Московская область, Россия
- Комаров Фадей Фадеевич**, д.ф.-м.н., профессор, академик Национальной академии наук Республики Беларусь, заведующий лабораторией эллионии, Институт прикладных физических проблем им. А. Н. Севченко Белорусского государственного университета, Минск, Беларусь
- Мангин Стефан**, Ph.D., профессор кафедры физики материи и материалов Института Жана Ламура, Университет Лотарингии, Нанси, Франция
- Першин Владимир Федорович**, д.т.н., профессор, профессор кафедры «Техника и технологии производства нанопроductов», ТГТУ, Тамбов, Россия
- Ставрев Димитр**, д.т.н., профессор, профессор кафедры «Материаловедения», Варненский технический университет, Варна, Болгария
- Столин Александр Моисеевич**, д.ф.-м.н., профессор, заведующий лабораторией, ИСМАН РАН, Черноголовка, Московская область, Россия
- Танимото Есифуми**, Ph.D., профессор, Хиросимский университет, Япония
- Валитов Венер Анварович**, д.т.н., ведущий научный сотрудник, Институт проблем сверхпластичности металлов РАН, Уфа, Республика Башкортостан, Россия
- Аракелян Сергей Мартиросович**, д.ф.-м.н., профессор, заведующий кафедрой физики и прикладной математики, Владимирский государственный университет им. А. Г. и Н. Г. Столетовых, Владимир, Россия
- Бабаяев Ариф Азимович**, д.ф.-м.н., профессор, заведующий лабораторией оптических явлений в конденсированных средах Института физики им. Х. И. Амирханова ДНЦ РАН, Махачкала, Республика Дагестан, Россия
- Теруков Евгений Иванович**, д.т.н., профессор, заместитель генерального директора по научной работе ООО «НТЦ тонкопленочных технологий в энергетике при ФТИ им. А.Ф. Иоффе», Санкт-Петербург, Россия
- Долматов Валерий Юрьевич**, д.т.н., начальник научно-исследовательской лаборатории, «Специальное конструкторско-технологическое бюро «Технолог», Санкт-Петербург, Россия
- Савин Валерий Васильевич**, д.ф.-м.н., ведущий научный сотрудник, заведующий лабораторией физического материаловедения МНИЦ «Когерентная рентгеновская оптика для установок «Мегасайенс», Балтийский федеральный университет им. Иммануила Канта, Калининград, Россия
- Селютин Геннадий Егорович**, к.ф.-м.н., доцент, старший научный сотрудник, Институт химии и химической технологии Сибирского отделения Российской академии наук ФИЦ КНЦ СО РАН, Красноярск, Россия
- Петров Владимир Владимирович**, д.ф.-м.н., профессор, Саратовский национальный исследовательский университет им. Н. Г. Чернышевского, Саратов, Россия
- Калинин Юрий Егорович**, д.ф.-м.н., профессор, Воронежский государственный технический университет, Воронеж, Россия
- Севостьянов Владимир Семенович**, д.т.н., профессор, заведующий кафедрой «Технологические комплексы, машины и механизмы», Белгородский государственный технологический университет им. В. Г. Шухова, Белгород, Россия
- Мухин Виктор Михайлович**, д.т.н., профессор, Российский химико-технологический университет им. Д. И. Менделеева, Москва, Россия
- Вермель Владимир Дмитриевич**, д.т.н., профессор, начальник Научно-технического центра научно-производственного комплекса, Центральный аэрогидродинамический институт им. профессора Н. Е. Жуковского, Московская область, Жуковский, Россия
- Усолицева Надежда Васильевна**, д.х.н., профессор, директор НИИ наноматериалов, Ивановский государственный университет, Иваново, Россия
- Абдрахманова Ляйля Абдулловна**, д.т.н., профессор, Казанский государственный архитектурно-строительный университет, Казань, Россия
- Сергеев Вячеслав Андреевич**, д.т.н., профессор, директор Ульяновского филиала ФГБУН «Институт радиотехники и электроники им. В. А. Котельникова» РАН, Ульяновск, Россия
- Запороцкова Ирина Владимировна**, д.ф.-м.н., профессор, директор института приоритетных технологий, Волгоградский государственный университет, Волгоград, Россия
- Гутерман Владимир Ефимович**, д.х.н., профессор, главный научный сотрудник, Южный федеральный университет, Ростов-на-Дону, Россия
- Тафинцева Валерия Сергеевна**, Ph.D., научный сотрудник, кафедра физики, факультет науки и технологий, Норвежский университет естественных наук, Норвегия
- Тютюнник Вячеслав Михайлович**, д.т.н., профессор, генеральный директор ООО «Международный информационный Нобелевский центр» (МИНЦ), ТГТУ, Тамбов, Россия
- Переводчик:** Гунина Наталия Александровна, к.ф.н., заведующий кафедрой «Международная научная и профессиональная коммуникация», ТГТУ, Тамбов, Россия

CONTENTS

Original papers

Manufacturing processes and systems

- Gorokhovskiy A. V., Tsyganov A. R., Goffman V. G., Gorshkov N. V., Tretyachenko E. V., Makarov A. A., Batyrova A. R.** Synthesis and electrical properties of the ceramic materials based on $K_xMn_yR_zTi_{8-y-z}O_{16}$ (R = Al, Cr, Fe) hollandite-like solid solutions..... 160

Materials for energy and environment, next-generation photovoltaics, and green technologies

- Oskin P. V., Lepikash R. V., Dyachkova T. P., Alferov S. V.** Comparative evaluation of different methods for determining the specific surface area of carbon materials used in electrochemical systems 167

- Timirgaliev A. N., Burakova I. V., Rybakova S. O., Ananyeva O. A., Yarkin V. O., Kuznetsova T. S., Kadum A. H. K., Burakov A. E.** Removal of organic dyes from aqueous solutions using a graphene-containing sorbent based on activated rapeseed biochar: kinetics and isotherms 177

- Yaskevich A. L., Hliavitskaya T. A., Yushkin A. A., Pratsenko S. A., Nazarov E. A., Efimov M. N., Muratov D. G., Plisko T. V., Bilyukevich A. V.** Production of carbon membranes from porous polyacrylonitrile hollow fibers via IR pyrolysis 188

Reviews

Nanostructured, nanoscale materials and nanodevices

- Bukharov D. N., Tumarkina D. D., Kucherik A. O., Tkachev A. G., Arakelyan S. M., Burakova I. V., Burakov A. E.** Structure control of metal-carbon composites with different nanotopological configurations and electrical conductivity characteristics in a laser experiment 207

СОДЕРЖАНИЕ

Оригинальные статьи

Производственные процессы и системы

- Гороховский А. В., Цыганов А. Р., Гоффман В. Г., Горшков Н. В., Третьяченко Е. В., Макаров А. А., Батырова А. Р. Синтез и электрические свойства керамических материалов на основе голландитоподобных твердых растворов $K_xMn_yR_zTi_{8-y-z}O_{16}$ (R = Al, Cr, Fe) 160

Материалы для энергетики и окружающей среды,

фотоэлектрическая энергия следующего поколения и зеленые технологии

- Оськин П. В., Лепикаш Р. В., Дьячкова Т. П., Алферов С. В. Сравнительная оценка различных методов определения удельной площади поверхности углеродных материалов, использующихся в электрохимических системах 167
- Тимиргалиев А. Н., Буракова И. В., Рыбакова С. О., Ананьева О. А., Яркин В. О., Кузнецова Т. С., Кадум А. Х. К., Бураков А. Е. Удаление органических красителей из водных растворов с помощью графенсодержащего сорбента на основе активированного рапсового биоугля: кинетика и изотермы 177
- Яскевич А. Л., Глевицкая Т. А., Юшкин А. А., Праценко С. А., Назаров Е. А., Ефимов М. Н., Муратов Д. Г., Плиско Т. В., Бильдюкевич А. В. Получение углеродных мембран из полиакрилонитрильных полых волокон методом ИК-пиролиза 188

Обзор

Наноструктурированные, наномасштабные материалы и наноустройства

- Бухаров Д. Н., Тумаркина Д. Д., Кучерик А. О., Ткачев А. Г., Аракелян С. М., Буракова И. В., Бураков А. Е. Управление структурой металлоуглеродных композитов разной нанотопологической конфигурации и характеристики электропроводимости в лазерном эксперименте..... 207

Synthesis and electrical properties of the ceramic materials based on $K_xMn_yR_zTi_{8-y-z}O_{16}$ ($R = Al, Cr, Fe$) hollandite-like solid solutions

© Alexander V. Gorokhovskiy^a✉, Alexey R. Tsyganov^a, Vladimir G. Goffman^a, Nikolay V. Gorshkov^a, Elena V. Tretyachenko^a, Aleksey A. Makarov^a, Aina R. Batyrova^a

^a Yuri Gagarin State Technical University of Saratov, 77, Polytekhnicheskaya, Saratov, 410054, Russian Federation

✉ algo54@mail.ru

Abstract: The potassium polytitanates (PPT) modified in the aqueous solutions containing the mixtures of water soluble salts of Mn^{2+} and trivalent metals ($R^{3+} = Fe^{3+}, Cr^{3+}$ or Al^{3+}) are used as intermediates to produce ceramic sinters consisting of hollandite-like solid solutions corresponding to the chemical composition of $K_{1.3\pm 0.1}Mn_{1.5\pm 0.1}R_{0.2}Ti_{6.3\pm 0.1}O_{16}$. It has been shown that an introduction of various trivalent metals into the salt compositions used to obtain Mn-containing powdered potassium polytitanate (PPT-Mn/ R^{3+}) makes it possible to produce single-phase ceramics based on the resulting products by sintering. The resulting ceramic materials are characterized with a colossal dielectric constant at low frequencies and *ac*-conductivity varied in a wide range of values depending R^{3+} . The mechanism of relaxation processes occurring in the resulting ceramic materials and the prospects for their application are considered. The ceramics based on PPT-Mn/Cr intermediates are characterized by relatively high *ac*-conductivity ($10^{-7.5}$ Sm·cm⁻¹) and permittivity (10^8 at 10^{-2} Hz), and can be used in manufacturing of BLC electrode materials, whereas, the ceramics produced with the PPT-Mn/Fe intermediate and characterized by relatively low *ac*-conductivity ($10^{-9.2}$ Sm/cm) and high permittivity ($10^{7.3}$ at 10^{-2} Hz) can be used as a dielectric material in manufacturing of ceramic capacitors.

Keywords: intermediates; crystallization; hollandite-like solid solutions; functional ceramics; electrical properties.

For citation: Gorokhovskiy AV, Tsyganov AR, Goffman VG, Gorshkov NV, Tretyachenko EV, Makarov AA, Batyrova AR. Synthesis and electrical properties of the ceramic materials based on $K_xMn_yR_zTi_{8-y-z}O_{16}$ ($R = Al, Cr, Fe$) hollandite-like solid solutions. *Journal of Advanced Materials and Technologies*. 2024;9(3):160-166. DOI: 10.17277/jamt.2024.03.pp.160-166

Синтез и электрические свойства керамических материалов на основе голландитоподобных твердых растворов $K_xMn_yR_zTi_{8-y-z}O_{16}$ ($R = Al, Cr, Fe$)

© А. В. Гороховский^a✉, А. Р. Цыганов^a, В. Г. Гоффман^a, Н. В. Горшков^a, Е. В. Третьяченко^a, А. А. Макаров^a, А. Р. Батырова^a

^a Саратовский государственный технический университет имени Гагарина Ю. А., ул. Политехническая, 77, Саратов, 410054, Российская Федерация

✉ algo54@mail.ru

Аннотация: Полититанаты калия (ППТ), модифицированные в водных растворах, содержащих смеси водорастворимых солей Mn^{2+} и трехвалентных металлов ($R^{3+} = Fe^{3+}, Cr^{3+}$ или Al^{3+}), используются в качестве полупродуктов для получения керамических агломератов, состоящих из голландитоподобных твердых растворов, соответствующих химическому составу $K_{1.3\pm 0.1}Mn_{1.5\pm 0.1}R_{0.2}Ti_{6.3\pm 0.1}O_{16}$. Показано, что введение различных трехвалентных металлов в солевые композиции, используемые для получения Mn-содержащего порошкообразного полититаната калия (ППТ-Mn/ R^{3+}), позволяет получать однофазную керамику на основе полученных продуктов методом спекания. Полученные керамические материалы характеризуются колоссальной диэлектрической проницаемостью на низких частотах и проводимостью на переменном токе, варьирующей в широком диапазоне значений в зависимости от типа R^{3+} . Рассмотрен механизм релаксационных процессов, происходящих в полученных керамических материалах, и перспективы их применения. Керамика на основе

полупродуктов ППТ-Mn/Cr характеризуется относительно высокими значениями электропроводности ($10^{-7.5}$ См/см) и диэлектрической проницаемости (10^8 при 10^{-2} Гц) и может быть использована в производстве ВЛС-электродных материалов, тогда как керамика, полученная с использованием интермедиата ППТ-Mn/Fe и характеризующаяся относительно низкой электропроводностью ($10^{-9.2}$ См/см) и высокой диэлектрической проницаемостью ($10^{7.3}$ при 10^{-2} Гц) может быть использована в качестве диэлектрического материала при производстве керамических конденсаторов.

Ключевые слова: интермедиаты; кристаллизация; голландитоподобные твердые растворы; функциональная керамика; электрические свойства.

Для цитирования: Gorokhovskiy AV, Tsyganov AR, Goffman VG, Gorshkov NV, Tretyachenko EV, Makarov AA, Batyrova AR. Synthesis and electrical properties of the ceramic materials based on $K_xMn_yR_zTi_{8-y-z}O_{16}$ ($R = Al, Cr, Fe$) hollandite-like solid solutions. *Journal of Advanced Materials and Technologies*. 2024;9(3):160-166. DOI: 10.17277/jamt.2024.03.pp.160-166

1. Introduction

Modern electronics needs new functional materials characterized by regulated electric properties and various combinations of functionalities. Such materials can be used in manufacturing of electric capacitors, storage devices, thermistors, electric filters, etc. [1–3]. Among them, the materials exhibiting a colossal dielectric constant (CDC, $\epsilon > 10^3$) are of great interest for producing high-density charge storage devices (memory drives) including boundary layer capacitors (BLC) and multilayer ceramic capacitors (MLCC).

Ferroelectrics with perovskite-like structure ($BaTiO_3$, $PbTiO_3$, $PbZrO_3$, etc.) currently form the basis of most ceramics demonstrating CDC values, but only within a narrow temperature range close to T_c . The best known non-ferroelectric CDC materials ($CaCu_3Ti_4O_{12}$, $Ba(Fe_{0.5}Nb_{0.5})O_3$, and NiO based ceramics) possess excellent dielectric properties ($\epsilon \sim 10^5$) [4, 5]. Nevertheless, creating materials characterized by higher dielectric constant values, regulated frequency dependence of permittivity and lower temperature of sintering remains a significant problem.

In this regard, the hollandite-like solid solutions could open up new ways in the design and production of advanced non-ferroelectric ceramic materials. Some solid solutions, synthesized in the system of $K_2O-M_xO_y-TiO_2$ ($M = Ni, Cu, Co, Cr, Fe$) [6–8], have shown $\epsilon = 10^3-10^6$ ($f = 0.01$ Hz) at (23 ± 2) °C. The $K_xM_yTi_{8-y}O_{16}$ hollandite-like ceramics based on the amorphous potassium polytitanates (PPT) modified in aqueous solutions of some transition metal salts [6] feature submicro-sized crystals facilitating the production of layered ceramics. This experimental technique enables relatively simple and fast production of the hollandite-like materials compared to other traditional time-consuming experimental methods, such as multistage molten salt

and solid state synthesis [9], as well as a more complex sol-gel technique [8].

However, the hollandite-like solid solution based on modified potassium polytitanates, as well as those produced by other methods [6–9], are significantly contaminated with secondary crystalline phases (TiO_2 , $MeTiO_3$, Me_2O_3).

The goal of this research is to justify a method of producing mono-phase hollandite-like ceramics characterized by enhanced CDC values. This can be achieved by using the potassium polytitanate intermediates modified in the aqueous solutions containing the combinations of divalent (Mn^{2+}) and trivalent (R^{3+}) metals.

2. Materials and Methods

2.1. Materials and preparing methods

The parent potassium polytitanate powder (PPT) was synthesized at 500 °C by the molten salt method described in [10]. The PPT-based intermediates were produced by treating the parent PPT in the aqueous solutions containing the mixtures of sulfates of Mn^{2+} and trivalent metals (Al^{3+} , Cr^{3+} , Fe^{3+}). The $[Mn]/[R]$ molar ratio (n) in the mixed aqueous solutions was selected as $n = 2 : 1$ to align with the stoichiometry of layered double hydroxides (LDH) incrusting the PPT flakes by corresponding nanoscale LDH particles [11].

Given that such mixed salt solutions are characterized by complicated physicochemical processes accompanied with hydrolysis, sedimentation of certain products and complexation [12–14], depending on pH and nature of the used salts, the prepared solutions (0.01 M for each salt, $pH = 6.4 \pm 0.2$) were soaked for 6 hours to obtain chemically stable systems. Further, the solutions were filtered with the Whatman No 40 filters to separate the sediments (metal hydroxides), and used to modify PPT particles. Finally, the PPT powder was

introduced into the resulting aqueous solution (1 g per 100 mL) and stirred for 4 hours [6, 7].

The resulting precipitate was washed with distilled water until reaching a pH = 8.5 and dried at 50 °C for 4 hours. The final products were marked as PPT-Mn/R³⁺ (R = Al, Cr, Fe).

The powdered intermediates were compacted at 200 MPa to produce the discs of 12 mm in diameter and (2.0 ± 0.1) mm in thickness, and then sintered at 900 °C for 2 hours to produce the ceramic specimens.

2.2. Testing methods

The resulting ceramics were investigated using a scanning electron microscope (SEM) Aspex EXplorer (acceleration voltage of 15 kV) and X-ray ARL X'TRA diffractometer (CuK α source, λ = 0.15406 nm, 40 kV). The chemical composition was determined through the wavelength dispersive X-ray fluorescence analysis (Spectroscan MAX-GV).

To evaluate the electrical properties, the bases of the produced ceramic discs were coated with silver-palladium adhesive (K13 trade mark), and the obtained specimens were investigated using the impedance spectroscopy analyzer Novocontrol Alpha AN at (23 ± 2) °C. The mechanical strength of the discs was measured in accordance with ASTM C1424-15.

The porosity of the ceramic sinters was calculated using a ratio of the real and apparent densities, determined by the picnometric method (Russian Standard 24409-80).

3. Results and Discussion

The XRD patterns of the obtained ceramic materials are presented in Fig. 1. All the materials can be classified as K_xMn_yR_zTi_{8-y-z}O₁₆ solid solutions.

Their structure corresponds to the hollandite-like phases, specifically KMnTi₃O₈ (54-1183) or K_{1.46}Ti_{7.2}Fe_{0.8}O₁₆ (5-60) (JCPDS-ICDD-2009 base of data).

It can be inferred that during the thermal treatment the R³⁺ additives stabilize structure of the titanate polyanions, as represented in the PPT, and inhibit crystallization of perovskite-like MnTiO₃, which intensively forms in the PPT-Mn based intermediates [7].

The chemical composition of the obtained ceramics (Table 1) allows us to classify the obtained substances as K_{1.3}Mn_{1.5}Al_{0.2}Ti_{6.2}O₁₆, K_{1.4}Mn_{1.4}Cr_{0.2}Ti_{6.4}O₁₆ and K_{1.3}Mn_{1.6}Fe_{0.2}Ti_{6.2}O₁₆ hollandite-like solid solutions with similar structure and composition. This formula corresponds to the general stoichiometry K_xMe³⁺_yTi_{8-y}O₁₆ (x ≈ y), which is traditionally recognized in the literature for such substances and indicates the presence of manganese in the Mn³⁺ state, similar to the hollandite-like solid solutions based on PPT-Mn intermediates [7].

The secondary phases observed in the sinters correspond to MnTiO₃ (PPT-Mn/Al precursor) and spinel-like Mn_{1.5}Cr_{1.5}O₄ (Mn_{1.5}Al_{1.5}O₄); however, the total content of these phases in all the investigated systems is less than 3 %, allowing to consider them as traces.

The chemical compositions of all the intermediates (PPT-Mn/R), as well as the ceramic powders obtained by their thermal treatment, are very close and facilitate the formation of the same crystalline phase (a hollandite-like solid solution K_{1.3±0.1}Mn_{1.5±0.1}R_{0.2}Ti_{6.3±0.1}O₁₆) at high temperatures.

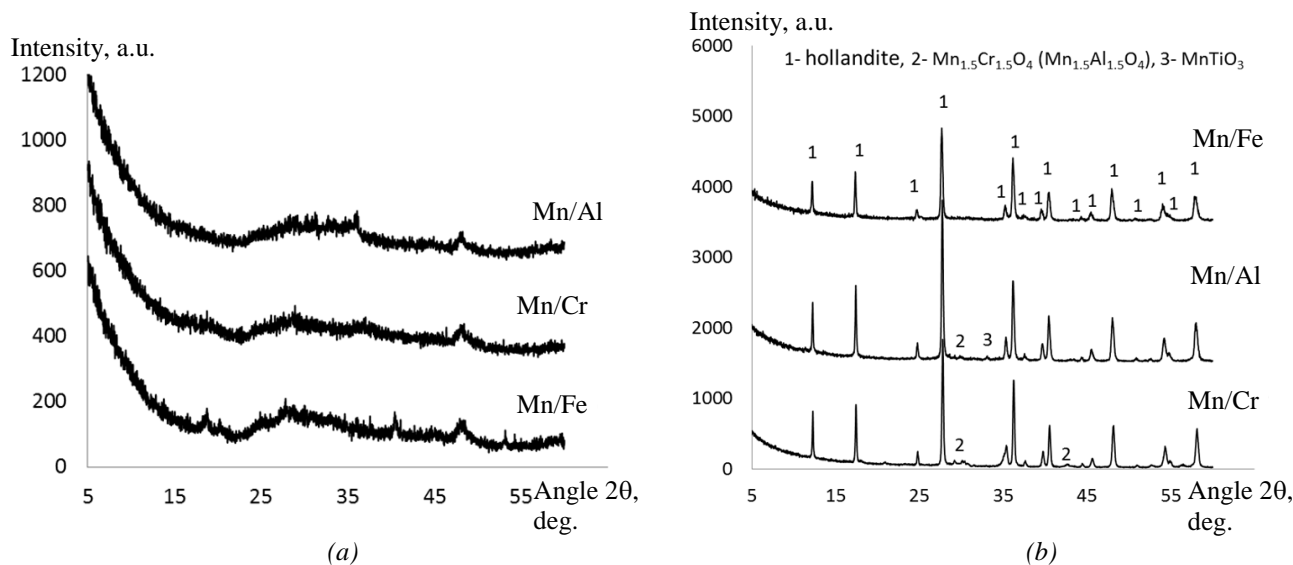


Fig. 1. XRD patterns of the PPT-Mn/R³⁺ precursors (a) and ceramic sinters based thereon (b)

Table 1. Chemical composition (X-ray fluorescence analysis data), compressive strength (CS), porosity (P), electric conductivity (σ_{dc}) and electric resistance of the equivalent circuit (R) of the obtained ceramic materials (Me = Fe, Cr or Al)

Precursor material	Content, at. % ($\pm 0,1$)					CS, MPa	P, %	σ_{dc}^* , $\times 10^8$ $\text{Sm}\cdot\text{cm}^{-1}$	R^* , $\text{M}\Omega$
	K	Mn	Me	Ti	O				
PPT-Mn/Al	5.2	6.1	0.8	24.6	63.3	145 ± 10	4 ± 1	0.90	0.67
PPT-Mn/Cr	5.0	6.0	0.8	25.1	63.0	123 ± 12	7 ± 2	0.42	1.40
PPT-Mn/Fe	5.1	6.3	0.8	24.5	63.2	111 ± 18	9 ± 2	0.91	1.11

* calculated from the impedance spectra.

To explain this phenomenon we have to take into account that in accordance with the X-ray fluorescence and XRD analysis data, the separated sediments obtained after soaking the mixed aqueous solutions consist of amorphous hydroxides of metals (Fe, Cr, Al) characterized by low critical values of pH ($\text{pH}_{\text{crys}} = 2.0$; 5.6 and 4.8, respectively [12–14]). These critical pH values are lower than $\text{pH} = 6.4$ obtained in the parent mixed aqueous solutions. Consequently, soaking these solutions leads to a removal of the main part of Fe, Cr and Al with sediments, whereas most of Mn ($\text{pH}_{\text{crys}} = 8$ [12]) remains in the solutions. We can also assume that the remaining Fe, Cr or Al in the parent solution forms any hydroxo-anion aqua-complexes with Mn containing ions (Mn^{2+} , and MnOH^+) found in the solution at $\text{pH} = 6.4$ [13–16]. Most likely, the nature of such complexation is similar for various R^{3+} containing ions [16]. As a result, the initial molar ratio of $[\text{Mn}]/[\text{R}] \approx 2$ was transformed to $[\text{Mn}]/[\text{R}] \approx 7$ in all investigated parent aqueous solutions, and this phenomenon was confirmed across 5 experimental series for each combination of salts. Therefore, the PPT-Mn/R products obtained by PPT treatment in the mixed aqueous solutions were considered as stable intermediates to produce ceramics based thereon.

The resulting ceramic bodies have a dense structure (Fig. 2a) significantly low porosity and high compressive strength (Table 1).

The impedance spectra of the ceramic sinters are presented in Fig. 2b. The impedance spectra observed in the low-frequency region represent the angle close to 45° with the Z' axis (high contribution of the diffusion process). At the same time, the shape of the Cole-Cole plots (semicircles) at high frequencies indicates that volume processes related to conductivity, taking place in these conditions, predominantly influence the impedance. The electrical resistance (R) and dc-conductivity of the

corresponding equivalent circuits can be determined from the $Z'' = f(Z')$ dependence (Fig. 2b) [17].

Using the measured Z' and Z'' values, the following characteristics were calculated: complex specific conductivity σ^* , ac – and dc conductivities, the real ε' and imaginary ε'' components of the dielectric constant

$$\varepsilon^* = \varepsilon'(\omega) - i\varepsilon''(\omega) = -i \frac{1}{\varepsilon_0 \omega s} \frac{l}{Z} Z^{*-1};$$

$$\sigma^* = \frac{l}{s} Z^{*-1},$$

where s is the electrode area and ω is the angular frequency.

The resistance corresponding to ionic conductivity was calculated by extrapolating the high-frequency region of the hodograph (Fig. 2.b) to the axis of real resistances (R). Conductivity σ (ionic component or volumetric conductivity) was calculated using the relation $\sigma = d/(R \cdot s)$, where d is the thickness of the ceramic sample (disk), R is the resistance found by extrapolation. The electronic component of conductivity (low-frequency conductivity measured at a frequency of 10^{-2} Hz) was determined from Fig. 2d as an extrapolation of the frequency dependences of conductivity on the $\log(\sigma_{ac})$ axis, i.e. determination of conductivity at a frequency of 10^{-2} Hz.

A simple shape of the semicircles in the Cole-Cole plots and relatively high values of the electric resistance determined by extrapolating the high-frequency arc to intersect the axis of real resistances indicate that the transport of electric charge carriers along boundaries of the crystals ($2e^- + 1/2\text{O}_2 = \text{O}^{2-}$) reveals principal contribution in the conductivity [18].

Thus, the intermediates based on the PPT-Mn/R system have allowed for the production of mono-phase ceramic dielectrics through sintering, whereas the PPT-Mn intermediates only facilitated the

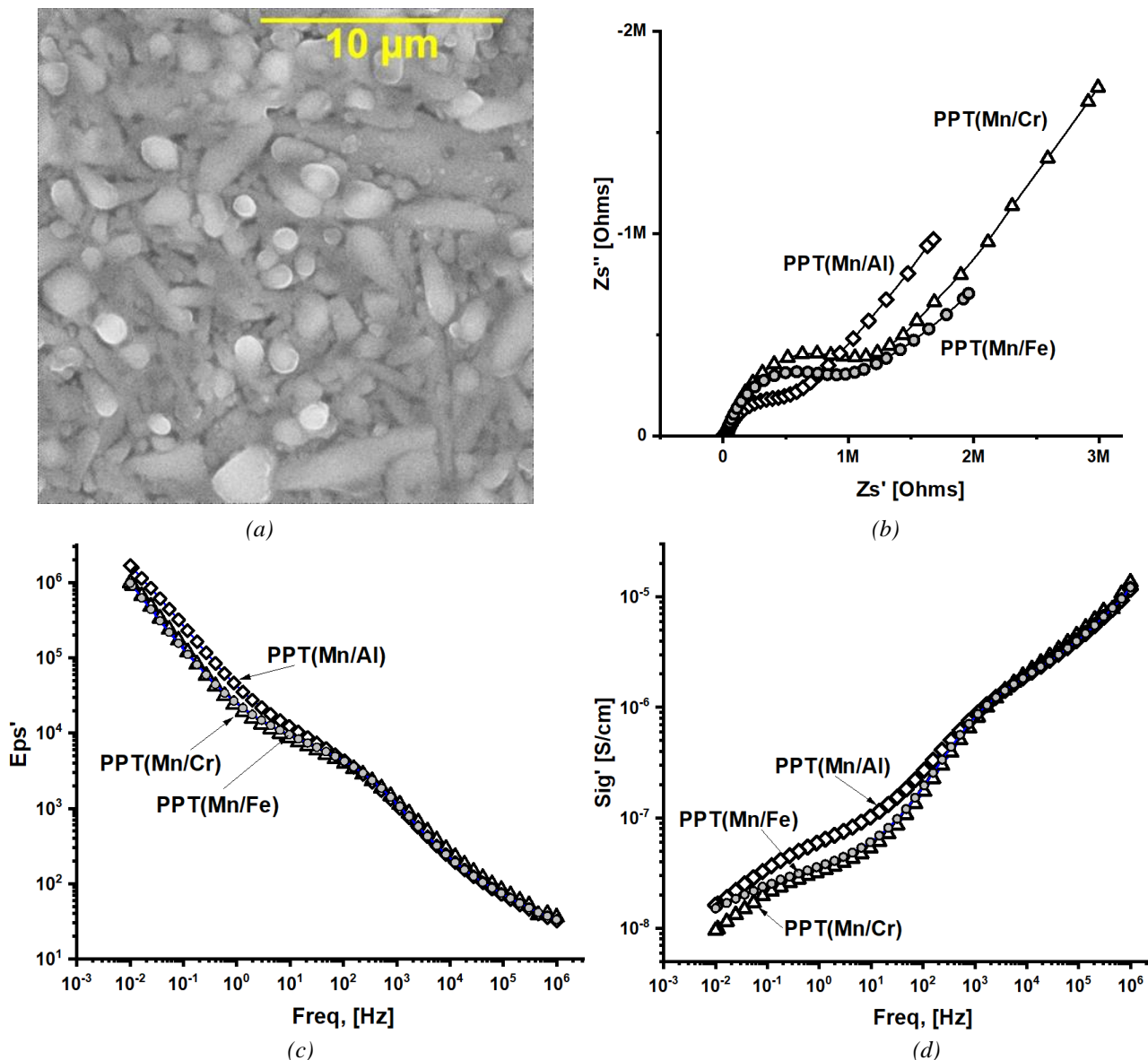


Fig. 2. Typical fracture surface of the ceramic sinter (PPT-Mn/Cr) (a), Cole-Cole plots of the impedance data (b) and frequency dependences of permittivity (c) and conductivity (d) for the sinters based on various PPT-Mn/R³⁺ intermediates

formation of ceramic composites, characterized by the presence of various secondary crystalline phases, lower permittivity and higher conductivity [7]. The permittivity of the obtained ceramics has extremely high values (Fig. 2c) and monotonically decreases with increased frequencies. The origin of high dielectric constant in the obtained non-ferroelectric systems at the room temperature can be attributed to both intrinsic and extrinsic relaxation processes (such as grain boundary, electrode interface) [19, 20]. The sources of conductivity and relaxation mechanisms in these materials can be discussed in terms of defect structures. A movement of the charged point defects (Ti³⁺, typical for the hollandite-like structures [9]), free charge carriers (e⁻, K⁺) and oxygen vacancies as well as accumulation of charge carriers at the grain

boundaries enhances the dielectric constant in these materials. Transition metals with various oxidation states (Mn, Fe, Cr) can also act as charged point defects and facilitate hopping conductivity. Nevertheless, it is interesting that the hollandite-like solid solutions of all the investigated compositions are characterized by very similar values of permittivity and conductivity in a wide range of frequencies in spite of different kinds of R³⁺ metal used as a dopant.

The findings indicate that the mono-phase PPT-Mn/Fe based ceramic materials are promising for the MLCC manufacturing due to their higher permittivity and lower conductivity compare to previously investigated hollandite-like materials based on simple PPT-Me intermediates [6–8].

4. Conclusion

1. The obtained results indicate that the potassium polytitanates modified in the stabilized aqueous solutions containing the mixtures of water soluble salts of Mn and trivalent metals (*R*), such as Fe, Cr or Al, can be used as intermediates to produce mono-phase ceramic sinters consisting of hollandite-like solid solutions (purity of 99+) corresponding to the formula of $K_{1.3\pm 0.1}Mn_{1.5\pm 0.1}R_{0.2}Ti_{6.3\pm 0.1}O_{16}$.

2. The sintered ceramics produced through this method have a colossal dielectric constant (10^6 – 10^8) at low frequencies and relatively low *ac*-conductivity varying in the range of $10^{-7.5}$ – $10^{-9.2}$ depending on the R^{3+} type.

3. The ceramic materials based on PPT-Mn/*R* intermediates can be used in manufacturing of hybrid (electrostatic-electrochemical) electrode materials and could be advantageous in manufacturing high-density charge storage devices, such as ceramic capacitors.

5. Funding

This work was financially supported by the Foundation for Assistance to Small Innovative Enterprises in Science and Technology (Project №23ГТC2PЭC14/48796, Program TechnoStart)

6. Conflict of interests

The authors declare no conflict of interest.

References

1. Spearing SM. Materials issues in microelectromechanical systems (MEMS). *Acta Materialia*. 2000;48(1):179-196. DOI:10.1016/S1359-6454(99)00294-3
2. Setter N, Waser R. Electroceramic materials. *Acta Materialia*. 2000;48(1):151-178. DOI:10.1016/S1359-6454(99)00293-1
3. Cava RJ. Dielectric materials for applications in microwave communications. *Journal of Materials Chemistry*. 2001;11(1):54-62. DOI:10.1039/b0036811
4. Ramirez AP, Subramanian MA, Gardel M, Blumberg G, et al. Giant dielectric constant response in a copper-titanate. *Solid State Communications*. 2000;115(5):217-220. DOI:10.1016/S0038-1098(00)00182-4
5. Jana PK, Sarkar S, Chaudhuri BK. Maxwell-Wagner polarization mechanism in potassium and titanium doped nickel oxide showing giant dielectric permittivity. *Journal of Physics D: Applied Physics*. 2007;40(2):556-560. DOI:10.1088/0022-3727/40/2/033
6. Gorokhovskiy AV, Tretyachenko EV, Goffman VG, Gorshkov NV, et al. Preparation and dielectric properties of ceramics based on mixed potassium titanates with the hollandite structure. *Inorganic Materials*. 2016;52(6):587-592. DOI:10.1134/S0020168516060042
7. Gorokhovskiy A, Saunina S, Maximova L, Tretyachenko E, et al. Synthesis and electric properties of the high-*k* ceramic composites based on potassium polytitanate modified by manganese. *Research on Chemical Intermediates*. 2022;48(3):1227-1248. DOI:10.1007/s11164-022-04669-x
8. Sinelshchikova OYu, Petrov SA, Besprozvannykh NV, Kuchaeva SK, et al. Features of sol-gel synthesis of new functional materials based on complex oxides with tunnel structure. *Journal of Sol-Gel Science and Technology*. 2013;68(3):495-499. DOI:10.1007/s10971-013-2988-7
9. Moetakef P, Larson AM, Hodges BC, Zavalij P, et al. Synthesis and crystal chemistry of microporous titanates $K(Ti,M)_8O_{16}$ where $M=Sc-Ni$. *Journal of Solid State Chemistry*. 2014;220:45-53. DOI:10.1016/j.jssc.2014.08.012
10. Sanchez-Monjaras T, Gorokhovskiy A, Escalante-Garcia JI. molten salt synthesis and characterization of potassium polytitanate ceramic precursors with varied TiO_2/K_2O molar ratios. *Journal of the American Ceramic Society*. 2008;91(9):3058-3065. DOI:10.1111/j.1551-2916.2008.02574.x
11. Gorokhovskiy AV, Tsiganov AR, Nikityuk TV, Escalante-Garcia JI, et al. Synthesis and properties of nanocomposites in the system of potassium polytitanate - layered double hydroxide. *Journal of Materials Research and Technology*. 2020;9(3):3924-3934. DOI:10.1016/j.jmrt.2020.02.018
12. Dean JG, Bosqui FL, Lanouette KH. Removing heavy metals from waste water. *Environmental Science & Technology*. 1972;6(6):518-522. DOI:10.1021/es60065a006
13. Reisfeld R, Jørgensen CK. *Chemistry, spectroscopy and applications of sol-gel glasses*. Vol. 77. Springer Berlin: Heidelberg; 1992. 265 p.
14. Zhao H, Liu H, Qu J. Effect of pH on the aluminum salts hydrolysis during coagulation process: Formation and decomposition of polymeric aluminum species. *Journal of Colloid and Interface Science*. 2009;330(1):105-112. DOI:10.1016/j.jcis.2008.10.020
15. Dolgonosov BM. Hydrolysis and coagulation of aluminum salts in the initial stage of mixing of solutions. *Theoretical Foundations of Chemical Engineering*. 2005;39(3):263-274. DOI:10.1007/s11236-005-0074-8
16. Doyle-Garner FM, Monhemius AJ. Hydrolytic stripping of single and mixed metal-versatic solutions. *Metallurgical Transactions B*. 1985;16(4):671-677. DOI:10.1007/BF02667504
17. Barsoukov E, Macdonald JR. *Impedance spectroscopy: theory, experiment, and applications*. 3rd edition. Hoboken, NJ: Wiley; 2018. 560 p.
18. Adler SB. Factors governing oxygen reduction in solid oxide fuel cell cathodes. *Chemical Reviews*. 2004;104(10):4791-4844. DOI:10.1021/cr020724o
19. Wu K, Huang Y, Li J, Li S. Space charge polarization modulated instability of low frequency

permittivity in $\text{CaCu}_3\text{Ti}_4\text{O}_{12}$ ceramics. *Applied Physics Letters*. 2017;111(4):042902. DOI:10.1063/1.4995968

20. Lunkenheimer P, Fichtl R, Ebbinghaus SG, Loidl A. Nonintrinsic origin of the colossal dielectric constants in $\text{CaCu}_3\text{Ti}_4\text{O}_{12}$. *Physical Review B*. 2004;70(17):172102. DOI:10.1103/PhysRevB.70.172102

21. Sleptsov VV, Ushkar MN, Zinin YV, Shchur PA, et al. Study of the specific energy of universal electrode materials for hybrid ultra-high-volume capacitor systems. *IOP Conference Series: Materials Science and Engineering*. 2020;868(1):012013. DOI:10.1088/1757-899X/868/1/012013

Information about the authors / Информация об авторах

Alexander V. Gorokhovskiy, D. Sc. (Chem.), Professor, Head of the Department, Yuri Gagarin State Technical University of Saratov (SSTU), Saratov, Russian Federation; ORCID 0000-0002-4210-3169; e-mail: algo54@mail.ru

Alexey R. Tsyganov, Cand. Sc. (Chem.), Research Associate, SSTU, Saratov, Russian Federation; ORCID 0000-0002-5112-7939; e-mail: tsyganov.a.93@mail.ru

Vladimir G. Goffman, D. Sc. (Chem.), Professor, SSTU, Saratov, Russian Federation; ORCID 0000-0002-2119-7688; e-mail: vggoff@mail.ru

Nikolay V. Gorshkov, Cand. Sc. (Eng.), Associate Professor, SSTU, Saratov, Russian Federation; ORCID 0000-0003-3248-3257; e-mail: gorshkov.sstu@gmail.com

Elena V. Tretyachenko, Cand. Sc. (Chem.), Associate Professor, SSTU, Saratov, Russian Federation; ORCID 0000-0001-9095-0920; e-mail: trev07@rambler.ru

Aleksey A. Makarov, Postgraduate, SSTU, Saratov, Russian Federation; ORCID 0009-0006-6650-1440; e-mail: aleksey.makw@gmail.com

Aina R. Batyrova, Postgraduate, SSTU, Saratov, Russian Federation; ORCID 0009-0002-6979-2539; e-mail: batyrova.aina@bk.ru

Гороховский Александр Владиленович, доктор химических наук, профессор, заведующий кафедрой, ФГБОУ ВО «Саратовский государственный технический университет имени Гагарина Ю. А.» (СГТУ имени Гагарина Ю.А.), Саратов, Российская Федерация; ORCID 0000-0002-4210-3169; e-mail: algo54@mail.ru

Цыганов Алексей Русланович, кандидат химических наук, научный сотрудник, СГТУ имени Гагарина Ю.А., Саратов, Российская Федерация; ORCID 0000-0002-5112-7939; e-mail: tsyganov.a.93@mail.ru

Гоффман Владимир Георгиевич, доктор химических наук, профессор, СГТУ имени Гагарина Ю.А., Саратов, Российская Федерация; ORCID 0000-0002-2119-7688; e-mail: vggoff@mail.ru

Горшков Николай Вячеславович, кандидат технических наук, доцент, СГТУ имени Гагарина Ю.А., Саратов, Российская Федерация; ORCID 0000-0003-3248-3257; e-mail: gorshkov.sstu@gmail.com

Третьяченко Елена Васильевна, кандидат химических наук, доцент, СГТУ имени Гагарина Ю.А., Саратов, Российская Федерация; ORCID 0000-0001-9095-0920; e-mail: trev07@rambler.ru

Макаров Алексей Алексеевич, аспирант, СГТУ имени Гагарина Ю.А., Саратов, Российская Федерация; ORCID 0009-0006-6650-1440; e-mail: aleksey.makw@gmail.com

Батырова Айна Рахатовна, аспирант, СГТУ имени Гагарина Ю.А., Саратов, Российская Федерация; ORCID 0009-0002-6979-2539; e-mail: batyrova.aina@bk.ru

Received 12 May 2024; Accepted 15 July 2024; Published 22 October 2024



Copyright: © Gorokhovskiy AV, Tsyganov AR, Goffman VG, Gorshkov NV, Tretyachenko EV, Makarov AA, Batyrova AR., 2024. This article is an open access article distributed under the terms and conditions of the Creative Commons Attribution (CC BY) license (<https://creativecommons.org/licenses/by/4.0/>).

Comparative evaluation of different methods for determining the specific surface area of carbon materials used in electrochemical systems

© Pavel V. Oskin^a✉, Roman V. Lepikash^a, Tatyana P. Dyachkova^b, Sergey V. Alferov^a

^a Tula State University, 92, Lenin Av., Tula, 300012, Russian Federation,

^b Tambov State Technical University, Bld. 2, 106/5, Sovetskaya St., Tambov, 392000, Russian Federation

✉ pavelfraj@yandex.ru

Abstract: In this paper, a comparative analysis of methods for determining the surface area in relation to electrode materials was carried out on the example of commercial carbon felts of various structures. For a more complete analysis, scanning electron microscopy and Raman spectroscopy methods were additionally used. It is shown that electrochemical methods for determining the surface area are selective with respect to the edge plane of graphite, which can be both an advantage and a disadvantage, depending on the objectives of the study. It is revealed that the use of the classical method of low-temperature adsorption of gases is not always justified due to the complexity of selecting the correct model describing the system under study. Adsorption of dyes from aqueous solutions seems to be the most suitable method for determining the wetted surface of the material, however, it requires large amounts of sample and is characterized by a significant error.

Keywords: carbon fiber; surface area; electron transfer rate; capacity of the double electric layer; basal plane of graphite; edge plane of graphite; adsorption of methylene blue.

For citation: Oskin PV, Lepikash RV, Dyachkova TP, Alferov SV. Comparative evaluation of different methods for determining the specific surface area of carbon materials used in electrochemical systems. *Journal of Advanced Materials and Technologies*. 2024;9(3):167-176. DOI: 10.17277/jamt.2024.03.pp.167-176

Сравнительная оценка различных методов определения удельной площади поверхности углеродных материалов, использующихся в электрохимических системах

© П. В. Оськин^a✉, Р. В. Лепикаш^a, Т. П. Дьячкова^b, С. В. Алферов^a

^a Тульский государственный университет,
пр. Ленина, 92, Тула, 300012, Российская Федерация,

^b Тамбовский государственный технический университет,
ул. Советская, 106/5, пом. 2, Тамбов, 392000, Российская Федерация

✉ pavelfraj@yandex.ru

Аннотация: В данной работе проведено сравнение методов определения площади поверхности применительно к электродным материалам на примере коммерческих углеродных войлоков различной структуры. Для более полного анализа дополнительно привлечена сканирующая электронная микроскопия, позволившая охарактеризовать морфологию поверхности материала и спектроскопия комбинационного рассеяния, с помощью которой оценивали количество дефектов в кристаллической структуре углерода, а также содержание аморфной фазы. Показана селективность электрохимических методов определения площади поверхности по отношению к краевой плоскости графита, что может являться как преимуществом, так и недостатком, в зависимости от целей исследования. Выявлено, что применение классического метода низкотемпературной адсорбции газов далеко не всегда оправдано, ввиду сложности подбора корректной модели, описывающей исследуемую систему. Кроме того, при исследовании приведенным методом электродных материалов полученные данные будут сильно

завышены из-за лучшей смачиваемости углеродного материала азотом, чем водой. Адсорбция красителей из водных растворов, по-видимому, является наиболее подходящим методом для определения смоченной поверхности материала, однако требует наличия большого числа образцов, характеризуется значительной погрешностью и может давать несколько завышенные результаты, хоть и меньшие, чем низкотемпературная адсорбция азота.

Ключевые слова: углеродное волокно; площадь поверхности; скорость переноса электронов; емкость двойного электрического слоя; базальная плоскость графита; краевая плоскость графита; адсорбция метиленового голубого.

Для цитирования: Oskin PV, Lepikash RV, Dyachkova TP, Alferov SV. Comparative evaluation of different methods for determining the specific surface area of carbon materials used in electrochemical systems. *Journal of Advanced Materials and Technologies*. 2024;9(3):167-176. DOI: 10.17277/jamt.2024.03.pp.167-176

1. Introduction

Specific surface area is one of the key parameters of carbon materials. Various methods are used to determine it. For example, for quasi-one-dimensional materials, it is possible to estimate the specific surface area based on the average fiber radius values [1–3]. However, the geometric estimate cannot be considered accurate, since it does not take into account the heterogeneity of the fiber surface. Low-temperature gas adsorption data [2, 4, 5] and dye adsorption from aqueous solutions [6, 7] are often used. In addition, a number of sources report on electrochemical methods for estimating the specific surface area [8, 9].

The results obtained by the Brunauer–Emmett–Teller (BET) method are often poorly suited for describing the electrochemical behavior of a carbon material due to the difference in the mechanisms of interaction between gas and electrolyte with carbon. Data on dye adsorption from solutions are more suitable in this sense, but difficulties with selecting a physical model of the process remain.

Electrochemical methods are free from this drawback, but require the use of accurate values of a number of constants. Moreover, if the diffusion coefficient used in calculations according to the

Randles-Shevchik equation [8] is known for most standard redox systems, then determining the specific capacity of the electric double layer (EDL) causes difficulties, since this value is made up of the capacities of the marginal and basal planes [10–12], data on which vary significantly in different sources (Table 1). For example, experimentally determined values of the capacity of the marginal plane differ by orders of magnitude due to the contribution of pseudocapacitance [13, 14].

Thus, all currently available methods for assessing the surface area of carbon materials have shortcomings. At the same time, the use of several complementary methods can provide reliable useful information, for example, the ratio of the areas of the basal and edge planes of graphite. This parameter is extremely important for characterizing the electrochemical properties of carbon materials. Thus, in [18], it was shown that materials with a high proportion of the edge plane are able to more effectively reduce oxygen in the cathode space of fuel cells. The rate of electron transfer in redox systems, for example, $[\text{Fe}(\text{CN})_6]^{3-}/[\text{Fe}(\text{CN})_6]^{4-}$ containing ascorbic acid or hydrazine significantly, depend on this ratio [19–21].

Table 1. Specific capacity of the basal and edge plane of graphite

Electrolyte	Basal plane capacity, $\mu\text{F}\cdot\text{cm}^{-2}$	Edge plane capacity, $\mu\text{F}\cdot\text{cm}^{-2}$	Reference
0,9 H NaF	3	50–70	[15]
1 mM HCF in 1M KCl	1–2	70	[11]
1M KCl	0.81	–	[16]
6 M LiCl	4.72 ± 0.37	430.1 ± 9.9	[13]
0,1 M Na_2HPO_4 (pH = 7), 0,1M KCl	4	10^5	[14]
6 M LiCl	4.3–6.0	–	[10]
6 M LiCl	1.7 ± 0.2	25 ± 6	[17]

Usually, the proportion of the edge plane is calculated from the value of the rate constant of heterogeneous electron transfer in the $[\text{Fe}(\text{CN})_6]^{3-}/[\text{Fe}(\text{CN})_6]^{4-}$ system according to equation (1) [11, 12].

$$k = k_e f_e + k_b (1 - f_e), \quad (1)$$

where k is the rate constant of heterogeneous electron transfer, $\text{cm}\cdot\text{s}^{-1}$; k_e is the rate constant of heterogeneous electron transfer to the edge plane of graphite, $\text{cm}\cdot\text{s}^{-1}$; k_b is the rate constant of heterogeneous electron transfer to the basal plane, $\text{cm}\cdot\text{s}^{-1}$; f_e is the fraction of the edge plane of graphite. This method is not very accurate due to the large error in determining the rate constant [22].

According to [1, 16], the fraction of the edge plane is also included in equation (2):

$$C = f_e C_e + (1 - f_e) C_b, \quad (2)$$

where C is the specific capacitance of the EDL for the material, $\mu\text{F}\cdot\text{cm}^{-2}$; C_e is the specific capacitance of the edge plane of graphite, $\mu\text{F}\cdot\text{cm}^{-2}$; C_b is the specific capacitance of the basal plane of graphite, $\mu\text{F}\cdot\text{cm}^{-2}$.

However, it is not possible to use equation (2) in practice due to the complexity of determining the exact value of the specific capacitance of the edge plane EDL.

The aim of this work was to compare different methods for determining the surface area for characterizing carbon materials that can be used in electrochemical systems in the future. Carbon felt was chosen as a model material, since it is widely used in the creation of supercapacitors [23, 24], electrochemical [5, 25] and bioelectrochemical [4, 26] current sources, as well as electrochemical sensors [8].

2. Materials and Methods

2.1. Initial materials and reagents

In this work, two commercial samples of carbon felt obtained by pyrolysis of polyacrylonitrile fiber in an inert atmosphere were investigated. Sample No. 1 was produced by Heibei Huasheng Felt Co Ltd. (China), sample No. 2 was produced by Kompozit-Polymer (Russia).

The reagents (methylene blue, potassium hexacyanoferrate (III), potassium chloride) used in the work were of analytical grade. All solutions were prepared with deionized water and stored in dark glassware at a temperature of 4 °C for no more than a week.

2.2. Analytical methods

Electron images were obtained on a JSM-6510 LV microscope (JEOL, Japan) in low vacuum mode (30 Pa) with secondary electron (SE) registration. Raman spectra were recorded on a DXR Raman Microscope (Thermo Scientific, USA) using a laser with a wavelength of 532 nm.

The surface area was determined by the adsorption of methylene blue (solution concentration $1 \text{ mmol}\cdot\text{dm}^{-3}$) according to the procedure [6] using an SF-2000 spectrophotometer (OKB-Spectr, Russia). The optical density of the dye was measured at a wavelength of 616 nm. The surface area was determined by nitrogen adsorption using a Quantochrome Autosorb IQ Nova 1200e specific surface area and porosity analyzer (Quantochrome Instruments, USA) at a temperature of 77 K and a partial pressure of 0.05–0.30. Electrochemical measurements were performed on a CORRTEST CS1350 potentiostat-galvanostat (Corrtest, China) in a three-electrode cell with a saturated silver chloride electrode as the reference electrode and a $0.5 \times 0.5 \times 0.1$ cm platinum foil as the auxiliary electrode. A 0.1 M KCl solution was used as the background electrolyte. The concentration of potassium hexacyanoferrate (III) in the solution was 0.5 mM. Cyclic voltammograms were recorded at scan rates of $10\text{--}500 \text{ mV}\cdot\text{s}^{-1}$ in the range of $-0.4\text{--}+0.6$ V.

Impedance spectra were recorded in 0.1 M KCl in the frequency range from 1 Hz to 0.1 MHz at the anodic potentials of cyclic voltammograms (CV) of potassium hexacyanoferrate (III) (to determine the rate constant of heterogeneous transfer) and at the open circuit potential (to determine the specific capacitance of the EDL). The voltage amplitude was 10 mV.

From the CV data, the rate constant of heterogeneous electron transfer was calculated using the Nicholson-Lavagnini method [27, 28] based on the slope of the dependence of the limiting current on $1/\psi$ in accordance with equation (3) obtained by combining the Nicholson and Randles-Shevchik equations:

$$I_p = 0.4463 n F S C \sqrt{1 - \alpha} \frac{k_s \sqrt{\pi}}{\psi}, \quad (3)$$

where I_p is limiting anode current; π is a mathematical constant, 3,14; $1 - \alpha$ is an electron transfer coefficient for the anode process; k_s is a rate constant of heterogeneous electron transfer; F is the Faraday number; S is the electrode area; n is the number of electrons participating in the reaction.

The parameter ψ was determined using equation (4) [28]:

$$\psi = -\frac{-0.6288 + 0.002\Delta E}{1 - 0.017\Delta E}, \quad (4)$$

where ψ is the Nicholson coefficient, V; ΔE is the difference between the potentials of the anodic and cathodic peaks, V.

From the electrochemical impedance spectroscopy data, the rate constant of heterogeneous electron transfer was calculated using equation (5) [27]:

$$k_s = \frac{RT}{R_F n^2 F^2 SX}, \quad (5)$$

where R is the universal gas constant, J·mol·K⁻¹; T is the temperature, K; R_F is the Faraday resistance of the reaction, Ohm; X is the concentration of the electro-active substance in the solution, mol·dm⁻³. To find the Faraday resistance, the Voigt ladder diagram was used. To calculate the specific capacity of the EDL, the Randles diagram was used [29].

Based on the results of the CV with a linear potential sweep at a potential sweep rate of 100 mV·s⁻¹ in the range of 0–0.5 V, the specific capacitance of the EDL of carbon felt was determined using equation (6) [30]:

$$C = \frac{\int_{E_1}^{E_2} I dE}{m(E_2 - E_1)}, \quad (6)$$

where I is the equation for the dependence of current on potential, A; E_1 is the initial potential of the cyclic voltammogram, V; E_2 is the final potential of the voltammogram, V; m is the mass of felt, g.

Charge-discharge curves were recorded at a charge-discharge current of 10 μ A in the potential range of 0–0.5 V. The specific capacity of the EDL was calculated using formula (7) [30]:

$$C = \frac{I'\Delta t}{m\Delta E'}, \quad (7)$$

where I' is the charging (discharging) current, A; Δt is the charging (discharging) time, s; $\Delta E'$ is the absolute value of the difference between the potential at the beginning and end of charging (discharging), V.

3. Results and Discussion

Scanning electron images (SEM) were obtained to characterize the morphology of the felt samples (Fig. 1). Both samples consist of interwoven carbon

fibers with a diameter of about 20 μ m. On the surface of these fibers, longitudinal grooves with a width of 0.1–0.3 μ m are observed, which apparently formed during the production of polyacrylonitrile fiber. On the surface of sample No. 2, growths with a size of 0.5–5.0 μ m are observed. The obtained results are consistent with the literature data [1].

The Raman spectra (Fig. 2) of both samples contain the G (1550 cm⁻¹) and D (1350 cm⁻¹) bands, which are characteristic of all carbon materials. The G band is due to vibrations of sp²-hybridized carbon atoms in the crystal structure of graphite, and the D band is due to the presence of defects in this structure. The degree of defectiveness of a carbon material is usually estimated by the intensity ratio of these bands (I_D/I_G) [31]. The Raman spectrum of sample No. 1 (Fig. 2a) is characterized by a high noise level, which may be a consequence of the amorphization of the structure [31]. This is confirmed by the presence of the D'' peak (1400 cm⁻¹) between the D and G bands, the intensity of which depends on the amount of the bulk amorphous phase in the structure [32]. The Raman spectrum of sample No. 2 (Fig. 2b) additionally contains the $2D$ (2700 cm⁻¹) and $D + G$ (2950 cm⁻¹) bands, characteristic of the ordered structure of graphite [33]. Thus, sample No. 1 is amorphized to a greater extent than sample No. 2. To confirm this conclusion, peaks D' (1600 cm⁻¹) and D'' , were additionally identified using mathematical processing of the Raman spectra in accordance with [34]. The defect density (n_D) [35], the distance between defects (L_a) [35] and the crystallite size (L_D) [36] were also calculated (Table 2).

The I_D/I_G ratio for both materials, the distance between defects, the density of defects and the sizes of crystallites differ slightly, which indicates the similarity of the general parameters of the structure disorder [31]. At the same time, judging by the value of $I_D/I_{D'}$ and the intensity of the D' band, surface [37, 38] rather than intracrystalline [31] defects of the graphite structure are more characteristic of sample No. 2. It is not entirely correct to compare the obtained absolute numerical values of the parameters given in Table 2 with the literature data due to the individual settings of each specific Raman spectrometer [39].

The specific surface area values were measured in various ways for the carbon felt samples, which were then compared with the literature data for analogs (Table 3).

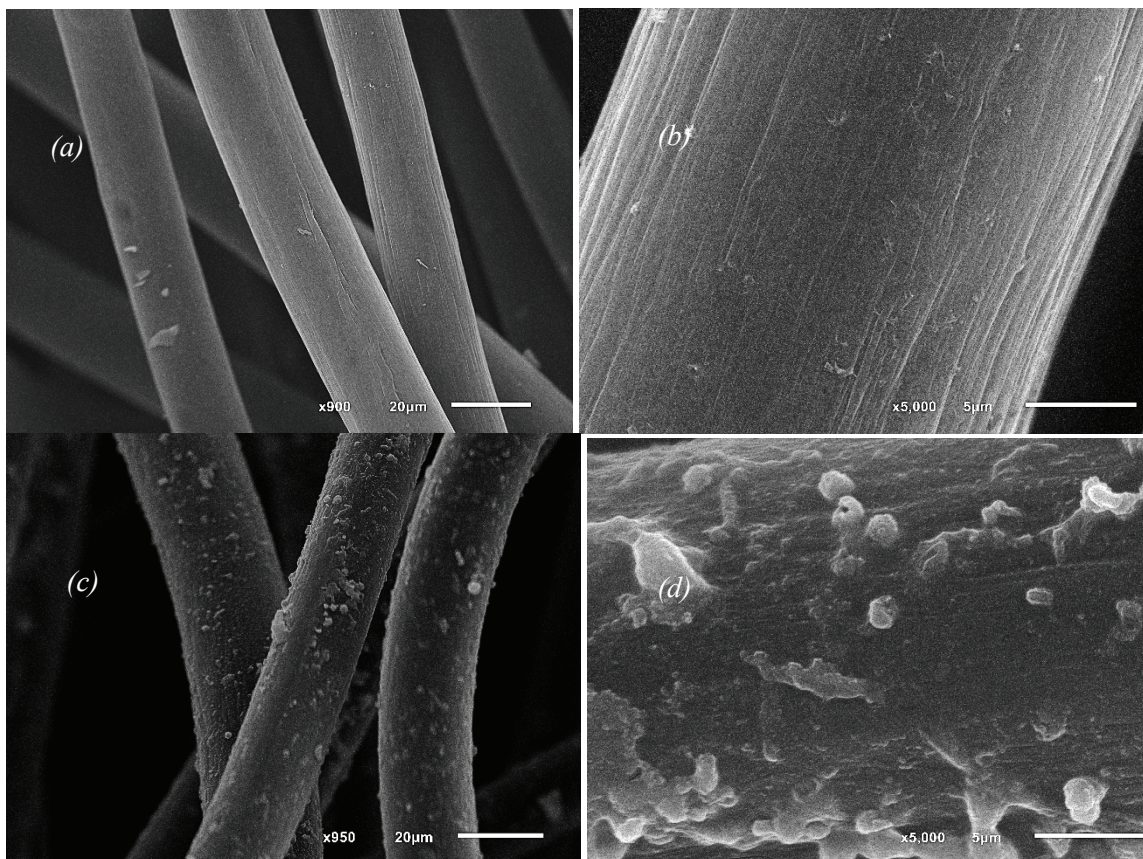


Fig. 1. SEM images of carbon felt samples No. 1 (a, b) and No. 2 (c, d)

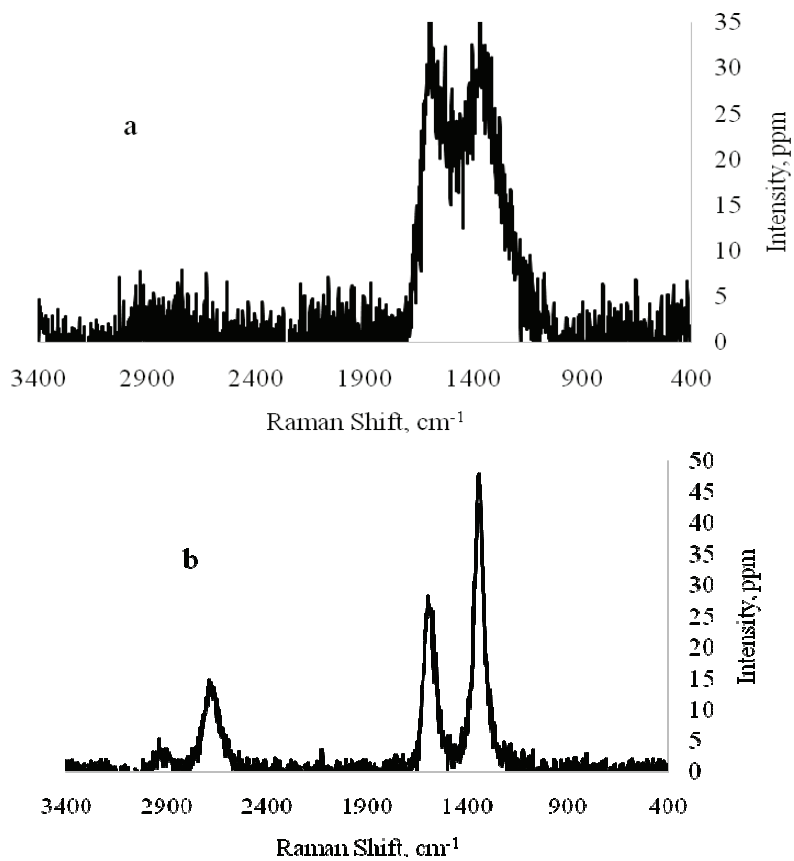


Fig. 2. Raman spectra of sample No. 1 (a) and sample No. 2 (b)

Table 2. Results of processing the Raman spectra of carbon and graphite felts

Sample	I_D/I_G	L_D , nm	$n_D \cdot 10^{-10}$, cm^{-2}	L_a , nm	I_D'/I_G	$I_{D''}/I_G$	$I_D/I_{D'}$	Type of defects
1	1.6 ± 0.1	33 ± 2	2.7 ± 0.2	10 ± 2	1.8 ± 0.4	0.7 ± 0.1	1.0 ± 0.2	Local
2	1.8 ± 0.2	32 ± 4	3.1 ± 0.3	9 ± 2	0.3 ± 0.1	–	6.1 ± 0.2	Regional, vacancies

Table 3. Specific surface area of carbon felt determined by various methods

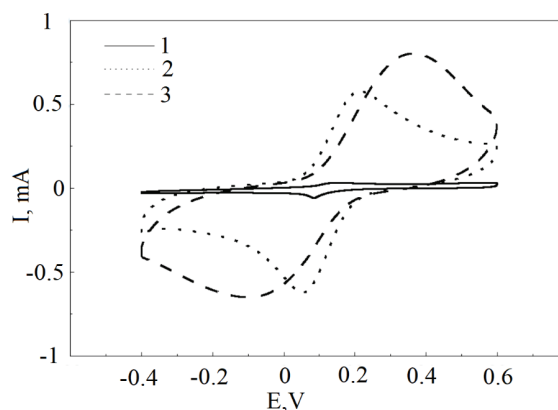
Method	Specific surface area, $\text{m}^2 \cdot \text{g}^{-1}$		References
	Sample No.1	Sample No. 2	
Nitrogen adsorption (BET)	–	–	0.4 [2]; 1.69 [4]; 0.5 [5]; 0.8 [25]; 1 [24]
Geometrical evaluation	0.011	0.011	0.028 [1]; 0.022 [3]
Methylene blue adsorption	4.5 ± 0.7	4.3 ± 0.4	–
Rendles-Szewczyk equation	0.072 ± 0.006	0.19 ± 0.02	–

It was not possible to determine the surface area by low-temperature gas adsorption due to the extremely long establishment of equilibrium (more than 3 days), which makes it impossible to use the BET model and other common models. Similar cases have already been encountered previously [1], so for comparison with the electrochemical determination it was decided to use a geometric estimate and the adsorption of methylene blue. The surface area was estimated geometrically by calculating the lateral area of an ideally smooth cylinder, which was taken to be carbon fiber. For this calculation, it is necessary to know the density of the felt, which was taken to be $1.9 \text{ g} \cdot \text{cm}^{-3}$ based on literary data [1, 2]. The fiber diameter (Fig. 1) of both graphite and carbon felt is the same and is about $20 \mu\text{m}$, which is why the geometric estimate gives a similar result. However, it should be noted that the use of this approximation for sample No. 2 is incorrect due to the presence of a large number of growths on the surface of its fibers (Fig. 2).

Methylene blue adsorption also yields similar surface area values ((4.5 ± 0.7) and $(4.3 \pm 0.4) \text{ m}^2 \cdot \text{g}^{-1}$), which are an order of magnitude higher than the literature data on low-temperature nitrogen adsorption processed using the BET model (Table 3). The fact that surface area values obtained by different methods differ for carbon materials is widely known [2, 40]. In addition, as mentioned above, low-temperature nitrogen adsorption may yield incorrect results. From the electron microscopy data (Fig. 1), it is evident that the felts should have different surface areas, which does not correlate with the results of determination by methylene blue adsorption. This is

explained by the higher content of defects in the structure of sample No. 1 (from the Raman spectra). In [16], it was shown that defects in the structure of the carbon material are methylene blue adsorption centers. In addition, the use of the methylene blue method for determining the specific surface area can give strong errors towards overestimation in the case of the presence of relatively narrow mesopores in the material due to the interaction between molecules and their conformations in the pores.

The electrochemically active surface area determined using the Randles-Shevchik equation is two orders of magnitude lower than the result obtained by adsorption of methylene blue. Apparently, this is connected with the high rate constant of heterogeneous electron transfer to the edge surface of graphite, due to which only the area of the edge plane is determined, whereas dye adsorption yields the total area.

**Fig. 3.** Voltammograms of an empty wire hook (1), sample 1 (2) and sample 2 (3), scanning speed $100 \text{ mV} \cdot \text{s}^{-1}$

This is consistent with the data of [2], in which the surface area according to BET (total area) and the EDL capacitance (edge plane area) are similarly different. The ratio of the EDL capacitances of different felts can be estimated from the appearance of cyclic voltammograms (Fig. 3). In sample No. 2, the peaks are broadened, which indicates high EDL charging currents, from which one can conclude that the EDL capacitance is higher.

To confirm this conclusion, the specific capacity of the EDL of carbon felt was determined using cyclic voltammetry, electrochemical impedance spectroscopy and charge-discharge curves (Table 4).

The values of the EDL specific capacity determined by different methods are in satisfactory agreement with each other. A slight underestimation of the value obtained by the cyclic voltammetry method may be due to the fact that the potential increases faster than the diffusion of ions from the solution, so the EDL is not charged to the maximum possible value [41]. The specific capacity of the EDL for the “Composite-Polymer” felt is higher, which agrees with the qualitative assessment of the ratio of the EDL capacitances based on the shape of the cyclic voltammograms.

To calculate the rate constants using formulas (3) and (5), the surface area determined using the Randles-Shevchik equation was used. It is directly related to the limiting current, from the dependence

of which on the parameter ψ the constant is calculated.

The results obtained by the two methods (Table 5) are quite close to each other and correspond to the literature data, including those obtained using mathematical models [5, 42] and on electrodes consisting of individual fibers [3].

Thus, the data presented in Table 5 shows that there is no need to use complex mathematical models and single-fiber electrodes [3]. According to the literature data, a high error in determination is characteristic of the rate constant of heterogeneous electron transfer [3, 43]. It can be associated with the heterogeneity of the distribution of the marginal and basal plane in different parts of the felt [2].

An important characteristic of electrochemical properties of carbon materials is the ratio of the edge and basal planes of graphite. As was said above, in a number of redox-active systems, electron transfer occurs only on the edge surface. The percentage of the edge plane area was calculated from the values of the heterogeneous transfer rate constant according to equation (2), the capacity of the EDL – according to equation (1), and also from the ratio of the specific surface areas determined by the adsorption of methylene blue and from the Randles-Shevchik equation (Table 6).

Table 4. Results of determining the specific capacity of the EDL of carbon felt

Sample	Specific capacity, F/g		
	Cyclic voltammetry	Charge-discharge curves	Electrochemical impedance spectroscopy (EIS)
1	0.21 ± 0.02	0.26 ± 0.05	0.28 ± 0.02
2	0.35 ± 0.02	0.42 ± 0.04	0.37 ± 0.02

Table 5. Results of determining the rate constant of heterogeneous electron transfer by various methods

Method	Sample No. 1	Sample No. 2	References
$k_s \cdot 10^3, \text{sm} \cdot \text{s}^{-1}, \text{CV}$	3 ± 1	3.1 ± 0.9	7.0 ± 0.5 [1]; 7 ± 3 [3]; 10 [5]
$k_s \cdot 10^3, \text{sm} \cdot \text{s}^{-1}, \text{EIS}$	3 ± 2	3 ± 2	3 ± 2 [5]; 7.7 ± 0.1 [42]

Table 6. Results of determining the content of the boundary plane by various methods

Sample	$k_s, \%$	$C_{\text{EDL}}, \%$	Ratio of specific areas, %
1	3 ± 1	2.7 ± 0.6	1.6 ± 0.4
2	3.1 ± 0.9	6.4 ± 0.9	4,4 ± 0.9

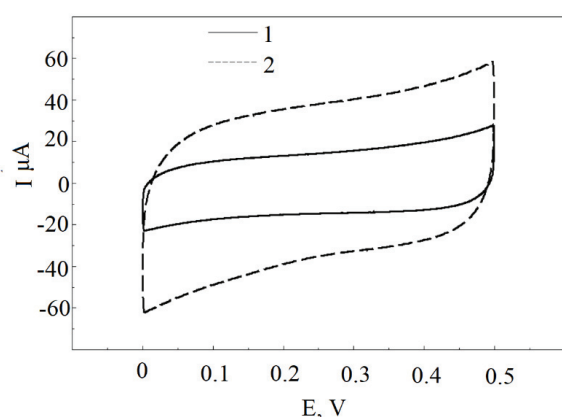


Fig. 4. Cyclic voltammograms of carbon felt in 0.1 M KCl; 1 – Sample No. 1, 2 – Sample No. 2

When calculating the capacity of the EDL, the specific capacity of the edge plane was taken as $70 \mu\text{F}\cdot\text{cm}^{-2}$, since in this case the result obtained is in good agreement with other methods. From the rectangular shape of the cyclic voltammograms of carbon felts (Fig. 4), one can conclude that there is no pseudocapacitance [41], therefore $70 \mu\text{F}\cdot\text{cm}^{-2}$ is the capacity of the EDL in the absence of pseudocapacitance. The distortion of the rectangular shape can be associated with the diffusion of ions to the electrode surface, which limits the charging rate [30].

Calculation from the values of the rate constant of heterogeneous electron transfer does not yield significant differences between the percentage content of the edge plane for the felts. This can be explained by the high error in determining this constant for this material [3, 43]. Calculations by other methods indicate a higher content of the edge plane in sample No. 2 despite the close values of the defect densities according to Raman spectroscopy data. Thus, the rate of electron transfer to the amorphous phase of carbon is low, which may be due to its low electrical conductivity. Charge accumulation also apparently occurs better on more structured graphite defects, which is associated with the formation of conjugated bond systems between quinoid structures.

4. Conclusion

It is shown that in order to obtain the most complete information on the surface area of a carbon material, it is necessary to use several complementary methods for its determination. Calculation of this value from cyclic voltammetry data with the help of the Randles-Shevchik equation, using potassium hexacyanoferrate (III) as an electrochemical sensor, makes it possible to determine predominantly the area

of the edge plane. Geometrical assessment of the surface area and determination by low-temperature gas adsorption should be used with caution. In the case of characterization of electrode materials, the expediency of using these methods is questionable. Comparing the specific surface area obtained by various methods with the results of Raman spectroscopy, it should be noted that electron transfer to amorphized carbon is more difficult than to crystalline carbon, while adsorption of methylene blue, on the contrary, occurs more easily on the amorphous phase.

5. Funding

The work was carried out with the financial support of the Ministry of Science and Higher Education of the Russian Federation within the framework of the state assignment No. FEWG-2024-0003 (Biocatalytic platforms based on microorganism cells, subcellular structures and enzymes in combination with nanomaterials).

6. Acknowledgements

We thank the staff of the Center for Collective Use of Scientific Equipment “Production and Application of Multifunctional Nanomaterials” of Tambov State Technical University for assistance in recording the Raman spectra of the studied samples.

7. Conflict of interests

The authors declare no conflict of interest.

References

1. Smith REG, Davies TJ, Baynes NDB, Nichols RJ. The electrochemical characterisation of graphite felts. *Journal of Electroanalytical Chemistry*. 2015;747:29-38. DOI:10.1016/j.jelechem.2015.03.029
2. Kroner I, Becker M, Turek T. Determination of rate constants and reaction orders of vanadium-ion kinetics on carbon fiber electrodes. *ChemElectroChem*. 2020;7:4314-4325. DOI:10.1002/celec.202001033
3. Landon-Lane L, Downard AJ, Marshall AT. Single fibre electrode measurements – A versatile strategy for assessing the non-uniform kinetics at carbon felt electrodes. *Electrochim Acta*. 2020;136709. DOI:10.1016/j.electacta.2020.136709
4. Wang K, Cao Z, Chang J, Sheng Y, et al. Promoted bioelectrocatalytic activity of microbial electrolysis cell (MEC) in sulfate removal through the synergy between neutral red and graphite felt. *Chemical Engineering Journal*. 2017;327:183-192. DOI:10.1016/j.cej.2017.06.086
5. Feynerol V, El Hage R, Brites Helú M, Fierro V, et al. Comparative kinetic analysis of redox flow battery electrolytes: From micro-fibers to macro-felts.

Electrochimica Acta. 2022;421:140373. DOI:10.1016/j.electacta.2022.140373

6. Maltsev AA, Bibikov SB, Varfolomeev SD, Kalinichenko VN, et al. Determining the specific surface area of carbon electrode materials for electrodes of supercapacitors via the adsorption of methylene blue dye. *Russian Journal of Physical Chemistry A*. 2018;92(4):772-777. DOI:10.1134/S0036024418040209

7. Kuzmina EV, Dmitrieva LR, Karaseva EV, Kolosnitsyn VS. On the possibility of application of the method of sorption of dyes for determining the specific surface area of carbon materials for lithium-sulfur batteries. *Izvestia Ufimskogo nauchnogo tsentra RAN*. 2020;2:29-34. DOI:10.31040/2222-8349-2020-0-2-29-34 (In Russ.)

8. Wen M, Liu H, Zhang F, Zhu Y, et al. Amorphous FeNiPt nanoparticles with tunable length for electrocatalysis and electrochemical determination of thiols. *Chemical Communications*. 2009;30:4530-4532. DOI:10.1039/B907379E

9. Zhu P, Zhao Y. Cyclic voltammetry measurements of electroactive surface area of porous nickel: Peak current and peak charge methods and diffusion layer effect. *Materials Chemistry and Physics*. 2019;233:60-67. DOI:10.1016/j.matchemphys.2019.05.034

10. Zou Y, Walton AS, Kinloch IA, Dryfe RAW. Investigation of the differential capacitance of highly ordered pyrolytic graphite as a model material of graphene. *Langmuir*. 2016;32(44):11448-11455. DOI:10.1021/acs.langmuir.6b02910

11. Rice RJ, McCreery RL. Quantitative relationship between electron transfer rate and surface microstructure of laser-modified graphite electrodes. *Analytical Chemistry*. 1989;61(15):1637-1641. DOI:10.1021/ac00190a010

12. Rice RJ, Pontikos NM, McCreery RL. Quantitative correlations of heterogeneous electron-transfer kinetics with surface properties of glassy carbon electrodes. *Journal of the American Chemical Society*. 1990;112(12):4617-4622. DOI:10.1021/ja00168a001

13. Iamprasertkun P, Hirunpinyopas W, Keerthi A, Wang B, et al. Capacitance of basal plane and edge-oriented highly ordered pyrolytic graphite: specific ion effects. *Journal of Physical Chemistry Letters*. 2019;10(3):617-623. DOI:10.1021/acs.jpcclett.8b03523

14. Yuan W, Zhou Y, Li Y, Li C, et al. The edge- and basal-plane-specific electrochemistry of a single-layer graphene sheet. *Scientific Reports*. 2013;3:2248. DOI:10.1038/srep02248

15. Pandolfo AG, Hollenkamp AF. Carbon properties and their role in supercapacitors. *Journal Power Sources*. 2006;157:11-27. DOI:10.1016/j.jpowsour.2006.02.065

16. McDermott MT, Kneten K, McCreery RL. Anthraquinonedisulfonate adsorption, electron-transfer kinetics, and capacitance on ordered graphite electrodes: the important role of surface defects. *Journal of Physical Chemistry*. 1992;96(7):3124-3130. DOI:10.1021/j100186a063

17. Velický M, Toth PS, Woods CR, Novoselov KS, Dryfe RAW. Electrochemistry of the basal plane versus edge plane of graphite revisited. *Journal of Physical*

Chemistry C. 2019;123(18):11677-11685. DOI:10.1021/acs.jpcc.9b01010

18. Li Y, Li Q, Wang H, Zhang L, et al. Recent progresses in oxygen reduction reaction electrocatalysts for electrochemical energy applications. *Electrochemical Energy Reviews*. 2019;2:518-538. DOI:10.1007/s41918-019-00052-4

19. Ramesh P, Sampath S. Electrochemical characterization of binderless, recompressed exfoliated graphite electrodes: electron-transfer kinetics and diffusion characteristics. *Analytical Chemistry*. 2003;75(24):6949-6957. DOI:10.1021/ac034833u

20. Chen P, McCreery RL. Control of electron transfer kinetics at glassy carbon electrodes by specific surface modification. *Analytical Chemistry*. 1996;68(22):3958-3965. DOI:10.1021/ac960492r

21. Kneten KR, McCreery RL. Effects of redox system structure on electron-transfer kinetics at ordered graphite and glassy carbon electrodes. *Analytical Chemistry*. 1992;64(21):2518-2524. DOI:10.1021/ac00045a011

22. McCreery RL, McDermott MT. Comment on electrochemical kinetics at ordered graphite electrodes. *Analytical Chemistry*. 2012;84:2602-2605. DOI:10.1021/ac2031578

23. Abdelrahim AM, Abd El-Moghny MG, El-Shakre ME, El-Deab MS. High mass loading MnO₂/graphite felt electrode with marked stability over a wide potential window of 1.9 V for supercapacitor application. *Journal of Energy Storage*. 2023;57:106218. DOI:10.1016/j.est.2022.106218

24. Rosolen JM, Matsubara EY, Marchesin MS, Lala SM, et al. Carbon nanotube/felt composite electrodes without polymer binders. *Journal Power Sources*. 2006;162(1):620-628. DOI:10.1016/j.jpowsour.2006.06.087

25. Emmel D, Hofmann JD, Arlt T, Manke I, et al. Understanding the impact of compression on the active area of carbon felt electrodes for redox flow batteries. *ACS Applied Energy Materials*. 2020;3(5):4384-4393. DOI:10.1021/acsam.0c00075

26. Das I, Das S, Ghangrekar MM. Application of bimetallic low-cost CuZn as oxygen reduction cathode catalyst in lab-scale and field-scale microbial fuel cell. *Chemical Physics Letters*. 2020;751:137536. DOI:10.1016/j.cplett.2020.137536

27. Randviir EP. A cross examination of electron transfer rate constants for carbon screen-printed electrodes using Electrochemical Impedance Spectroscopy and cyclic voltammetry. *Electrochimica Acta*. 2018;286:179-186. DOI:10.1016/j.electacta.2018.08.021

28. Lavagnini I, Antiochia R, Magno F. An extended method for the practical evaluation of the standard rate constant from cyclic voltammetric data. *Electroanalysis*. 2004;16(6):505-506. DOI:10.1002/elan.200302851

29. Lazanas AC, Prodromidis MI. Electrochemical impedance spectroscopy – A Tutorial. *ACS Measurement Science Au*. 2022;3:162-193. DOI:10.1021/acsmeasuresciau.2c00070

30. Wei L, Sevilla M, Fuertes AB, Mokaya R, Yushin G. Hydrothermal carbonization of abundant renewable natural organic chemicals for high-performance supercapacitor electrodes. *Advanced Energy Materials*. 2011;1(3):356-361. DOI:10.1002/aenm.201100019
31. Li Z, Deng L, Kinloch IA, Young RJ. Raman spectroscopy of carbon materials and their composites: Graphene, nanotubes and fibres. *Progress in Materials Science*. 2023;135. DOI:10.1016/j.pmatsci.2023.101089
32. Chernyak SA, Ivanov AS, Stolbov DN, Egorova TB, et al. N-doping and oxidation of carbon nanotubes and jellyfish-like graphene nanoflakes through the prism of Raman spectroscopy. *Applied Surface Science*. 2019;488:51-60. DOI:10.1016/j.apsusc.2019.05.243
33. Ghosh S, Ganesan K, Polaki SR, Ravindran TR, et al. Evolution and defect analysis of vertical graphene nanosheets. *Journal of Raman Spectroscopy*. 2014;45(8):642-649. DOI:10.1002/jrs.4530
34. Bonpua J, Yagües Y, Aleshin A, Dasappa S, Camacho J. Flame temperature effect on sp² bonds on nascent carbon nanoparticles formed in premixed flames (T_{f,max} > 2100 K): A Raman spectroscopy and particle mobility sizing study. *Proceedings of the Combustion Institute*. 2019;37(1):943-951. DOI:10.1016/j.proci.2018.06.124
35. Caçado LG, Jorio A, Ferreira EHM, Stavale F, et al. Quantifying defects in graphene via Raman spectroscopy at different excitation energies. *Nano Letters*. 2011;11(8):3190-3196. DOI:10.1021/nl201432g
36. Ribeiro-Soares J, Oliveros ME, Garin C, David MV, et al. Structural analysis of polycrystalline graphene systems by Raman spectroscopy. *Carbon*. 2015;95:646-652. DOI:10.1016/j.carbon.2015.08.020
37. Eckmann A, Felten A, Mishchenko A, Britnell L, et al. Probing the nature of defects in graphene by Raman spectroscopy. *Nano Letters*. 2012;12:3925-3930. DOI:10.1021/nl300901a
38. Venezuela P, Lazzeri M, Mauri F. Theory of double-resonant Raman spectra in graphene: Intensity and line shape of defect-induced and two-phonon bands. *Physical Review B – Condensed Matter and Materials Physics*. 2011;84:035433. DOI:10.1103/PhysRevB.84.035433
39. Ferrari AC, Basko DM. Raman spectroscopy as a versatile tool for studying the properties of graphene. *Nature Nanotechnology*. 2013;8:235-246. DOI:10.1038/nnano.2013.46
40. Huang Le TX, Bechelany M, Cretin M. Carbon felt based-electrodes for energy and environmental applications: A review. *Carbon*. 2017;122:564-591. DOI:10.1016/j.carbon.2017.06.078
41. Morales DM, Risch M. Seven steps to reliable cyclic voltammetry measurements for the determination of double layer capacitance. *JPhys Energy*. 2021;3(3):034013. DOI:10.1088/2515-7655/abee33
42. Landon-Lane L, Marshall AT, Harrington DA. EIS at carbon fiber cylindrical microelectrodes. *Electrochemistry Communications*. 2019;109:106566. DOI:10.1016/j.elecom.2019.106566
43. Rabbow TJ, Trampert M, Pokorny P, Binder P, Whitehead AH. Variability within a single type of polyacrylonitrile-based graphite felt after thermal treatment. Part II: Chemical properties. *Electrochimica Acta*. 2015;173:24-30. DOI:10.1016/j.electacta.2015.05.058

Information about the authors / Информация об авторах

Pavel V. Oskin, Junior Researcher, Tula State University (TulSU), Tula, Russian Federation; ORCID 0000-0001-9308-6496; e-mail: pavelfraj@yandex.ru

Roman V. Lepikash, Junior Researcher, TulSU, Tula, Russian Federation; ORCID 0000-0001-7853-2937; e-mail: mr.romalep@yandex.ru

Tatyana P. Dyachkova, D. Sc. (Chem.), Professor, Tambov State Technical University, Tambov, Russian Federation; ORCID 0000-0002-4884-5171; e-mail: dyachkova_tp@mail.ru

Sergey V. Alferov, Cand. Sc. (Chem.), Associate Professor, Head of the Laboratory, TulSU, Tula, Russian Federation; ORCID 0000-0002-5217-7815; e-mail: s.v.alferov@gmail.com

Оськин Павел Владимирович, младший научный сотрудник, Тульский государственный университет (ТулГУ), Тула, Российская Федерация; ORCID 0000-0001-9308-6496; e-mail: pavelfraj@yandex.ru

Лепикаш Роман Владимирович, младший научный сотрудник, ТулГУ, Тула, Российская Федерация; ORCID 0000-0001-7853-2937; e-mail: mr.romalep@yandex.ru

Дьячкова Татьяна Петровна, доктор химических наук, профессор, Тамбовский государственный технический университет, Тамбов, Российская Федерация; ORCID 0000-0002-4884-5171; e-mail: dyachkova_tp@mail.ru

Алферов Сергей Валерьевич, кандидат химических наук, доцент, заведующий лабораторией, ТулГУ, Тула, Российская Федерация; ORCID 0000-0002-5217-7815; e-mail: s.v.alferov@gmail.com

Received 13 May 2024; Accepted 14 August 2024; Published 22 October 2024



Copyright: © Oskin PV, Lepikash RV, Dyachkova TP, Alferov SV, 2024. This article is an open access article distributed under the terms and conditions of the Creative Commons Attribution (CC BY) license (<https://creativecommons.org/licenses/by/4.0/>).

Removal of organic dyes from aqueous solutions using a graphene-containing sorbent based on activated rapeseed biochar: kinetics and isotherms

© Alexey N. Timirgaliev^a, Irina V. Burakova^a✉, Sofya O. Rybakova^a, Oksana A. Ananyeva^a, Vladimir O. Yarkin^a, Tatyana S. Kuznetsova^a, Ali H. K. Kadum^a, Alexander E. Burakov^a

^a Tambov State Technical University,
Bld. 2, 106/5, Sovetskaya St., Tambov, 392000, Russian Federation

✉ iris_tamb68@mail.ru

Abstract: The paper deals with the development of a graphene-containing sorbent material based on activated rapeseed biochar. The physicochemical properties of the sorbent and features of its morphological structure were determined. The nanocomposite was found to have amorphous properties with a graphene-like structure. The morphological analysis confirmed the formation of internal carbon framework and external three-dimensional multilayer graphene structure, which is excellent for mass transfer between pollutants and adsorbent surface. The research also aimed to determine the important parameters of sorption of organic compounds, i.e. synthetic dyes Congo Red (CR) and Malachite Green (MG), on the developed material from aqueous solutions in a limited volume. According to the kinetic studies, the experimental sorption capacity of the material on MG was $1860 \text{ mg}\cdot\text{g}^{-1}$ (sorption time – 60 min) and $642 \text{ mg}\cdot\text{g}^{-1}$ on CR (sorption time – 15 min). The theoretical maximum adsorption capacity of the sorbent calculated by the Langmuir model reached values of $769.23 \text{ mg}\cdot\text{g}^{-1}$ for CR and $3333.33 \text{ mg}\cdot\text{g}^{-1}$ for MG. It is found that the extraction of dye molecules is controlled by the second-order reaction according to the pseudo-second-order model and proceeds mainly by a mixed-diffusion mechanism. The activation energy has a value of $0.01 \text{ kJ}\cdot\text{mol}^{-1}$ for CR molecules and $0.02 \text{ kJ}\cdot\text{mol}^{-1}$ for MG, confirming the physical mechanism of dye adsorption. The high efficiency of adsorption of organic dyes on graphene-containing sorption material based on activated rapeseed biochar was demonstrated, indicating the feasibility of its practical application in wastewater treatment.

Keywords: graphene oxide; activated carbon; biochar; rapeseed; synthetic dyes; Congo Red; Malachite Green; adsorption; kinetics; isotherms.

For citation: Timirgaliev AN, Burakova IV, Rybakova SO, Ananyeva OA, Yarkin VO, Kuznetsova TS, Kadum AHK, Burakov AE. Removal of organic dyes from aqueous solutions using a graphene-containing sorbent based on activated rapeseed biochar: Kinetics and isotherms. *Journal of Advanced Materials and Technologies*. 2024;9(3):177-187. DOI: 10.17277/jamt.2024.03.pp.177-187

Удаление органических красителей из водных растворов с помощью графенсодержащего сорбента на основе активированного рапсового биоугля: кинетика и изотермы

© А. Н. Тимиргалиев^a, И. В. Буракова^a✉, С. О. Рыбакова^a, О. А. Ананьева^a, В. О. Яркин^a, Т. С. Кузнецова^a, А. Х. К. Кадум^a, А. Е. Бураков^a

^a Тамбовский государственный технический университет,
ул. Советская, 106/5, пом. 2, Тамбов, 392000, Российская Федерация

✉ iris_tamb68@mail.ru

Аннотация: В статье разработан графенсодержащий сорбционный материал на основе активированного рапсового биоугля, определены физико-химические свойства сорбента и особенности его морфологического строения. Установлено, что наноккомпозит имеет аморфные характеристики с графеноподобной структурой. Морфологический анализ подтвердил образование внутреннего углеродного каркаса и внешней трехмерной многослойной графеновой структуры, которая превосходно подходит для массопереноса между загрязнителями

и поверхностью адсорбента. Также целью исследований являлось определение важных параметров сорбции органических соединений – синтетических красителей конго красного (КК) и малахитового зеленого (МЗ), на разработанном материале из водных растворов в ограниченном объеме. Согласно кинетическим исследованиям, экспериментальная сорбционная емкость материала по МЗ составила 1860 мг/г (время сорбции 60 мин) и 642 мг/г по КК (время сорбции 15 мин). Теоретическая максимальная адсорбционная емкость сорбента, рассчитанная по модели Ленгмюра, достигла значений 769,23 мг/г по КК и 3333,33 мг/г по МЗ. Обнаружено, что извлечение молекул красителей контролируется реакцией второго порядка согласно модели псевдо-второго порядка и проходит преимущественно по смешанно-диффузионному механизму. Энергия активации имеет значение 0,01 кДж/моль по молекулам КК и 0,02 кДж/моль для МЗ, что подтверждает физический механизм поглощения красителей. В целом, в работе показана высокая эффективность адсорбции органических красителей на графенсодержащем сорбционном материале на основе активированного рапсового биоугля, что позволяет говорить о целесообразности его практического применения при очистке сточных вод.

Ключевые слова: оксид графена; активированный уголь; биоуголь; рапс; синтетические красители; конго красный; малахитовый зеленый; адсорбция; кинетика; изотермы.

Для цитирования: Timirgaliev AN, Burakova IV, Rybakova SO, Ananyeva OA, Yarkin VO, Kuznetsova TS, Kadum ANK, Burakov AE. Removal of organic dyes from aqueous solutions using a graphene-containing sorbent based on activated rapeseed biochar: Kinetics and isotherms. *Journal of Advanced Materials and Technologies*. 2024;9(3): 177-187. DOI: 10.17277/jamt.2024.03.pp.177-187

Introduction

According to a recent World Health Organization (WHO) report, nearly 844 million people worldwide do not have access to safe drinking water [1]. Dye-containing wastewater from the textile industry poses an increasing risk to human life and aquatic organisms when discharged into various water bodies, as most of the types of dyes found in dyeing wastewater are toxic and carcinogenic [2]. In addition, these dyes interfere with light penetration and oxygen transport in water bodies [3].

Malachite Green (MG) and Congo Red (CR) together account for a significant proportion of the organic dyes produced and used annually that pose significant health risks. MG is known for its potential teratogenic and carcinogenic properties, which can cause damage to vital organs such as the liver, kidney and heart [4]. CR is classified as an anionic diazo dye and is one of the most commonly used dyes [5]. Unfortunately, decomposition of CR under anaerobic conditions leads to the formation of benzidine, a known human carcinogen [6]. It is therefore crucial to remove organic dyes that pollute the environment's water resources in order to mitigate their harmful effects on humans, flora and fauna.

In their study, Ohemeng-Boahen et al. [6] presented a number of approaches for the removal of dye molecules, including adsorption, coagulation-flocculation, co-deposition, membrane separation, ion exchange, and photo- and biodegradation. Adsorption is regarded as an efficacious method for the elimination of dyes from wastewater, due to its advantageous characteristics, including flexibility, operational simplicity and economic viability [7]. At present, a variety of adsorbents are employed for

the removal of dyes, including biochar, activated carbon composites, nanoparticles, polymers, resins, clays, minerals and biosorbents [8].

Among the range of available adsorbents, activated carbon is undoubtedly considered the most versatile for use in studies of dye removal due to its low cost, excellent adsorption capacity, environmental friendliness and good surface characteristics [7]. Biochar is a bioorganic biomass produced by carbonization of carbon-rich materials. The modern low-temperature biomass processing method is hydrothermal carbonization (HTC), which is considered a green technology because of the absence of harmful gas emissions. The distinctive feature of this process is the relatively mild conditions under which it is carried out, in comparison with the well-studied pyrolysis process [8–10].

Many scientific teams are engaged in the development of new sorbents. They demonstrate remarkable efficacy in removing organic dyes from liquids (Fig. 1).

Thus, a number of materials of different chemical nature have been used for MG adsorption, for example: activated carbon with zinc oxide decorated with plantain peel [11]; magnetic mesoporous core-shell nanostructure $Ni_{0.4}Fe_{2.6}O_4/(Fe, Ni)$ with carbon [12]; chemically activated biochar from Indian bael peel [13]; functionalized biochar from banana peel [14]; halloysite nanotubes [15]; β -cyclodextrin nanocomposite based on polymer with zinc ferrite nanofiller [16]. For CR removal the following are used: β -cyclodextrin polyurethane insoluble nanosponge modified with phosphorylated multi-walled carbon nanotubes and additionally decorated with titanium dioxide and silver nanoparticles [17];

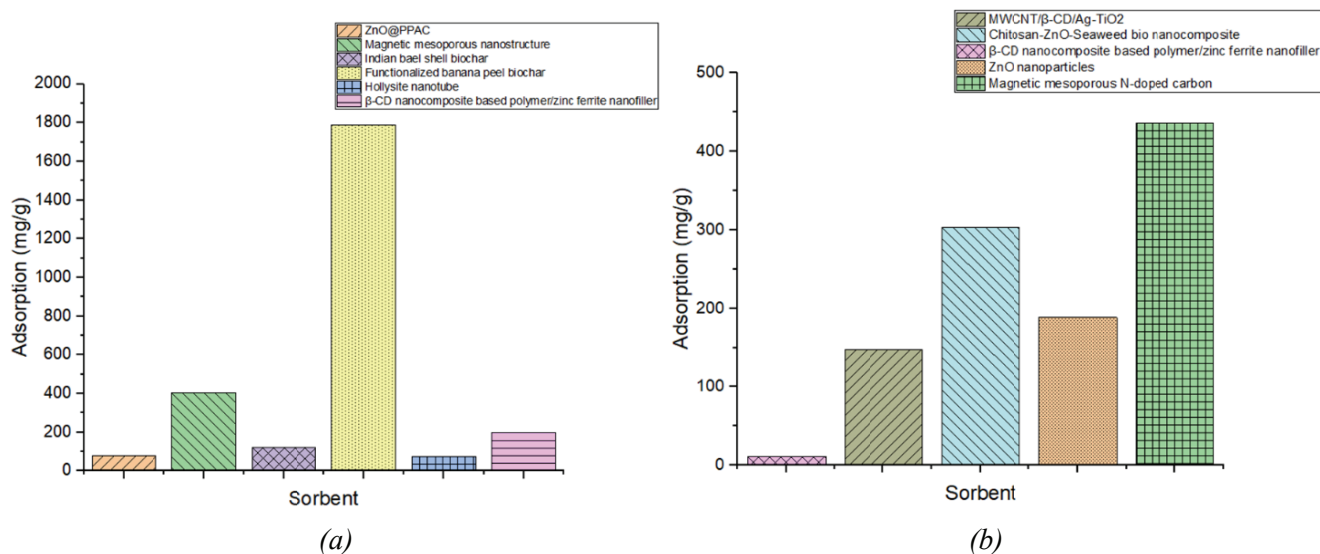


Fig. 1. Literature data on the sorption of MG (a) and CR (b) on different types of sorbents and their sorption capacity

bionanocomposite consisting of chitosan, zinc oxide, algae [18]; β -cyclodextrin nanocomposite based on polymer containing zinc ferrite nanofiller [16]; zinc oxide nanoparticles [19]; magnetic and mesoporous N-doped carbon [20].

The aim of the present work is to synthesize and evaluate the physicochemical properties of graphene-containing activated biochar based on vegetable waste from rapeseed processing and to determine the mechanisms of removal of organic contaminants – CR and MG dyes – using the developed material.

2. Materials and Methods

2.1. Material's synthesis

Rapeseed meal (originating from Tambov region, Russia) was used as a carbon source. The modifier was graphene oxide (GO) in the form of aqueous 1 wt. % suspension (NanoTechCenter LLC, Tambov). Biochar was obtained by hydrothermal carbonization in stainless steel autoclaves for 12 hours at 180 °C. The obtained hydrocoal was separated from the liquid by filtration. Further, the filtered material was carbonized in stages at 150, 500 and 750 °C for one hour at each temperature in argon atmosphere. The carbonized material was subjected to alkaline activation, for this purpose it was mixed with potassium hydroxide (KOH) in a mass ratio of 1:6. The process was carried out in an inert environment at 400 and 750 °C for one hour at each temperature. The resulting material was washed with distilled water on a filter to a neutral pH, and then incubated for 24 hours in concentrated hydrochloric acid (Russian Standard 3118-77). Then the biochar was washed again to neutral pH and dried at 110 °C to constant weight.



Fig. 2. Physical appearance of graphene-containing sorbent based on rapeseed

To obtain a nanocomposite sorbent, activated biochar was mixed with a suspension of GO to a homogeneous state (ratio 1.5:1) and then treated with ultrasound. The material was placed in autoclaves and incubated at 180 °C for 20 hours. In the next step, the composite was frozen to –30 °C in a lyophilic dryer (Scientz-10n, China), followed by lyophilization for 48 h, during which the solvent was removed by the freeze-drying. The final material was a spontaneously compacted product (see Fig. 2).

2.2. Analytical methods

Microphotographs were obtained using an AURIGA CrossBeam scanning electron microscope (SEM) with Inca X-Max 80 mm² EDS (Carl Zeiss Group, Germany). Thermo Scientific ARL Equinox 1000 (TechTrend Science Co., Ltd., Taiwan) ($\lambda = 0.1540562$ nm (copper anode) was used to identify

the crystal structure of the material. The orderliness of the carbon framework was evaluated by Raman spectroscopy on a DXR Raman Microscope instrument (Thermo Scientific Instruments Group, Waltham, USA) ($\lambda = 633$ nm). IR spectra were obtained on a Jasco FT/IR 6700 FTIR spectrometer (Jasco International Co., Ltd., Japan) in the frustrated total internal reflection mode.

2.3. Kinetic research

To determine the kinetic parameters of CR and MG adsorption, experiments were performed under static conditions; for this purpose, 0.01 g of nanocomposite was taken, the initial concentration of CR and MG dye solutions was $1500 \text{ mg}\cdot\text{L}^{-1}$, and the solution volume was 30 mL. The solutions were stirred for 5, 10, 15, 30, 60 and 90 min at 100 rpm and room temperature on a Multi Bio RS-24 rotator (Biosan) and then filtered.

2.4. Isotherm study

To plot adsorption isotherms, 0.01 g of nanocomposite was added to 30 mL of CR and MG dye solution with initial concentrations of 300, 500, 750, 750, 1000, 1200, and $1500 \text{ mg}\cdot\text{L}^{-1}$, shaken for 15 min for CR and 60 min for MG at 100 rpm and room temperature on a Multi Bio RS-24 programmable rotator (Biosan). In all sorption experiments, the amount of dye in the liquid phase before and after adsorption was determined spectrophotometrically (Ekros, St. Petersburg, Russia) at wavelengths of 612 and 709 nm for CR and MG, respectively.

3. Results and Discussion

3.1. Physicochemical properties and morphology of the graphene-containing sorbent

SEM images (Fig. 3) of the nanocomposite sorbent indicate that the material has a rather loose structure. The carbon backbone of the biochar is predominantly covered with graphene sheets. Individual aggregates of micrometer-sized graphene sheets are also found.

The IR spectrum of the nanocomposite (Fig. 4a) contains peaks indicating the presence of sorbed water (broad peak in the region of 3400 cm^{-1}), C–H bonds in alkyl fragments ($2924, 2854 \text{ cm}^{-1}$), C=O (1645 cm^{-1}), aromatic ring bonds at 1564 cm^{-1} , C–O (group of peaks in the region of $1100\text{--}1265 \text{ cm}^{-1}$), and phosphorus-containing compounds (873 cm^{-1}). The obtained data correlate well with the information on the chemical nature of carbon structures in the scientific literature [21–23].

According to Raman spectroscopy (Fig. 4b), the composition of the broad peak in the region $1000\text{--}1650 \text{ cm}^{-1}$ includes the *G* band (around 1590 cm^{-1}) and *D* band (at 1350 cm^{-1}). A second-order overtone of the *D* band, the *2D* band at 2670 cm^{-1} , can also be distinguished. Since the *2D* band arises from the two-phonon double resonance process, it is closely related to the zone structure of graphene layers [24]. The I_D/I_G ratio is > 1 , indicating a high content of sp^3 -hybridized carbon atoms in the material.

The X-ray spectrum (Fig. 5) shows blurred peaks at 26° and 47° , indicating the presence of 002 and 100 planes of graphene materials. The absence of sharp peaks in the spectra suggests that the nanocomposite has amorphous characteristics with graphene-like structure [23].

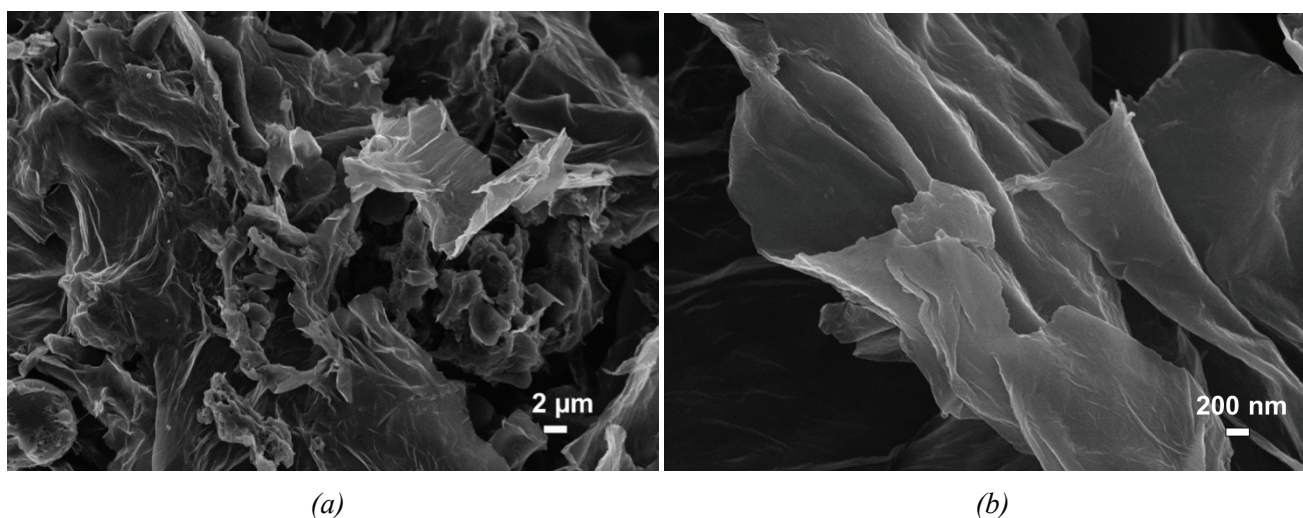


Fig. 3. SEM images of the nanocomposite: *a* – magnification $\times 5,000$; *b* – magnification $\times 50,000$

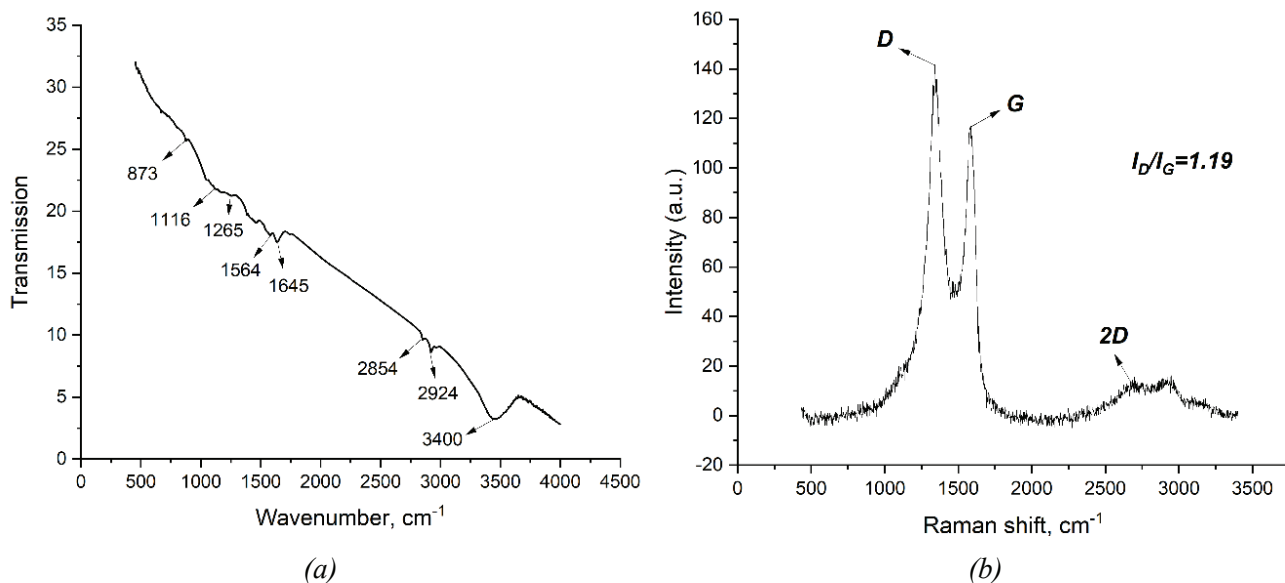


Fig. 4. FTIR (a) and Raman (b) spectra of the nanocomposite from rapeseed plant waste

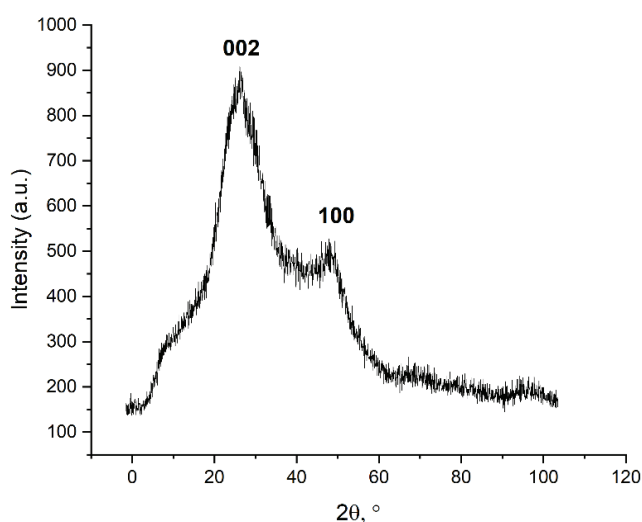


Fig. 5. X-ray diffraction pattern of the nanocomposite from rapeseed plant waste

3.2. Sorption kinetics of organic dyes

Based on the experimental results, the kinetic dependencies of the adsorption of CR and MG on the developed nanocomposite were plotted (Fig. 6a). The experimental values of the adsorption capacity of the material with respect to MG were $1860 \text{ mg}\cdot\text{g}^{-1}$ and $642 \text{ mg}\cdot\text{g}^{-1}$ for CR. It should be noted that the equilibrium of the adsorption process for CR adsorption is reached in 15 min. The extraction of MG is slower – saturation of the sorbent is reached in 60 min.

The kinetic analysis identifies the mechanism of adsorption and the factor determining its rate. The experimental data were analyzed using pseudo-first order, pseudo-second order, Elovich and

intraparticle diffusion models. The equations of these models are given in Table 1.

The pseudo-first and pseudo-second order models allow the determination of the pollutant uptake rate – the values of the sorption rate constants k_1 and k_2 . The pseudo-first order model characterises the processes occurring during the initial period of sorption and the pseudo-second order model describes the extraction mechanism for the entire period. The theoretical equation of intraparticle diffusion takes into account the rate of the internal mass transfer stage, i.e. the diffusion of sorbate in the pores of the sorbent with a spherical particle shape. In this case, if the graph of the dependence of Q_t on $t^{1/2}$ passes through the origin, intraparticle diffusion is the rate-controlling stage. The Elovich model suggests the presence of chemical heterogeneity of the sorbent surface, which favors chemical adsorption. When the experimental data are described by this equation, the adsorption process is chemical in nature [25].

Table 2 summarizes the results of the mathematical evaluation of the experimental kinetic data.

It was found (Fig. 6, Table 2) that the adsorption of MG and CR dye molecules is satisfactorily described by the pseudo-second-order and intraparticle diffusion models. The correlation of the experimental data according to the pseudo-second-order model (Fig. 6c) for CR sorption is $R^2 = 0.9999$ with the value of $Q_e = 667 \text{ mg}\cdot\text{g}^{-1}$. For MG molecules, $Q_e = 2000 \text{ mg}\cdot\text{g}^{-1}$ with $R^2 = 0.9966$. The theoretical value of Q_e by the pseudo-second-order model for both dyes is very close to the sorption capacity obtained experimentally.

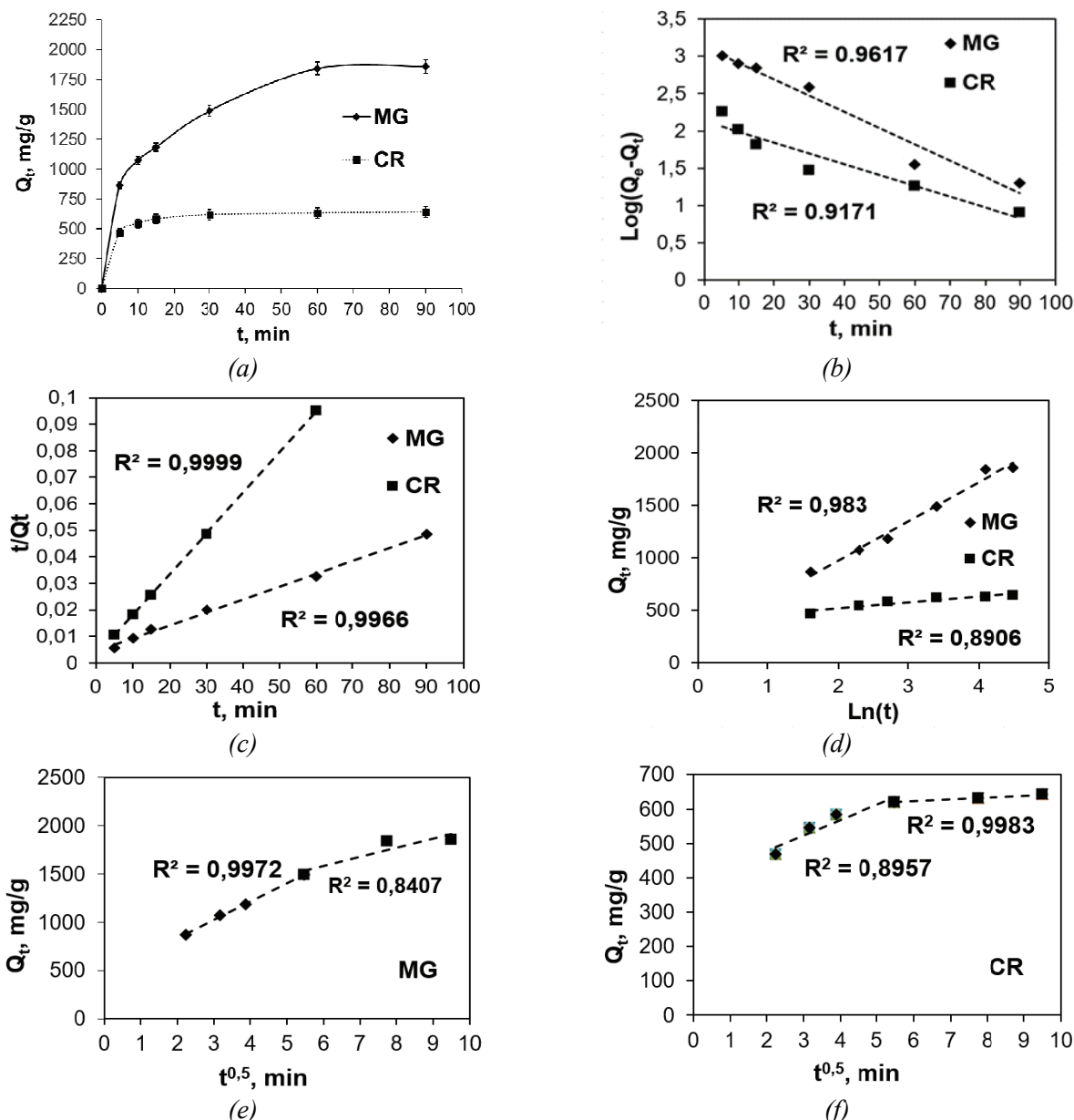


Fig. 6. Adsorption kinetics of CR and MG molecules on the nanocomposite (a), linearized forms of kinetic dependences by pseudo-first (b) and pseudo-second-order (c); Elovich (d); intraparticle diffusion (e, f) models

Table 1. Equations and parameters of different kinetic models [22]

Model	Parameters
Pseudo-first-order model $\ln(Q_e - Q_t) = \ln Q_e - k_1 t$	Q_e and Q_t ($\text{mg} \cdot \text{g}^{-1}$) are the amount of lead ions adsorbed at equilibrium and at any time t (min), respectively; k_1 is the rate constant of the pseudo-first-order (min^{-1}) equation
Pseudo-second-order model $\frac{t}{Q_t} = \frac{1}{k_2 Q_e^2} + \frac{t}{Q_e}$	k_1 ($\text{g} \cdot (\text{mg} \cdot \text{min})^{-1}$) is the rate constant of the pseudo-second-order equation
Elovich model $Q_t = \frac{1}{\beta} \ln(1 + \alpha \beta t)$	α ($\text{mg} \cdot \text{g}^{-1} \cdot \text{min}$) is the initial adsorption rate; β ($\text{g} \cdot \text{mg}^{-1}$) is the adsorption constant related to the degree of surface coverage and the activation energy of chemisorptions
Intraparticle diffusion model $Q_t = k_{id} t^{1/2} + C$	k_{id} ($\text{mg} \cdot \text{g}^{-1} \cdot \text{min}^{1/2}$) is the rate constant of intraparticle diffusion; C is a constant related to the boundary layer thickness at the surface of the sorbent particle

Table 2. Kinetic parameters of organic dyes sorption

Dye	Model parameters					
	Pseudo-first order			Pseudo-first order		
	Q_e	k_1	R^2	Q_e	k_2	R^2
CR	152.4	0.0332	0.9171	667	0.000776	0.9999
MG	1349.9	0.0502	0.9617	2000	0.000056	0.9966
	Elovich equation			Intraparticle diffusion Step 1/Step 2		
	α	β	R^2	k_{id}	C	R^2
CR	71517.1	0.0018	0.891	44.98/5.427	388.71/590.22	0.8957/0.9983
MG	1129.03	0.0043	0.983	189.77/95.37	454.55/1009.6	0.9972/0.8407

According to Fig. 6b, rather low values of the coefficients ($R^2 = 0.9171$; 0.9617) of the pseudo-first order model suggest a weak chemical interaction between the molecules of the CR and MG dyes and the functional groups of the nanocomposite. The Elovich model shows a low correlation with the experimental data, again suggesting that mainly physical adsorption takes place [26].

The Q_t vs. t dependence is not a straight line through the origin of the coordinates, indicating that internal diffusion is not the limiting stage of adsorption. This may be due to the difference in mass transfer rate at the initial and final stages of sorption, i.e. the adsorption of dye molecules has a mixed-diffusion character [25].

3.3. Isotherm study

There are many models that can be used to interpret sorption isotherms, but the usefulness and accuracy of a particular model depends on the

underlying assumptions, as no model works for all adsorption systems. Among these models, the Freundlich and Langmuir models are the most widely used [26, 27]. The Langmuir isotherm assumes that adsorption results in the formation of a monolayer of adsorbate on the adsorbent surface. In contrast, the Freundlich model describes multilayer adsorption with an exponential decrease in the energy distribution of the adsorbed centers [28] (Table 3).

The Temkin isotherm model allows the activity of the sorbent surface centers to be estimated, with the activity of each of them decreasing as a result of the appearance of a number of surface sorption complexes. The more such complexes, the more the initial activity of that center changes. Thus, the activity of each center decreases as the degree of surface coverage by adsorbate increases.

Table 3. Equations and parameters of different isotherm models [26–28]

Model	Parameters
The Langmuir model $\frac{1}{Q_e} = \frac{1}{Q_{\max}} + \frac{1}{Q_{\max} K_L C_e}$	Q_e (mg·g ⁻¹) is the amount of metal ions adsorbed at equilibrium; the Q_{\max} (mg·g ⁻¹) is the maximum adsorption under experimental conditions; C_e (mg·L ⁻¹) is the equilibrium concentration; K_L (L·mg ⁻¹) is a constant related to the adsorption rate
The Freundlich model $\lg Q_e = \frac{1}{n} \lg C_e + \lg k$	k (mg·g ⁻¹ ·(L·mg ⁻¹)); $1/n$ are constants measuring adsorption capacity and intensity, respectively; n indicates how favorable the adsorption process is
The Temkin model $Q_e = B \ln(k_t) + B \ln(C_e)$	k_t (L·mg ⁻¹) is an equilibrium coupling constant corresponding to the maximum binding energy; B (J·mol ⁻¹) is a constant related to the heat of adsorption
The Dubinin–Radushkevich model $\lg Q_e = \ln Q_{\max} - K_{ad} \varepsilon^2;$ $E = \frac{1}{\sqrt{-2k_{ad}}}$	k_{ad} (mol ² ·kJ ⁻²) is the constant of Dubinin–Radushkevich isotherm; ε (kJ·mol ⁻¹) is the Polanyi potential reflecting the isothermal work of transfer of one mole of metal from the volume of equilibrium solution to the sorbent surface; E (kJ·mol ⁻¹) is the activation energy

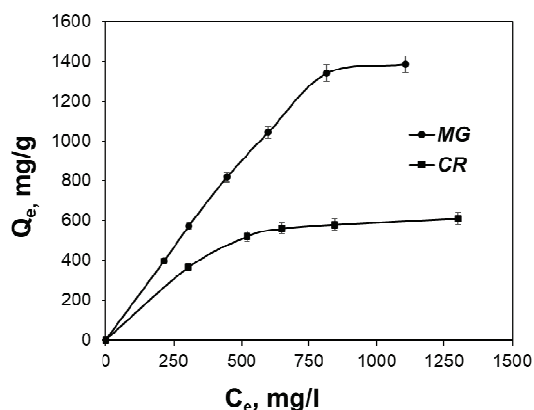


Fig. 7. Adsorption isotherms of CR and MG dyes on the nanocomposite

Using the Dubinin-Radushkevich model, calculations of activation energy are made, which determine the nature of interaction of pollutant forces with active centers. At activation energy values $E < 8 \text{ kJ}\cdot\text{mol}^{-1}$, physical adsorption takes place; at $8 < E < 16 \text{ kJ}\cdot\text{mol}^{-1}$, chemisorption takes place [29].

Fig. 7 shows the experimental adsorption isotherms of CR and MG dyes on the developed nanocomposite.

As a result of the mathematical processing of the experimental data, the dependences shown in Fig. 8 were obtained, which made it possible to determine such important adsorption parameters as maximum adsorption capacity, activation energy, etc. (see Table 4).

The experimental isotherm of MG sorption shows a good correlation with the theoretical data of the Dubinin-Radushkevich equation. The adsorption of CR is satisfactorily described by the Temkin model. At the same time, the activation energy of sorption of MG molecules was $0.02 \text{ kJ}\cdot\text{mol}^{-1}$ (Table 4). According to the calculated values, the maximum adsorption capacity of the nanocomposite according to the Langmuir model was $3333.33 \text{ mg}\cdot\text{g}^{-1}$ for MG and $769.23 \text{ mg}\cdot\text{g}^{-1}$ for CR. The value of the activation energy of sorption of CR molecules was $0.01 \text{ kJ}\cdot\text{mol}^{-1}$, which also corresponds to physical sorption in the case of removal of MG molecules.

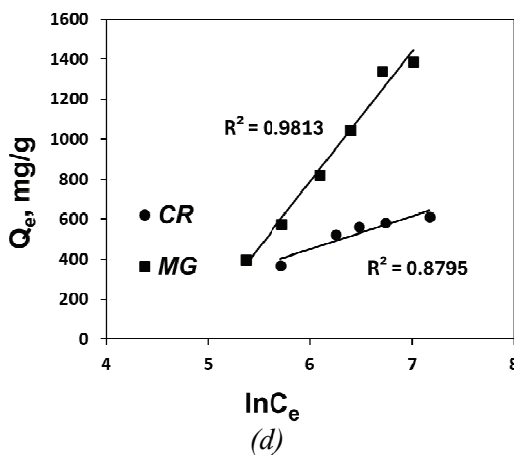
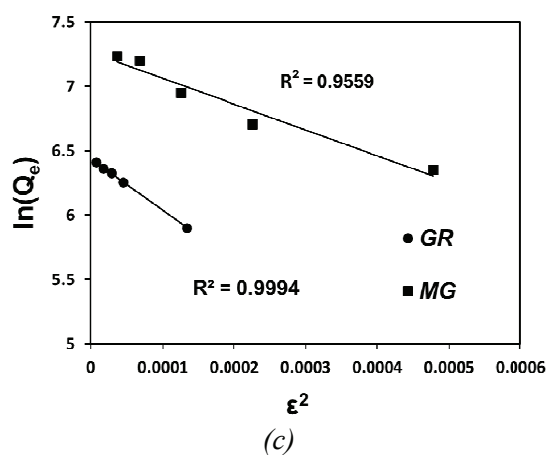
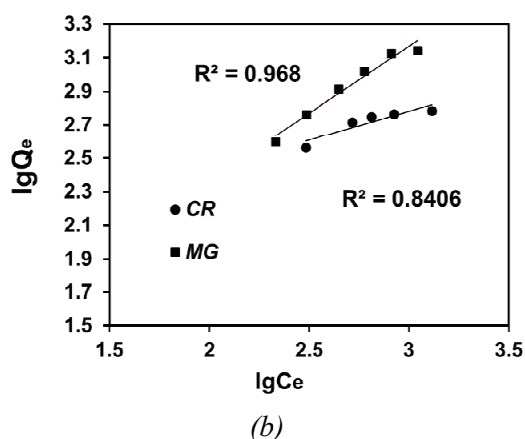
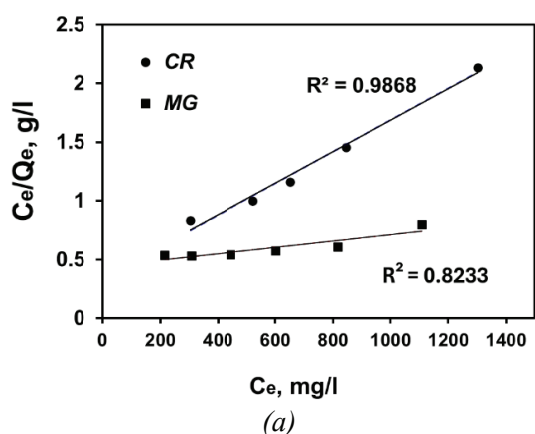


Fig. 8. Models of adsorption isotherms of CR and MG: a – Langmuir; b – Freundlich; c – Dubinin–Radushkevich; d – Temkin

Table 4. Sorption parameters of CR and MG molecules according to the equations of isotherms

Dye	Model parameter			
	<i>Langmuir</i>			
	K_L	Q_{\max}	R^2	
CR	0.0038	769.23	0.9868	
MG	0.0007	3333.33	0.8233	
	<i>Freindlich</i>			
	n	$1/n$	k	R^2
CR	2.891	0.3459	55.386	0.9868
MG	1.2596	0.7939	6.073	0.8233
	<i>Dubinin–Radushkevich</i>			
	k_{ad}	Q_{\max}	E	R^2
CR	4053.6	629.34	0.01	0.9994
MG	2018.5	1438.12	0.02	0.9559
	<i>Temkin</i>			
	k_t	B	R^2	
CR	0.0091	116.2	0.8795	
MG	0.0084	652.2	0.9813	

4. Conclusion

In this paper, the technique for obtaining a highly efficient sorbent material based on activated biochar from rapeseed waste modified with graphene oxide during hydrothermal carbonization has been developed. According to the results of the evaluation of the nanocomposite's properties, it was found that the material has a porous carbon framework, the surface of which is covered with sheets of graphene. X-ray diffraction analysis confirmed the formation of a graphene-like carbon structure of the sorbent. The authors studied the adsorption of synthetic organic dyes from aqueous solutions on the developed material. Kinetic and isothermal studies of adsorption of CR and MG dye molecules were carried out in static mode. It was found that the sorption equilibrium is reached in 60 min for MG and in 15 min for CR with sorption capacity values of $1860 \text{ mg}\cdot\text{g}^{-1}$ for MG and $642 \text{ mg}\cdot\text{g}^{-1}$ for CR. It was found that the sorption is satisfactorily described by the pseudo-second-order model and intraparticle diffusion, with diffusion into the sorbent pores not being a limiting factor. Both external and internal diffusion contribute to the total sorption rate of the dye molecules. Data from isothermal studies were processed using the Langmuir, Freundlich, Dubinin–Radushkevich and Temkin models. The calculated activation energy values confirm the physical mechanism of sorption.

5. Funding

The study was supported by the Russian Science Foundation grant No. 22-13-20074, <https://rscf.ru/project/22-13-20074/>.

6. Acknowledgments

This work was done using facilities of the shared access center “Production and application of multifunctional nanomaterials” (Tambov State Technical University).

7. Conflict of interests

The authors declare no conflict of interests.

References

1. Wutich A, Rosinger AY, Stoler J, Jepson W, et al. Measuring human water needs. *American Journal of Human Biology*. 2020;32(1):e23350. DOI:10.1002/ajhb.23350
2. Berradi M, Hsissou R, Khudhair M, Assouag M, et al. Textile finishing dyes and their impact on aquatic environs. *Heliyon*. 2019;5(11):e02711. DOI:10.1016/j.heliyon.2019.e02711
3. Peng X, Huang D, Odoom-Wubah T, Fu D, et al. Adsorption of anionic and cationic dyes on ferromagnetic ordered mesoporous carbon from aqueous solution: equilibrium, thermodynamic and kinetics. *Journal of Colloid and Interface Science*. 2014;430:272-282. DOI: 10.1016/j.jcis.2014.05.035

4. Eltaweil AS, Ali Mohamed H, Abd El-Monaem EM, El-Subruiti GM. Mesoporous magnetic biochar composite for enhanced adsorption of malachite green dye: characterization, adsorption kinetics, thermodynamics and isotherms. *Advanced Powder Technology*. 2020;31(3): 1253-1263. DOI:10.1016/j.apt.2020.01.005
5. Wang X, Xu Q, Zhang L, Pei L, et al. Adsorption of methylene blue and congo red from aqueous solution on 3d mxene/carbon foam hybrid aerogels: a study by experimental and statistical physics modeling. *Journal of Environmental Chemical Engineering*. 2023;11(1):109206. DOI:10.1016/j.jece.2022.109206
6. Ohemeng-Boahen G, Sewu DD, Tran HN, Woo SH. Enhanced adsorption of congo red from aqueous solution using chitosan/hematite nanocomposite hydrogel capsule fabricated via anionic surfactant gelation. *Colloids and Surfaces A: Physicochemical and Engineering Aspects*. 2021;625:126911. DOI:10.1016/j.colsurfa.2021.126911
7. Boretti A, Rosa L. Reassessing the projections of the world water development report. *Npj Clean Water*. 2019;2(1):15. DOI:10.1038/s41545-019-0039-9
8. Pichel N, Vivar M, Fuentes M. The problem of drinking water access: a review of disinfection technologies with an emphasis on solar treatment methods. *Chemosphere*. 2019;218:1014-1030. DOI:10.1016/j.chemosphere.2018.11.205
9. Sabzehmeidani MM, Mahnaee S, Ghaedi M, Heidari H, et al. Carbon based materials: a review of adsorbents for inorganic and organic compounds. *Materials Advances*. 2021;2(2):598-627. DOI:10.1039/D0MA00087F
10. Khan TA, Saud AS, Jamari SS, Rahim MHA, et al. Hydrothermal carbonization of lignocellulosic biomass for carbon rich material preparation: a review. *Biomass and Bioenergy*. 2019;130:105384. DOI:10.1016/j.biombioe.2019.105384
11. Dada AO, Inyinbor AA, Tokula BE, Bayode AA, et al. Zinc oxide decorated plantain peel activated carbon for adsorption of cationic malachite green dye: mechanistic, kinetics and thermodynamics modeling. *Environmental Research*. 2024;252:119046. DOI:10.1016/j.envres.2024.119046
12. Liu Y, Wei S, Kamali BE, Ege D, et al. Ni_{0.4}Fe_{2.6}O₄/(Fe, Ni)-carbon core-shell magnetic mesoporous nanostructure for efficient adsorption and photocatalytic degradation of malachite green from wastewater. *Journal of Water Process Engineering*. 2024;59:105019. DOI:10.1016/j.jwpe.2024.105019
13. Das T, Debnath A, Manna MS. Adsorption of malachite green by aegle marmelos-derived activated biochar: novelty assessment through phytotoxicity tests and economic analysis. *Journal of the Indian Chemical Society*. 2024;101(9):101219. DOI:10.1016/j.jics.2024.101219
14. Chen L, Mi B, He J, Li Y, et al. Functionalized biochars with highly-efficient malachite green adsorption property produced from banana peels via microwave-assisted pyrolysis. *Bioresource Technology*. 2023;376: 128840. DOI:10.1016/j.biortech.2023.128840
15. Altun T, Ecevit H. Adsorption of malachite green and methyl violet 2b by halloysite nanotube: batch adsorption experiments and box-behnken experimental design. *Materials Chemistry and Physics*. 2022;291: 126612. DOI:10.1016/j.matchemphys.2022.126612
16. Sirach R, Dave PN. β -cyclodextrin polymer/zinc ferrite nanocomposite: synthesis, characterization, and adsorption application for the removal of malachite green and Congo red. *Journal of Hazardous Materials Advances*. 2023;10:100300. DOI:10.1016/j.hazadv.2023.100300
17. Leudjo Taka A, Fosso-Kankeu E, Pillay K, Yangkou Mbianda X. Metal nanoparticles decorated phosphorylated carbon nanotube/cyclodextrin nanosponge for trichloroethylene and Congo red dye adsorption from wastewater. *Journal of Environmental Chemical Engineering*. 2020;8(3):103602. DOI:10.1016/j.jece.2019.103602
18. Gopalakrishnan S, Kannan P, Balasubramani K, Rajamohan N, et al. Sustainable remediation of toxic Congo red dye pollution using bio based carbon nanocomposite: modelling and performance evaluation. *Chemosphere*. 2023;343:140206. DOI: 10.1016/j.chemosphere.2023.140206
19. Abegunde SM, Olasehinde EF, Adebayo MA. Green synthesis of ZnO nanoparticles using nauclea latifolia fruit extract for adsorption of Congo red. *Hybrid Advances*. 2024;5:100164. DOI: 10.1016/j.hybadv.2024.100164
20. Rao R, Huang Y, Zhang H, Hu C, et al. A simple melamine-assisted cellulose pyrolysis synthesis of magnetic and mesoporous n-doped carbon composites with excellent adsorption of Congo red. *Separation and Purification Technology*. 2024;347:127678. DOI:10.1016/j.seppur.2024.127678
21. Li N, Yan X, Dai W, Lv B, et al. Adsorption properties and mechanism of sepiolite to graphene oxide in aqueous solution. *Arabian Journal of Chemistry*. 2023;16(4):104595. DOI:10.1016/j.arabjc.2023.104595
22. Ali I, Burakov AE, Burakova IV, Kuznetsova TS, et al. Facile and economic preparation of graphene hydrothermal nanocomposite from sunflower waste: kinetics, isotherms and thermodynamics for Cd(II) and Pb(II) removal from water. *Journal of Molecular Liquids*. 2024;407:125179. DOI:10.1016/j.molliq.2024.125179
23. Adel M, El-Maghraby A, El-Shazly O, El-Wahidy EWF, Mohamed MAA. Synthesis of few-layer graphene-like nanosheets from glucose: New facile approach for graphene-like nanosheets large-scale production. *Journal of Materials Research*. 2016;31:455-467. DOI:10.1557/jmr.2016.25
24. Ni Z, Wang Y, Yu T, Shen Z. Raman spectroscopy and imaging of graphene. *Nano Research*. 2008;1(4):273-291. DOI: 10.1007/s12274-008-8036-1
25. Qiu H, Lv L, Pan B, Zhang Q, et al. Critical review in adsorption kinetic models. *Journal of Zhejiang University-SCIENCE A*. 2009;10(5):716-724. DOI:10.1631/jzus.A0820524
26. Naghizadeh A, Ghasemi F, Derakhshani E, Shahabi H. Thermodynamic, kinetic and isotherm studies of sulfate removal from aqueous solutions by graphene and

graphite nanoparticles. *Desalination and Water Treatment*. 2017;80:247-254. DOI:10.5004/dwt.2017.20891

27. Vigdorowitsch M, Pchelintsev A, Tsygankova L, Tanygina E. Freundlich isotherm: an adsorption model complete framework. *Applied Sciences*. 2021;11(17):8078. DOI:10.3390/app11178078

28. Kadum AHK, Burakova IV, Mkrtchyan ES, Ananyeva OA, et al. Sorption kinetics of organic dyes methylene blue and malachite green on highly porous

carbon material. *Journal of Advanced Materials and Technologies*. 2023;8(2):130-140. DOI:10.17277/jamt.2023.02.pp.130-140

29. Hameed BH, Tan IAW, Ahmad AL. Adsorption isotherm, kinetic modeling and mechanism of 2,4,6-trichlorophenol on coconut husk-based activated carbon. *Chemical Engineering Journal*. 2008;144(2):235244. DOI: 10.1016/j.cej.2008.01.028

Information about the authors / Информация об авторах

Alexey N. Timirgaliev, Master's Degree Student, Tambov State Technical University (TSTU), Tambov, Russian Federation; ORCID 0009-0006-5030-3677; e-mail: timirgaliev31@mail.ru

Irina V. Burakova, Cand. Sc. (Eng.), Associate Professor, TSTU, Tambov, Russian Federation; ORCID 0000-0003-0850-9365; e-mail: iris_tamb68@mail.ru

Sofya O. Rybakova, Student, TSTU, Tambov, Russian Federation; e-mail: sofarybackova@yandex.ru

Oksana A. Ananyeva, Postgraduate, TSTU, Tambov, Russian Federation; ORCID 0000-0002-1188-9402; e-mail: oksana.a9993471@gmail.com

Vladimir O. Yarkin, Master's Degree Student, TSTU, Tambov, Russian Federation; ORCID 0009-0001-2185-0149; e-mail: sttstu90@gmail.com

Tatyana S. Kuznetsova, Cand. Sc. (Eng.), Senior Lecturer, TSTU, Tambov, Russian Federation; ORCID 0000-0001-6508-2092; e-mail: kuznetsova-t-s@yandex.ru

Ali H. K. Kadum, Postgraduate, TSTU, Tambov, Russian Federation; e-mail: ali_strong_2010@yahoo.com

Alexander E. Burakov, Cand. Sc. (Eng.), Associate Professor, TSTU, Tambov, Russian Federation; ORCID 0000-0003-4871-3504; e-mail: m-alex1983@yandex.ru

Тимиргалиев Алексей Николаевич, магистрант, Тамбовский государственный технический университет (ТГТУ), Тамбов, Российская Федерация; ORCID 0009-0006-5030-3677; e-mail: timirgaliev31@mail.ru

Буракова Ирина Владимировна, кандидат технических наук, доцент, ТГТУ, Тамбов, Российская Федерация; ORCID 0000-0003-0850-9365; e-mail: iris_tamb68@mail.ru

Рыбакова Софья Олеговна, студент, ТГТУ, Тамбов, Российская Федерация; e-mail: sofarybackova@yandex.ru

Ананьева Оксана Альбертовна, аспирант, ТГТУ, Тамбов, Российская Федерация; ORCID 0000-0002-1188-9402; e-mail: oksana.a9993471@gmail.com

Яркин Владимир Олегович, магистрант, ТГТУ, Тамбов, Российская Федерация; ORCID 0009-0001-2185-0149; e-mail: sttstu90@gmail.com

Кузнецова Татьяна Сергеевна, кандидат технических наук, старший преподаватель, ТГТУ, Тамбов, Российская Федерация; ORCID 0000-0001-6508-2092; e-mail: kuznetsova-t-s@yandex.ru

Кадум Али Хуссейн Кадум, аспирант, ТГТУ, Тамбов, Российская Федерация; e-mail: ali_strong_2010@yahoo.com

Бураков Александр Евгеньевич, кандидат технических наук, доцент, ТГТУ, Тамбов, Российская Федерация; ORCID 0000-0003-4871-3504; e-mail: m-alex1983@yandex.ru

Received 19 June 2024; Accepted 26 July 2024; Published 22 October 2024



Copyright: © Timirgaliev AN, Burakova IV, Rybakova SO, Ananyeva OA, Yarkin VO, Kuznetsova TS, Kadum AHK, Burakov AE, 2024. This article is an open access article distributed under the terms and conditions of the Creative Commons Attribution (CC BY) license (<https://creativecommons.org/licenses/by/4.0/>).

Production of carbon membranes from porous polyacrylonitrile hollow fibers via IR pyrolysis

© Ala L. Yaskевич^a, Tatsiana A. Hliavitskaya^a✉, Alexey A. Yushkin^b,
Svetlana A. Pratsenko^a, Evgenii A. Nazarov^a, Mikhail N. Efimov^b,
Dmitry G. Muratov^b, Tatiana V. Plisko^a, Alexandr V. Bilydukevich^a

^a Institute of Physical Organic Chemistry, National Academy of Sciences of Belarus,
13, Surganov St., Minsk, 220072, Belarus,

^b A.V. Topchiev Institute of Petrochemical Synthesis, Russian Academy of Sciences,
29, Leninsky Av., Moscow, 119991, Russian Federation

✉ thliavitskaya@gmail.com

Abstract: A new approach to carbon membranes fabrication by IR pyrolysis of the hollow fiber (HF) porous membranes from a homopolymer (PAN) and acrylonitrile copolymers with methyl acrylate (PAN-MA) and itaconic acid (PAN-IA) was developed. The method includes thermal stabilization of membranes at 250 °C, and subsequent IR pyrolysis. It was established that the HF membranes made from PAN-IA and PAN were the least susceptible to destruction with increasing temperature. However, for samples based on PAN-MA, the significant deformation of hollow fiber membranes after IR pyrolysis occurs at temperatures above 200–300 °C. Scanning electron microscopy study showed that the presence of glycerol as an impregnating agent in membranes (regardless of the chemical composition of acrylonitrile copolymers) leads to a less regular and more defective structure of the resulting carbon membranes. It was found that the thermal stabilization at 250 °C preserves structural integrity and contributes to the production of mechanically stable carbon membranes. FTIR spectra confirmed that IR radiation catalyzes transformations in the polymer structure. As a result, the time of thermal stabilization and pyrolysis was noticeably reduced. It was shown, that 15 min pretreatment and 5 min pyrolysis is enough for effective stabilization of membrane structure.

Keywords: carbon membrane; homopolymer (PAN); pyrolysis; hollow fiber; copolymer; IR treatment.

For citation: Yaskевич AL, Hliavitskaya TA, Yushkin AA, Pratsenko SA, Nazarov EA, Efimov MN, Muratov DG, Plisko TV, Bilydukevich AV. Production of carbon membranes from porous polyacrylonitrile hollow fibers via IR pyrolysis. *Journal of Advanced Materials and Technologies*. 2024;9(3):188-206. DOI: 10.17277/jamt.2024.03.pp.188-206

Получение углеродных мембран из полиакрилонитрильных полых волокон методом ИК-пиролиза

© А. Л. Яскевич^a, Т. А. Глевицкая^a✉, А. А. Юшкин^b,
С. А. Праценко^a, Е. А. Назаров^a, М. Н. Ефимов^b,
Д. Г. Муратов^b, Т. В. Плиско^a, А. В. Бильдюкевич^a

^a Институт физико-органической химии Национальной академии наук Беларуси,
ул. Сурганова, 13, Минск, 220072, Республика Беларусь,

^b Институт нефтехимического синтеза им. А. В. Топчиева РАН,
Ленинский пр., 29, Москва, 119991, Российская Федерация

✉ thliavitskaya@gmail.com

Аннотация: Предложен новый подход к получению углеродных мембран при помощи ИК-пиролиза полволоконных мембран из полиакрилонитрила (ПАН) и сополимеров акрилонитрила с метилакрилатом (ПАН-МА) и итаконовой кислотой (ПАН-ИА). Предложенный способ включает термостабилизацию мембран при 250 °C и последующий ИК-пиролиз. Установлено, что полволоконные мембраны, изготовленные из ПАН-ИА

и ПАН, наименее подвержены разрушению при повышении температуры. Для образцов на основе ПАН-МА деформация половолоконных мембран в результате ИК-пиролиза регистрируется при температурах выше 200...300 °С. Исследование структуры углеродных мембран методом растровой электронной микроскопии выявило, что использование глицерина в качестве импрегнирующего агента (независимо от химического состава сополимеров акрилонитрила) приводит к менее регулярной и более дефектной структуре получаемых углеродных мембран. Установлено, что термостабилизация при 250 °С сохраняет структурную целостность и способствует получению механически стабильных углеродных мембран. Методом ИК-спектроскопии доказано, что ИК-излучение способствует существенному преобразованию структуры полимера. Показано, что 15-минутной предварительной обработки и пятиминутного пиролиза достаточно для эффективной стабилизации структуры мембраны.

Ключевые слова: углеродная мембрана; полиакрилонитрил (ПАН); пиролиз; полые волокна; сополимер; ИК-обработка.

Для цитирования: Yaskevich AL, Hliavitskaya TA, Yushkin AA, Pratsenko SA, Nazarov EA, Efimov MN, Muratov DG, Plisko TV, Bilydukevich AV. Production of carbon membranes from porous polyacrylonitrile hollow fibers via IR pyrolysis. *Journal of Advanced Materials and Technologies*. 2024;9(3):188-206. DOI: 10.17277/jamt.2024.03.pp.188-206

1. Introduction

Carbon membranes are chemical stable materials that are resistant to pressure and temperature. They are superior to traditional polymer membranes for various practical applications in gas separation, pervaporation, vapor permeation, and liquid filtration. For example, carbon membranes were used as porous cathodes for lithium batteries [1]. Carbon membranes can also act as adsorbents [2]. Due to the extremely high inner surface area (more than $1000 \text{ m}^2 \cdot \text{g}^{-1}$), such membranes can selectively absorb dissolved substances with a size of about 1 nm. The high chemical stability of carbon membranes allows for their regeneration using acidic solutions. Carbon membranes have some advantages over traditional polymer membranes for gas and vapor separation [3, 4]. Such materials are especially useful for separating olefin/paraffin mixtures or for separating natural gas (the difference in molecular diameters is at the level of 0.5 Å) [4, 5]. Carbon membranes can also be used to isolate hydrogen [6, 7] or carbon dioxide [8] from gas mixtures. Carbon membranes are also suitable for separating liquid solutions [2] and for effective separation of water–oil emulsions [9, 10]. Thus the oil rejection efficiency being over 98 % [10].

Currently, the basis for obtaining carbon membranes are polyimides [3, 4, 11], polyacrylonitrile (PAN) [2, 12, 13], phenolic resins [6, 14], polyfurfuryl alcohol [7], polyvinylidene chloride-acrylate [5], cellulose [15] and others [16, 17]. Several patents focus on the synthesis of carbon membranes [18–20]. Carbon membranes are typically produced in flat sheet or tubular membrane shapes. To obtain defect-free membranes with high mechanical strength, a dense layer of polymer was deposited on a macroporous support as a base for carbon membrane [21, 22]. During the carbonization

process, the thickness of the selective layer decreased. If ceramic support was used for membrane preparation, cracking and formation of defects could occur in selective layers. Consequently, several layers were required to be deposited to eliminate all defects and obtain a defect-free membrane [23]. Flat sheet membranes can be used in plate-and-frame membrane modules, providing the membrane packing density of $300\text{--}1000 \text{ m}^2 \cdot \text{m}^{-3}$. In contrast, self-supporting membranes (tubular, capillary, hollow fiber) can significantly increase the efficiency of separation processes due to the high packing density of membranes in the module. For instance, hollow fiber membranes packing density can reach up to $30,000 \text{ m}^2 \cdot \text{m}^{-3}$ depending on the fiber diameter [22]. On the other hand, this might present challenges in providing the required mechanical strength.

At the same time, there are few reviews devoted to the production of hollow fiber carbon membranes [24–26]. Most reviews on the production of carbon fibers highlight PAN as the most common base material [27–30]. One of the reasons for this is the high degree of molecule orientation [13], due to which the pyrolysis of PAN hollow fiber membranes results in the formation of a thermally stable, highly oriented molecular structure. It provides a high mechanical strength of the resulting material. This minimizes the problem of the low mechanical strength of self-supporting carbon material. At the same time, there are also studies on the production of carbon membranes from PAN [23, 31–33]. The study of heat treatment of PAN hollow fiber membranes at 500–800 °C showed a significant effect of temperature on the pore size of the obtained carbon membrane [23]. In [31, 32] PAN-membrane modification method via heating with infrared (IR) radiation was developed. It was noted that the mechanism for forming conjugated structures in

polyacrylonitrile under the IR radiation was similar to that of the thermal transformations [34]. In this case, the structural transformations of polyacrylonitrile under IR radiation occur faster compared to traditional methods of thermal treatment [34, 35]. The IR treatment reduces the time required for insoluble structure formation without using unsafe chemicals as cross-linking agents [33, 36]. The use of IR radiation not only reduces the treatment time to several minutes, but also decreases the temperature by 50–100 °C [33]. Fabrication of PAN-membranes resistant to aprotic solvents by IR treatment consumes 6.5 times less energy compare to convective heating in a laboratory oven [36]. Carbon membranes fabricated by IR irradiation treatment exhibited more than 100 times higher productivity, with processing time and energy requirements reduced by ~20 and ~11 times, respectively, compared to a conventional electric heating method [33]. Therefore, short processing time, low power consumption, and absence of hazardous chemicals as cross-linking agents make IR-treatment an effective method for producing carbon membranes. It should be noted that the studies referenced primarily utilize either specially synthesized PAN [31, 32] or PAN-homopolymer [33, 36] as a precursor for carbon membrane production. While PAN-homopolymer is commonly used as a hollow fiber membrane-forming polymer, it is not the only commercially available polymer which is used for hollow fiber PAN-membranes production [37]. The introduction of comonomers (such as acrylic acid, itaconic acid, methyl acrylate and etc.) can improve certain properties of acrylonitrile polymers, such as solubility, hydrophilicity, drawability, and fiber spinning stability of hollow fibers [38]. Notably, acid comonomers such as

itaconic acid are often introduced into the commercially available polymers to increase hydrophilicity; they can also reduce the cyclization temperature and improve the stabilization of the resulting carbon fiber [39, 40]. Consequently, using hollow fiber ultrafiltration membranes made from acrylonitrile copolymers as precursors for carbon membrane production is highly promising. That is why the objective of this research is to use IR pyrolysis on hollow fiber ultrafiltration membranes made from acrylonitrile polymers of various compositions to produce carbon membranes. We propose methods for producing carbon membranes by IR pyrolysis of hollow fiber ultrafiltration membranes from commercially available acrylonitrile polymers of various compositions (poly(acrylonitrile-co-methyl acrylate), poly(acrylonitrile-co-itaconic acid), PAN-homopolymer). In the process of forming membranes, it is possible to adjust the conditions for producing mechanically stable membranes. Further, during the IR pyrolysis, one can change the pore sizes in the selective layer. Using various acrylonitrile copolymers as membrane-forming polymers made it possible to study the effect of the chemical composition of acrylonitrile copolymers on the properties of the resulting carbon membranes.

2. Materials and Methods

2.1. Materials

A commercial homopolymer and two acrylonitrile copolymers were used as membrane-forming materials in this study (Table 1). Dimethylsulfoxide (DMSO, chemically pure, “Khimmed”) was used as a solvent for casting solution preparation.

Table 1. Polymers used in this study for hollow fiber membrane preparation

Sample	Polymer	Monomer unit ratio ¹ , %	M_w^1 , kg·mol ⁻¹	$\eta_{sp}^{1,2}$	Manufacturer
PAN	Polyacrylonitrile	> 99.5	200	1.64	Dolan, Germany
PAN-MA	Poly(acrylonitrile-co-methyl acrylate)	92:8	107	1.41	JSC “VNIISV”, Russia
PAN-IA	Poly(acrylonitrile-co-itaconic acid)	99:1	99	1.29	European Carbon Fibers (ECF, former EPG), Germany

¹ Data provided by the manufacturer.

² η_{sp} is the polymer specific viscosity.

2.2. Hollow fiber membrane preparation

Casting solutions were prepared by dissolving polymers—in DMSO, using a laboratory setup that included a thermostated stainless steel reactor and an overhead stirrer (IKARW 20 Digital, Germany). The temperature for preparation of the spinning solution was 100 °C, the preparation time was 4 hours, and the stirring speed was 800 rpm. The PAN concentration in the spinning solution was 16 wt. %.

The hollow fiber membranes were obtained by a non-solvent induced phase separation (NIPS) method using a dry-jet wet spinning process on a laboratory setup (Fig. 1). The equipment for hollow fiber membrane fabrication included a system of thermostatically controlled receiving-supply vessels and tubing for a spinning dope (1, Fig. 1) and an internal coagulant (2, Fig. 1), a stand with a spinneret assembly (3, Fig. 1), and a receiving tank with tap water at $T = 15\text{ °C}$ (4, Fig. 1). The dope and the internal coagulant (water) are fed into the spinneret by compressed air, the pressure of which is controlled by pressures gauges (5, Fig. 1). The hollow fiber membranes are formed by gravity without winder in the system by the free-fall spinning method [41–43].



Fig. 1. Setup for the hollow fiber membrane fabrication: (1) spinning dope vessel; (2) internal coagulant bath; (3) spinneret; (4) receiving bath; (5) pressure gauges; (6) bore fluid temperature sensor and (7) thermostat

The hollow fibers were fabricated using various conditions: the polymer solution pressure was 200–250 kPa, the coagulant pressure was 30 kPa, the bore fluid temperature was 30 °C, and the temperature of the receiving (external coagulation) bath was 15 °C, the temperature of the polymer solutions was 40–50 °C, the air humidity was 55 %. The air gap distance was 80 cm. The outer diameter of the spinneret was 1.8 mm, the inner diameter was 0.8 mm. The spinning modes for forming PAN hollow fiber membranes were selected in accordance with the rheological behavior and properties of the polymer solution, which are given in [38].

The produced membranes were soaked in distilled water rinse bath for 12 hours to remove residual solvents and to complete the phase separation. Then, one part of the hollow fiber membranes was immersed in a 30 % glycerol aqueous solution for 24 hours and then dried for 48 hours. The other part of the membranes was dried without treatment with a glycerol solution.

2.3. Permeability of the prepared hollow fiber membranes

The permeability of individual fibers was measured on a cross-flow setup that included a gear pump (type DGS.68PPT, Tuthill Corp.) and a flow-through cell consisting of inlet and outlet capillaries and a fiber sample strung on them. Pure water flux was measured at a transmembrane pressure of 1 bar for at least 1 hour to obtain a steady-state value. The pure water flux of the membranes (J , $\text{L}\cdot\text{m}^{-2}\cdot\text{h}$) was calculated according to the equation:

$$J = \frac{V}{t \pi D_{\text{inn}} l}, \quad (1)$$

where V is the volume of the filtrate, L; D_{inn} is the inner diameter of the fiber, m; l is the fiber length, m; t is the filtration time, h.

Blue Dextran dye with a molecular weight of $70\text{ kg}\cdot\text{mol}^{-1}$ was used for rejection tests. A new membrane sample was used for every rejection experiment. Before the rejection test, distilled water was filtered through a membrane for 1 hour at 1 bar. The separation test was carried out at the transmembrane pressure of 1 bar for at least 1 hour to achieve steady-state values of the rejection. All experiments were prepared with a solute concentration of $100\text{ mg}\cdot\text{L}^{-1}$. The concentration of solute in the feed and permeate was measured with a spectrophotometer at the wavelength of 620 nm. The rejection R is calculated using the relation:

$$R = \left(1 - \frac{C_p}{C_f} \right) \cdot 100\%, \quad (2)$$

where C_f and C_p denote the solute concentrations in the feed and permeate respectively.

2.4. Geometric parameters and structure of the prepared membranes

The geometric dimensions of the structures of the prepared membranes were investigated by scanning electron microscopy (SEM). Two SEM microscopes were used for this purpose: Phenom Pro scanning electron microscope (Thermo Fisher Scientific, USA) with vacuum sputter coater DSR (Vacoat, London, UK) and Phenom XL G2 Desktop SEM (Thermo Fisher Scientific, USA) with Cressington 108 auto Sputter Coater (Great Britain) table magnetron sputtering machine. Membrane transverse cleavages were obtained after preliminary membranes impregnation in isopropanol and their subsequent breaking in liquid nitrogen. A thin (5–10 nm) layer of gold was deposited on the prepared samples.

2.5. Fourier-transform infrared (FTIR) analysis

The FTIR (Nicolet Is50 spectrometer, Thermo Fisher Scientific, USA) spectra of the prepared membranes were used to investigate the chemical composition of membranes. Before measurements, the membranes were rinsed several times with distilled water and then dried for about 48 hours at room temperature.

2.6. Determination of the membranes pore size

The porosity of the membranes was determined using the POROLIQ 1000 mL instrument (POROMETER, Belgium). Membrane pore size analysis was performed by liquid-liquid displacement method [44], using water-saturated isobutanol and isobutanol-saturated water as wetting and displacement liquids, respectively. Samples of hollow fiber membranes were glued with epoxy resin into a special holder designed in such a way that both ends of the hollow fiber remained open. Three segments cut from different parts of the hollow fiber were glued into the holder. The length of the working section through which the filtration was carried out was 1 cm for each fiber. After the epoxy resin hardened, the holder with glued fibers was placed in isobutanol for 12 hours. Then the sample was placed in a measuring setup filled with a displacing liquid (aqueous phase). The excess isobutanol was removed from the sample

surface due to its lower density compared to water and was subsequently removed from the setup during the measurement without affecting the process. When the holder with the membrane was placed in the setup, the transmembrane pressure increased step by step. At each pressure step, the measurement was carried out until the flow stabilized at the same level with an accuracy of $\pm 1 \mu\text{L}\cdot\text{min}^{-1}$ for 180 s. The pressure was increased step by step with a step of 0.2–0.5 bar until the moment of sample breaking, which was fixed by a sharp (by 4 orders of magnitude) increase in the flow through the membrane. When the flow sensor detected such an increase in flow, the measurement automatically stopped.

The pore diameter (d_p) corresponding to a given transmembrane pressure was calculated using the Young-Laplace equation:

$$d_p = \frac{4\gamma \cos \theta}{\Delta p}, \quad (3)$$

where γ is interfacial tension between two liquids used; θ is the contact angle between membrane and wetting liquid; Δp is transmembrane pressure.

In the used membranes, complete wetting with an alcohol-rich phase was observed, so the contact angle is 0, and $\cos \theta = 1$. The interfacial tension between the isobutanol and aqueous phases was $2.0 \text{ mN}\cdot\text{m}^{-1}$ at 20°C . The main value determined for each sample was the mean flow pore size (MFP), which was determined at a pressure at which the membrane permeability was 50 % of the maximum. This value differs from the number averaged pore size upwards because it takes into account that larger pores contribute more to the overall membrane permeability.

2.7. IR-pyrolysis of hollow fibers

A laboratory IR heating furnace [33] was used for thermal stabilization and pyrolysis of hollow fiber membranes (Fig. 2). Gas line was plugged into a quartz tube with the sample and an external control unit was connected to the apparatus. If experiments were performed under a nitrogen atmosphere, the quartz tube was closed in such a way that a small hole remained at one end of the tube, and constant nitrogen flow was supplied to the tube from the opposite side. In the experiments carried out on air, the quartz tube was open from one side and the gas line was closed. The tube was surrounded by an insulating box containing IR sources. KG-220

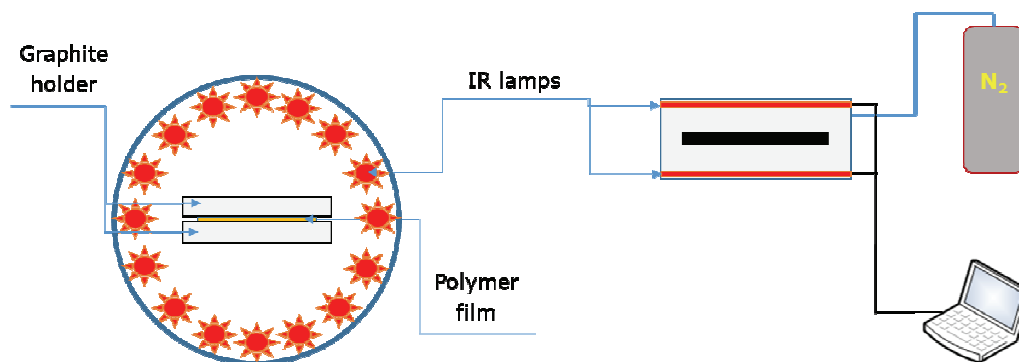


Fig. 2. Schematic illustrations of the IR furnace for membrane thermal treatment

halogen lamps with a radiation maximum in the region of 0.9–1.2 μm were used as a source of incoherent IR radiation. 3 to 6 fibers were placed in a graphite cassette for processing. During stabilization and further pyrolysis sample was freestanding without any tension. Additional quartz rods were laid between membrane samples to ensure the spatial separation of the samples without interfering with their uniform heating. The heating rate to the set temperature was $60\text{ }^\circ\text{C}\cdot\text{min}^{-1}$. The heating rate to a given temperature varied from 5 to $60\text{ }^\circ\text{C}\cdot\text{min}^{-1}$. The intensity of IR radiation was controlled by the heating temperature of the sample, measured using a chromel-alumel thermocouple placed directly under the sample. The control unit provided an increase and decrease in the intensity of IR radiation according to a given program. After reaching the predetermined temperature of the sample, the radiation intensity was reduced to ensure the constancy of the processing temperature for a predetermined time (1–15 minutes). Next, the IR lamps were turned off and the samples were cooled down under constant blowing with nitrogen or air.

A portion of the experiments was performed without thermal stabilization while the other part was carried out in two stages, with IR-pyrolysis preceded by thermal stabilization in air. At the end of the thermal stabilization stage, the IR lamps were turned off and the sample was allowed to slowly cool down to room temperature. Heating of the thermally stabilized samples for their pyrolysis started at room temperature.

2.8. Determination of the membrane shrinkage due to IR pyrolysis

Membrane shrinkage was calculated by the equation:

$$U = \left(1 - \frac{D_{\text{pyr}}}{D_{\text{ref}}} \right) \cdot 100\%, \quad (4)$$

where U is the degree of shrinkage of hollow fiber membranes, %; D_{ref} is the outer diameter of the reference hollow fiber membrane; D_{pyr} is the outer diameter of the hollow fiber membrane after IR-pyrolysis.

2.9. Determination of the membrane strength

The strength (σ_{str}) of the resulting hollow fiber membranes was studied using a TT-1100 tensile testing machine (Chemstruments, USA) at room temperature ($25\text{ }^\circ\text{C}$). The speed of movement of the traverse was 3.8 cm/min . The samples were hollow fibers about 70 mm long, fixed between clamps. The initial distance between the clamps was 30 mm .

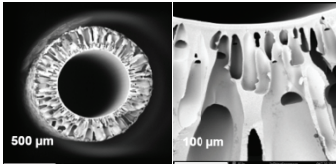
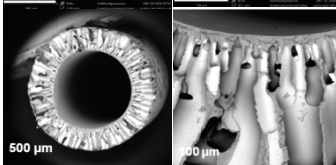
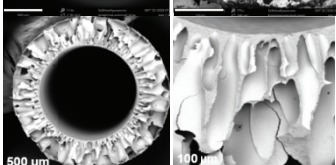
3. Results and Discussion

3.1. Properties of the reference hollow fiber membranes

The study of flat sheet ultrafiltration membranes formation from various acrylonitrile copolymers showed [38] that membranes prepared from acrylonitrile homopolymer solutions in DMSO with a concentration of 15% and higher have sponge-like structures of the membrane matrix.

In this paper, hollow fiber membranes were fabricated from acrylonitrile-based polymers as precursors for carbon membranes. 16% polymer solutions in DMSO were used for membrane preparation (Table 2). The strength of hollow fiber membranes (σ_{str}) depends on the polymer composition and drying conditions. Thus, for PAN and PAN-IA samples dried without glycerol (Sample II and Sample VI, respectively), the mechanical strength is higher than that for samples impregnated with glycerol aqueous solution before drying (Sample I and Sample V). For PAN-MA, a decrease in the mechanical strength was observed when hollow fiber membranes were dried without impregnation by glycerol (Sample IV).

Table 2. Characteristics of reference hollow fiber membranes

Sample	Polymer	Drying method	SEM	J_2 $L \cdot (\text{m}^2\text{h})^{-1}$	D_{ref}^1 , μm	D_{int}^2 , μm	L^3 , μm	σ_{str} , MPa
I	PAN	Glycerol		245 ± 5	1715 ± 30	1070 ± 10	320 ± 20	3.2
II	PAN	Without glycerol		185 ± 5	1750 ± 30	1095 ± 10	330 ± 20	3.6
III	PAN-MA	Glycerol		295 ± 5	1730 ± 30	1095 ± 10	310 ± 20	3.3
IV	PAN-MA	Without glycerol		220 ± 5	1815 ± 30	1110 ± 10	330 ± 20	2.9
V	PAN-IA	Glycerol		260 ± 5	1720 ± 30	1080 ± 10	320 ± 20	3.1
VI	PAN-IA	Without glycerol		195 ± 5	1780 ± 30	1100 ± 10	330 ± 20	3.4

¹ D_{ref} is the outer diameter of the reference hollow fiber membrane.

² D_{int} is the fiber inner diameter.

³ L is the fiber wall thickness.

The geometric parameters of the hollow fiber membranes dried without glycerol differ from those impregnated with glycerol: the inner diameter and the wall thickness (L) of the fibers is 20–25 and 20 μm larger, respectively. At the same time, the water permeability of hollow fiber membranes dried without glycerol is lower by 20–25 %. Thus, drying without a plasticizer (glycerol) leads to the collapse of the pores of the selective layer. Moreover, the use of a plasticizer protects the pores during drying but increases the shrinkage of the hollow fiber matrix. The increase of shrinkage is due to the increase of the mobility of polymer chains plasticized with glycerol which facilitates their rearrangement while drying.

The hollow fiber ultrafiltration membranes were produced by the method of dry-jet wet spinning, in which non-solvent-induced phase separation (NIPS) occurs. The membranes have an asymmetric structure with a thin surface selective layer (pore sizes are tens of nanometers) and a large-pore drainage layer providing mechanical strength. The drainage layer is shot through with a large number of finger-shaped vacuoles (macrovoids). Macrovoids arise from a polymer-depleted phase during NIPS membrane fabrication. The growth of macrovoids begins when the rate of diffusion of the nonsolvent in the core of the polymer-depleted phase in a freshly formed polymer film is higher than the rate of diffusion of

the solvent through the core wall. As a result, a high osmotic pressure is created, acting through the core wall, which can deform and destroy the walls of the emerging macrovoids [41]. The structure of membranes from PAN solutions in DMSO does not practically undergoes deformation after drying without glycerol (see scanning electron microscopy (SEM) results) in contrast to the structure of PAN-MA membrane samples (Table 2). In the case of membrane samples from the PAN-IA copolymer, the formation of a finer porous structure is observed. On the other hand, the membranes from the PAN-MA copolymer were partially deformed after drying without glycerol.

3.2. Change in characteristics of hollow fiber membranes after IR pyrolysis

In this section, one-stage pyrolysis without thermal stabilization was used for carbon membrane preparation. The heating rate was $50\text{ }^{\circ}\text{C}\cdot\text{min}^{-1}$, and the pyrolysis time at the maximum processing temperature was 2 minutes. As studies of the prepared carbon membranes showed, shrinkage of hollow fibers occurs as a result of IR pyrolysis. The degree of shrinkage depends on the chemical nature of the membrane-forming polymer and drying conditions (with or without glycerol) (Fig. 3). Measurement of hollow fiber membranes dimensions after pyrolysis showed that in the temperature range from 200 to 500 $^{\circ}\text{C}$ there is a significant decrease in the linear dimensions (diameter, length) of the membranes, reaching 62 % (Fig. 3). Such significant decrease in linear dimensions (diameter, length) may be associated with shrinkage which stemmed from the evolving gases (as a result of membrane burn off) [45] With a further increase in temperature, almost no

changes in the dimensions of the samples were observed. All samples was brittle and not flexible but their strength was enough for further processing.

The comparison of different copolymers shows that the smallest shrinkage was observed in the case of PAN-IA membranes (40–50 %) (Fig. 3c). The membranes obtained from PAN slightly exceeded them in terms of shrinkage (45–52 %) (Fig. 3a), while the samples from PAN-MA lost more in size (52–62 %) (Fig. 3b). In addition, samples from PAN-IA were more resistant to cracking during the pyrolysis.

Differences were also observed in the structures of carbon membranes (Fig. 4). After IR pyrolysis of hollow fiber membranes dried without glycerol, the structure of the resulting carbon membranes was more regular and less defective, with a non-porous inner layer compared to hollow fiber membranes dries with glycerol. For carbon membranes made from PAN-MA (Samples III and IV), a more pronounced deformation of the membrane matrix was observed, which explains the results obtained on fiber shrinkage (Fig. 3b). The structures of carbon membranes obtained from PAN hollow fiber membranes impregnated with glycerol (Sample I) and those without glycerol (Sample II) differ slightly, although the shrinkage of the fibers after drying with glycerol was higher (Fig. 3a). For carbon membranes based on samples of hollow fiber membranes from PAN-MA and PAN-IA dried with glycerol, there are areas with an inhomogeneous structure and remnants of the porous structure of the membranes (Fig. 4, Sample III and Simple V, respectively). This may be due to several reasons: (1) during the IR pyrolysis some of the energy was wasted on glycerol evaporation; (2) plasticized polymer chains featured

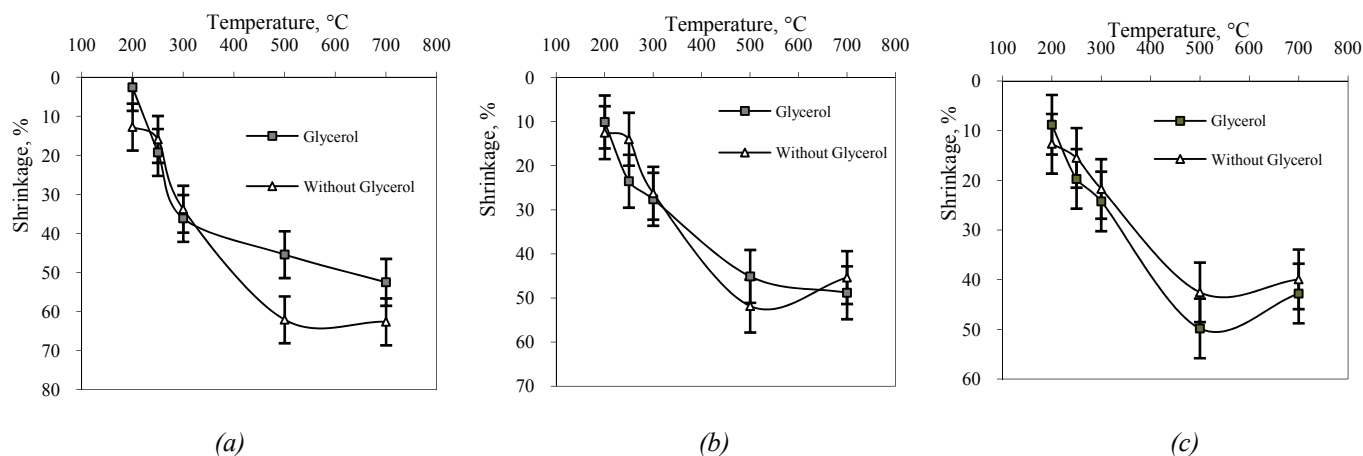


Fig. 3. Shrinkage of hollow fiber membranes depending on the IR pyrolysis temperature: a – PAN; b – PAN-MA; c – PAN-IA

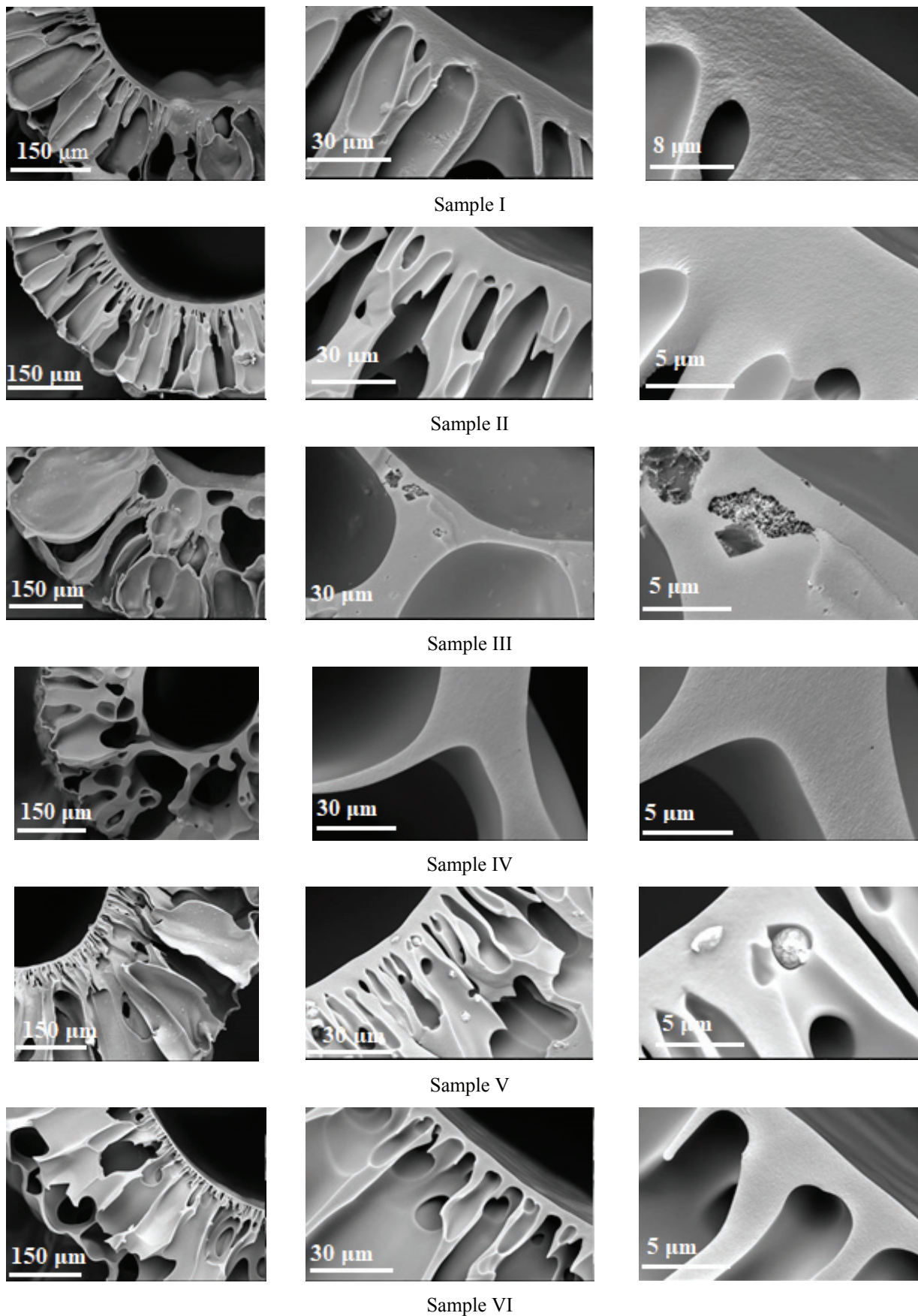


Fig. 4. SEM images of hollow fiber membranes after IR pyrolysis at 700 °C



Fig. 5. PAN hollow fiber membranes (Sample I) after pyrolysis in nitrogen atmosphere at different temperatures

increased mobility and can be rearranged during IR pyrolysis; (3) glycerol can impregnate membrane pore structure non-uniformly since membrane lumen is less accessible for glycerol penetration.

A study of the structure of membranes prepared at different temperatures showed that up to a temperature of 400 °C, no noticeable changes were observed in the structure of membrane cross-section. However, for membranes pyrolyzed at temperatures of 400 °C and higher, the structure of the membranes turned out to be significantly deformed (Fig. 4 and 5). It was found that the changes that occur during pyrolysis also depend on the material used and the drying method (with or without glycerol). The degree of deformation was bigger on the outer surface of the samples, while the inner layer as a whole remained unchanged. The observed deformations, most likely, resulted from the shrinkage of the samples during annealing.

A study of the mechanical strength of hollow fiber membranes after IR pyrolysis showed (Table 3) that at a treatment temperature of 200 °C, the strength of carbon membranes decreased by 20–24 % compared to the reference membranes (Table 2). With a further increase in temperature to 500 °C, the

strength of the membranes decreased by more than 50 %. An increase in temperature above 500 °C did not lead to a further decrease in strength. The comparison of samples initially dried without glycerol (IV) and dried after impregnation with glycerin solution (I and V) showed that the strength of hollow fibers after IR pyrolysis was practically independent of the drying method and polymer composition.

Table 3. Strength of membranes at different temperature IR pyrolysis in nitrogen atmosphere

IR-pyrolysis temperature, °C	σ_{str} , MPa		
	Sample I	Sample IV	Sample V
200	2.5	2.3	2.4
250	2.1	2.0	2.1
300	1.9	1.8	1.9
400	1.6	1.4	1.5
500	1.3	1.1	1.2
600	1.3	1.0	1.1
700	1.2	1.1	1.2

Table 4. Characteristics of hollow fiber membrane samples after IR pyrolysis in nitrogen atmosphere at different temperatures

Sample	Pore size, nm			Rupture pressure, bar			
	Initial	200 °C	250 °C	Initial	200 °C	250 °C	300 °C
I	27.5	~7.5	<5.8	6.0	>11	>14	10.1
II	11.7	9.9	3.8	7.0	8.3	23.1	14.2
III	38.1	7.9	4.1	6.9	>10.5	>20	16.4
IV	10.4	<7.2	<7.2	8.0	>11	>11	14.1
V	27.6	12.3	7.0	5.5	9.9	13.0	11.0
VI	13.6	~7.8	4.1	6.6	15.3	19.7	14.7

Porosimetric studies of membranes before and after IR pyrolysis showed that the main decrease in membrane pore size was observed in the pyrolysis temperature range of 200–300 °C (Table 4). For membrane samples impregnated with glycerol (I, III, V), the pore sizes were 2–3 times higher than the pore sizes of membranes dried without glycerol (II, IV, VI). After IR pyrolysis at 200 °C, the pore sizes of membrane samples I, III, and V decreased to 7.5–12 nm and were comparable with the pore sizes of membrane samples II, IV, and VI. After IR pyrolysis at 250 °C, the pore sizes of the samples decreased to 3.8–7.2 nm. For samples subjected to IR pyrolysis at a higher temperature, the pore size could not be determined due to the necessity of using high pressures that exceed the limiting pressure that the membranes were able to withstand.

A study of the tensile strength of the membrane samples showed (Table 4) that the rupture pressure of the hollow fibers increased after IR pyrolysis at 200 °C for all samples. With an increase in temperature to 250 °C, the rupture pressure of the samples also increased. However, with an increase in temperature up to 300 °C, the fiber rupture pressure for most samples decreased.

The obtained results indicate that during the IR pyrolysis of samples in a nitrogen atmosphere at temperatures of 200–300 °C, membrane shrinkage is accompanied by decrease in transport pore size in the selective layer of membranes. At the same time, at temperatures above 400 °C, although the main structure of the membrane remains unchanged, liquid porosimetry results indicate that most of the transport pores have already collapsed. Further sample shrinkage leads to deformation of the membrane macrostructure.

Testing of membranes from various PAN copolymers revealed that PAN-IA membranes experience less shrinkage during pyrolysis and are less susceptible to cracking, which makes this polymer optimal for carbon membrane preparation.

3.3. Influence of preliminary thermal stabilization on the membrane characteristics

As it was shown in Fig. 3, the geometric parameters of hollow fibers were changed with an increase in the temperature of IR pyrolysis. The study of the carbon membranes obtained with and without thermal stabilization using SEM showed that the samples subjected to IR pyrolysis after thermal stabilization demonstrated absence of structure deformations with an increase in the pyrolysis temperature (Table 5). In the absence of thermal stabilization, the structure of hollow fiber membranes after IR pyrolysis is significantly deformed. The destruction of the structure is especially noticeable for hollow fiber membranes impregnated with glycerol, apparently due to a more significant decrease in the pore size during pyrolysis.

The PAN-IA membranes were least susceptible to degradation with increasing temperature after IR treatment with thermal stabilization. Membranes dried without glycerol (Table 5, Sample VI), even at high temperatures of IR pyrolysis, preserved their geometrically regular structures. In contrast, glycerol-impregnated membranes (Table 5, Sample V) demonstrated a greater deformation of the structure after a one-stage IR pyrolysis. A similar trend was observed with the PAN samples (Table 5, Sample II). Similar to PAN-IA samples, PAN-membranes retained their structure after IR pyrolysis with thermal stabilization. However, without thermal stabilization membranes impregnated with glycerol experienced a significant deformation at a temperature of 500 °C and above (Table 5, Sample I). For PAN-MA-based samples (Table 5, Samples III and IV) structural changes after IR pyrolysis with thermal stabilization were comparable to those of PAN-IA and PAN samples. However, after IR pyrolysis without thermal stabilization, the deformation of hollow fiber membranes was notably significant at temperatures above 200–300 °C. Such significant deformation of

Table 5. SEM cross-section of membranes from PAN after IR-pyrolysis in various ways

Sample	Thermal stabilization (250 °C) and IR pyrolysis T , °C			IR pyrolysis T , °C		
I	300	500	700	300	500	700
II	300	500	700	300	600	700
III	300	500	700	200	500	700
IV	300	400	700	300	400	700
V	300	400	600	300	400	600
VI	300	500	700	300	500	700

glycerol impregnated membrane structure is likely due to an extreme reduction in the pore size resulting from the IR treatment. Impregnation of ultrafiltration membranes with glycerin solution is carried out to prevent pore contraction and is responsible for the high membrane flux [46]. This aligns well with the data presented in Table 4. Initial membranes impregnated with glycerol have pore sizes 2.0–3.6 times higher than those of initial membranes without glycerol. It is worth noting that other alcohols, such as isopropanol, ethanol, etc. can also be used as impregnating agents [47].

Using FTIR spectroscopy of prepared carbon membranes, a change in the chemical composition of samples after IR pyrolysis was investigated (Fig. 6). As the pyrolysis temperature increased from 200 to 400 °C, a decrease in the number of methylene groups (~ 2850 , 2930 , 1450 cm^{-1}) was observed. At temperatures of 400 °C and above the nitrile (~ 2250 cm^{-1}) and carbonyl (~ 1730 cm^{-1}) groups disappeared likely due to the initiation of the cyclization reaction [48]. At 400–500 °C a sharp peak was detected at 1590 cm^{-1} , representing a mix of C=N, C=C and C–N bonds [30]. This peak indicates the formation of cyclic structure of molecular chains, specifically through conversion of CN to C=N by cyclization [49]. The appearance of the C=C group was due to the dehydrogenation reaction [40]. The results of FTIR spectroscopy did not reveal significant differences in the resulting structures. The transformed peak shapes were nearly identical for all precursors. Carbonization of the samples apparently occurs at temperatures of 600–700 °C. At these temperatures FTIR spectra of membranes become flatter and the characteristic peaks rather diminish. The absence of these peaks indicates that PAN is completely converted to the cyclic carbon structure. Notably, compared to the FTIR spectrum of PAN-membranes, FTIR spectrum of the initial PAN-IA membrane had a characteristic band at 1710 cm^{-1} corresponding to C=O bond of itaconic acid. In the case of PAN-IA, cyclization and dehydrogenation were facilitated by itaconic acid through an ionic mechanism. Conversely, in the case of homopolymer, the cyclization of nitrile groups was initiated only through a free radical mechanism. The cyclization mechanisms were described in more detail in [30, 40].

In the FTIR spectra of carbon membranes based on hollow fibers dried without glycerol, a band ~ 1600 – 1590 cm^{-1} (C=N) appears after IR pyrolysis

at 300 °C (Fig. 6). A sharp disappearance of nitrile groups and a shift of the C=N bond band to 1570 cm^{-1} after pyrolysis at 400 °C was observed. At the same time, there were no significant differences in the spectra of the samples after IR pyrolysis with and without thermal stabilization. The spectra of samples obtained by IR pyrolysis with thermal stabilization were almost identical to the spectra of carbon membranes based on hollow fibers dried without glycerol. In the case of IR pyrolysis without thermal stabilization at 300–400 °C, a significant increase in the intensity of mix of C=N, C=C and C–N bonds at 1590 cm^{-1} was noted for PAN-MA and PAN-IA copolymers. This is due to the fact that the presence of a partially ionic structure eases the cyclization process [45].

3.4. Optimization of thermal stabilization conditions

The membranes subjected to thermal stabilization at a temperature of 200–240 °C for 15 minutes were more prone to deformation and cracking during pyrolysis (500 °C, 2 minutes) (Fig. 7). According to the FTIR spectra in Figs. 4 and 5, the pyrolysis at 500 °C has not finished the carbonization; therefore, higher temperature (600–700 °C) can be used during pyrolysis of the hollow fiber membranes. However, since the carbon membranes being developed are planned to be used for both gas separation and nanofiltration, it was decided to limit the pyrolysis temperature to 500 °C. This decision aligns with the data in [13], since at a very high temperature the pore size of membranes starts to decrease, ultimately leading to collapse.

Membranes, which underwent thermal stabilization at a temperature of 260–300 °C, retained its integrity. Further experiments in narrower temperature interval 240–260 °C showed that optimal temperature of thermal stabilization was 250 °C. At this temperature of thermal stabilization, the subsequent pyrolysis did not result in undesirable phenomena of cracking or deformation of the membranes. This suggests that heating of the sample under IR conditions follows similar mechanisms to traditional convective heating. Hence, thermal stabilization in an oxygen-containing atmosphere is important for maintaining membrane integrity during further pyrolysis at temperatures above 300 °C. At the same time, IR irradiation intensifies ongoing reactions, decreasing the time needed to achieve the desired conversion.

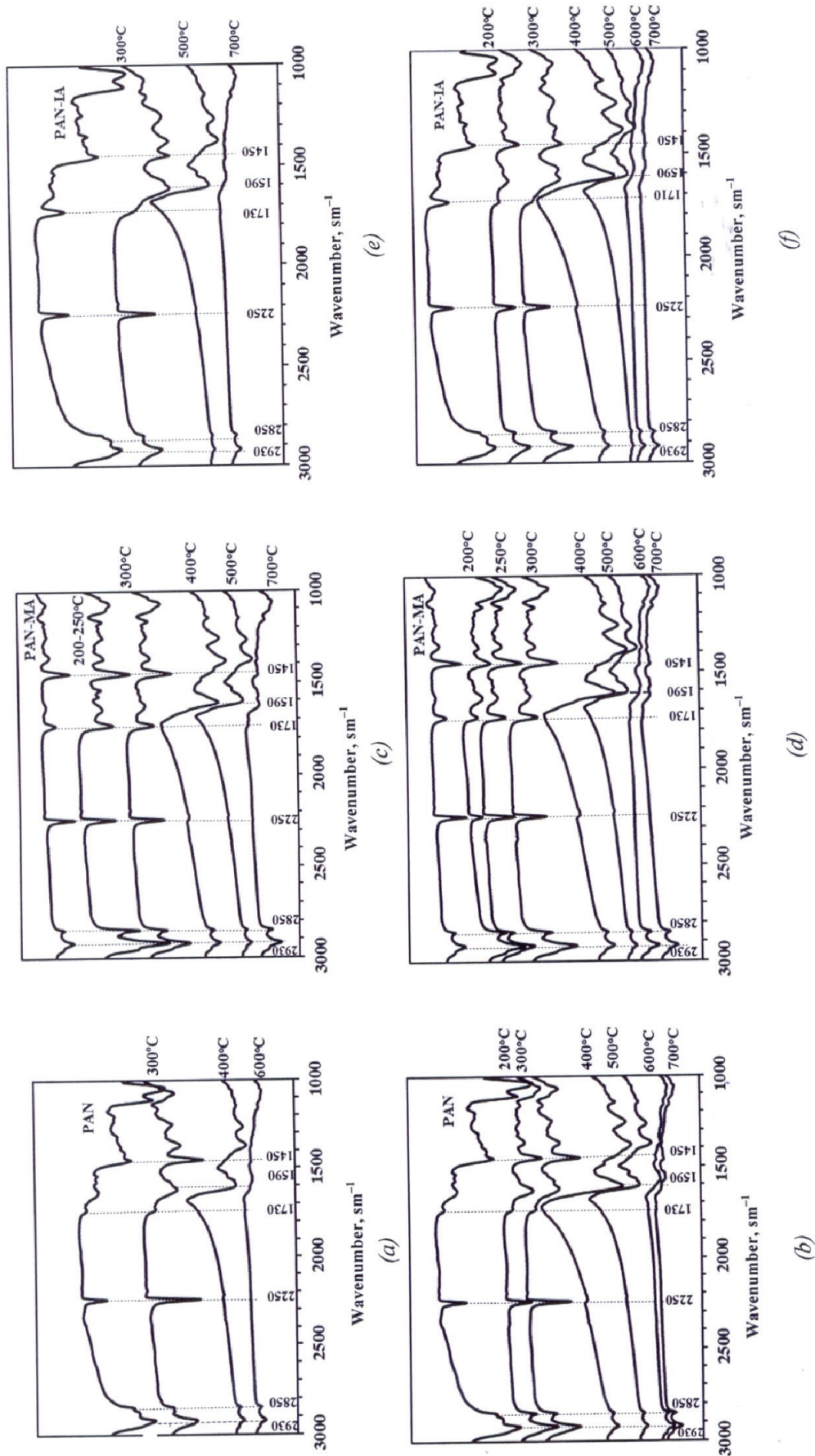


Fig. 6. FTIR of carbon membranes from Sample II (a, b), Sample IV (c, d) and Sample VI (e, f). Processing conditions: a, c, e – thermal stabilization at 250 °C and IR pyrolysis; b, d, f – IR pyrolysis

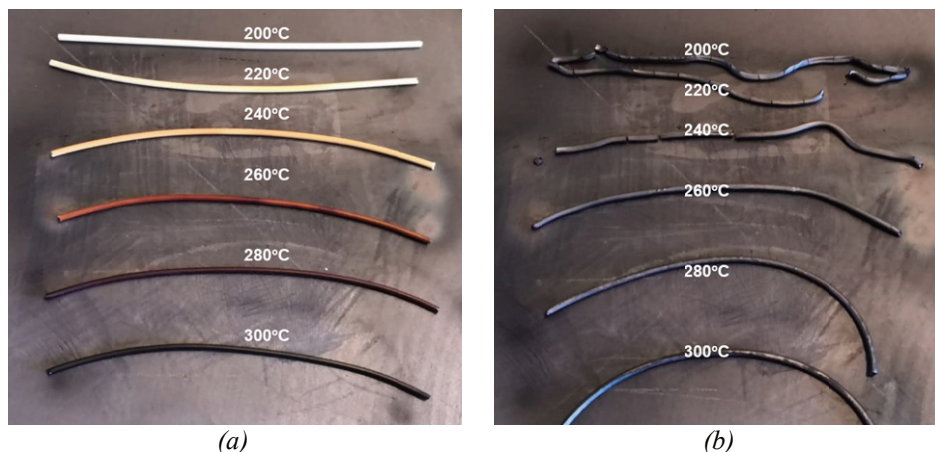


Fig. 7. Hollow fiber membranes after thermal stabilization (15 minutes) at various temperatures, before (a) and after (b) the pyrolysis stage at a temperature of 500 °C (2 minutes)

A similar behavior was observed when varying the thermal stabilization time. The membranes subjected to thermal stabilization (250 °C) for 5–10 minutes cracked during subsequent pyrolysis (500 °C, 2 minutes), while at a longer thermal stabilization time, the membranes retained their integrity. It is noteworthy that as the thermal stabilization time increased from 5 to 15 minutes, the color of membranes changed from pale beige to brown. With a further increase in the process time, no further changes in the membrane were observed. The thermal stabilization process required only 15 minutes, which is less than the time needed for thermal stabilization through convectional heating methods.

The obtained results also show that optimal thermal stabilization degree can be achieved at lower temperatures by increasing the treatment time.

The study investigated the influence of the heating rate of hollow fiber membranes by IR radiation during thermal stabilization and subsequent pyrolysis in the range of 5–60 °C·min⁻¹. The thermal stabilization parameters corresponded to the previously determined optimal values – 250 °C for 15 minutes, pyrolysis – 500 °C for 2 minutes. By varying the heating rate during thermal stabilization, it was found that at a low heating rate of 5 and 10 °C·min⁻¹, the samples retained their integrity during the subsequent pyrolysis; however, at higher heating rates, the pyrolysis of hollow fiber membranes led to their cracking. During pyrolysis, the heating rate was fixed at 60 °C·min⁻¹. The reason for this is that an increase in the heating rate leads to a decrease in the total processing time. This resulted in an insufficient level of sample stabilization before the pyrolysis stage. Thus, the value of 10 °C·min⁻¹ was chosen as the optimal heating rate, at which a

sufficient level of thermal stabilization of the membrane before IR pyrolysis is achieved.

The pyrolysis time at the maximum temperature ranged from 1 to 15 minutes. The membranes retained their integrity over the entire range of times. However, as the pyrolysis time exceeded 2 minutes, the strength of the membranes deteriorated. The drop of membrane strength was low, with a reduction not exceeding 10 % at maximum processing time.

The study of the influence of the heating rate during the pyrolysis process yielded similar findings: during the pyrolysis process, the membranes retained their integrity across all tested heating rates. All samples exhibited brittleness and poor flexibility after thermal stabilization and pyrolysis. No difference in membrane integrity was observed during the pyrolysis process with different heating rates, indicating that shorter processing time is preferable for the pyrolysis process. This contrasts with traditional convective heating, where lower heating rates are preferable to prevent membrane destruction. In IR processing reactions occur faster, making it possible to obtain membranes with shorter processing times. Hence, 60 °C·min⁻¹ and 2 minutes were chosen as the optimal heating rate and time for the pyrolysis stage.

3.5. Filtration performance of obtained membranes

Filtration performances were measured for membranes annealed at different IR treatment temperatures ranging from 200 to 500 °C. For membranes annealed at 200 and 250 °C, preliminary thermal stabilization was not applied. In contrast, for higher temperatures, thermal stabilization in air was applied for 15 minutes at a maximum temperature of 250 °C. The heating rate at

Table 6. Pure water flux and Blue Dextran rejection for hollow fiber membranes after different temperatures of IR treatment

IR treatment temperature, °C	Sample I		Sample IV		Sample V	
	$J, \text{L}\cdot(\text{m}^2\cdot\text{h})^{-1}$	$R, \%$	$J, \text{L}\cdot(\text{m}^2\cdot\text{h})^{-1}$	$R, \%$	$J, \text{L}\cdot(\text{m}^2\cdot\text{h})^{-1}$	$R, \%$
200	160	38	199	48	187	29
250	60	>99	68	95	62	68
300	18.7	>99	19.9	>99	19.0	99
400	10.5	>99	11.8	>99	11.5	>99
500	5.2	>99	6.7	>99	5.6	>99

thermal stabilization stage was 10 °C. After the thermal stabilization stage, the samples were subjected to pyrolysis in nitrogen atmosphere at a given temperature for 2 minutes. The heating rate in the pyrolysis process was 60 °C.

The pure water flux through membranes treated at a temperature of 200 °C was 10–15 % lower than that for the initial ones ($160\text{--}199 \text{ L}\cdot(\text{m}^2\cdot\text{h})^{-1}$ compared to $187\text{--}234 \text{ L}\cdot(\text{m}^2\cdot\text{h})^{-1}$) (Table 6). At a temperature of 300 °C, the flux dropped by an order of magnitude to $18.7\text{--}19.9 \text{ L}\cdot(\text{m}^2\cdot\text{h})^{-1}$. A further increase in temperature to 500 °C led to a decrease in pure water flux to $5.2\text{--}6.7 \text{ L}\cdot(\text{m}^2\cdot\text{h})^{-1}$. At the same time, the membranes retained more than 99 % of the Blue Dextran dye with a molecular weight of $70 \text{ kg}\cdot\text{mol}^{-1}$ (Table 6), which indicates that the obtained membranes were defect-free.

The decrease in pure water flux with an increasing IR treatment temperature was due to a decrease in pore size. Although the pore radius was not measured because of the high pressure needed for measuring such small pores, from filtration performances and shrinkage data (Fig. 3) it can be concluded that further decrease in pore size took place with increase of IR pyrolysis temperature. At the same time, complete collapse of the pores does not occur. From the other hand, high Blue Dextran rejection confirms absence of membrane cracking and appearance of defects during pyrolysis.

The obtained results demonstrated that IR irradiation can be used for preparation of carbon hollow fiber membranes. At the same time, by regulating the pyrolysis temperature it is possible to control the pore size of the obtained porous membranes.

4. Conclusion

A new technique for obtaining carbon membranes using IR radiation for heating the hollow fiber membranes has been developed. The optimal conditions for IR pyrolysis have been determined.

It was found that in the case of IR heating, samples of PAN hollow fiber membranes must be thermally stabilized in air at a maximum temperature of 250 °C for at least 15 minutes. Thermal stabilization is a necessary step in membrane processing, similar to convectional heating. It makes it possible to avoid undesirable effects of destruction and deformation of membranes during pyrolysis. Following the thermal stabilization stage, the samples are subjected to pyrolysis in an inert atmosphere. An optimal heating rate of $60 \text{ }^\circ\text{C}\cdot\text{min}^{-1}$ for duration of 2 minutes was chosen for the pyrolysis stage. The short processing time and high heating rate is preferable for pyrolysis process. This distinguishes IR heating from traditional convective heating. In the latter case, the lower heating rate is preferable to prevent membrane destruction. Faster processes associated with IR processing make it possible to obtain membranes with reduced processing time.

It has been established that IR pyrolysis of hollow fiber membranes prepared by spinning from 16 % solutions of PAN, PAN-MA, and PAN-IA in DMSO results in shrinkage of hollow fibers with the degree of shrinkage depending on the chemical nature of the membrane-forming polymer and drying conditions. The structure of the resulting carbon membranes was more regular and less defective if the porous membrane was not impregnated with glycerol. The PAN-MA samples were more prone to shrinkage and deformation of the membrane matrix, while PAN-IA samples demonstrated less shrinkage. The appearance of samples subjected to IR pyrolysis after thermal stabilization at 250°C significantly improved, practically no deformation of the structure was observed at higher pyrolysis temperatures. Without thermal stabilization, the structure of hollow fiber membranes after IR pyrolysis demonstrated significant deformation, particularly noticeable in hollow fibers impregnated with glycerol, apparently due to a more significant decrease in the pore size during pyrolysis.

5. Funding

This work was supported by Russian Foundation for Basic Research, Russian Federation (project number 20-58-00033 Bel_a) and Belarusian Republican Foundation for Fundamental Research, Belarus (project number X20P-185).

6. Acknowledgements

The authors express gratitude to D. Bakhtin for SEM images. This research was performed using the equipment of the Shared Research Center "Analytical center of deep oil processing and petrochemistry of TIPS RAS".

7. Conflict of interests

The authors declare no conflict of interest.

References

1. Choudhury S, Fischer D, Formanek P, Simon F, et al. Porous carbon prepared from polyacrylonitrile for lithium-sulfur battery cathodes using phase inversion technique. *Polymer*. 2018;151:171-178. DOI:10.1016/j.polymer.2018.07.026
2. Wu Q, Liang H, Li M, Liu B, et al. Hierarchically porous carbon membranes derived from pan and their selective adsorption of organic dyes. *Chinese Journal of Polymer Science*. 2016;34(1):23-33. DOI:10.1007/s10118-016-1723-6
3. Adams JS, Itta AK, Zhang C, Wenz GB, et al. New insights into structural evolution in carbon molecular sieve membranes during pyrolysis. *Carbon*. 2019;141:238-246. DOI:10.1016/j.carbon.2018.09.039
4. Chu Y-H, Yancey D, Xu L, Martinez M, et al. Iron-containing carbon molecular sieve membranes for advanced olefin/paraffin separations. *Journal of Membrane Science*. 2018;548:609-620. DOI:10.1016/j.memsci.2017.11.052
5. Liu J, Calverley EM, McAdon MH, Goss JM, et al. New carbon molecular sieves for propylene/propane separation with high working capacity and separation factor. *Carbon*. 2017;123:273-282. DOI:10.1016/j.carbon.2017.07.068
6. Roy S, Das R, Gagrai MK, Sarkar S. Preparation of carbon molecular sieve membrane derived from phenolic resin over macroporous clay-alumina based support for hydrogen separation. *Journal of Porous Materials*. 2016;23(6):1653-1662. DOI:10.1007/s10934-016-0226-8
7. Xu S, Lin X, He Y, Wang Z, et al. Carbon membrane performance on hydrogen separation in H₂/H₂O HI gaseous mixture system in the sulfur-iodine thermochemical cycle. *International Journal of Hydrogen Energy*. 2017;42(6):3708-3715. DOI:10.1016/j.ijhydene.2016.08.101
8. He X, Hägg M-B. Hollow fiber carbon membranes: investigations for CO₂ capture. *Journal of Membrane Science*. 2011;378(1-2):1-9. DOI:10.1016/j.memsci.2010.10.070
9. Du L, Quan X, Fan X, Chen S, et al. Electro-responsive carbon membranes with reversible superhydrophobicity/superhydrophilicity switch for efficient oil/water separation. *Separation and Purification Technology*. 2019;210:891-899. DOI:10.1016/j.seppur.2018.05.032
10. Pan Y, Wang W, Wang T, Yao P. Fabrication of carbon membrane and microfiltration of oil-in-water emulsion: an investigation on fouling mechanisms. *Separation and Purification Technology*. 2007;57(2):388-393. DOI:10.1016/j.seppur.2007.04.024
11. Fu S, Sanders ES, Kulkarni SS, Wenz GB, et al. Temperature dependence of gas transport and sorption in carbon molecular sieve membranes derived from four 6FDA based polyimides: entropic selectivity evaluation. *Carbon*. 2015;95:995-1006. DOI:10.1016/j.carbon.2015.09.005
12. Lee HS, Baek GY, Jeong SY, Shin K, et al. Preparation of thin porous carbon membranes from polyacrylonitrile by phase separation and heat treatment. *Journal of Nanoscience and Nanotechnology*. 2017;17(8):5822-5825. DOI:10.1166/jnn.2017.14135
13. Development and characterization of polyacrylonitrile(PAN) based carbon hollow fiber membrane. Available from: <https://www.semanticscholar.org> [Accessed 29 April 2024]
14. Rodrigues SC, Whitley R, Mendes A. Preparation and characterization of carbon molecular sieve membranes based on resorcinol-formaldehyde resin. *Journal of Membrane Science*. 2014;459:207-216. DOI:10.1016/j.memsci.2014.02.013
15. He X, Lie JA, Sheridan E, Hägg M-B. Preparation and characterization of hollow fiber carbon membranes from cellulose acetate precursors. *Industrial & Engineering Chemistry Research*. 2011;50(4):2080-2087. DOI:10.1021/ie101978q
16. Ma X, Swaidan R, Teng B, Tan H, et al. Carbon molecular sieve gas separation membranes based on an intrinsically microporous polyimide precursor. *Carbon*. 2013;62:88-96. DOI:10.1016/j.carbon.2013.05.057
17. Park HB, Lee SY, Lee YM. Pyrolytic carbon membranes containing silica: morphological approach on gas transport behavior. *Journal of Molecular Structure*. 2005;739(1-3):179-190. DOI:10.1016/j.molstruc.2004.08.028
18. Tena A, Rangou S, Shishatskiy S. *Method of producing a thermally rearranged PBX, thermally rearranged PBX and membrane*. United States patent 10,301,431. 28 May 2019.
19. Koros WJ, Zhang C. *Ultra-selective carbon molecular sieve membranes and methods of making*. United States patent. 15/170,529. 27 July 2016.
20. Bhave RR, Linneen NN. *Carbon molecular sieve membrane for gas separations*. United States patent 10758873 B2. 1 September 2020.
21. Hamm JBS, Ambrosi A, Griebeler JG, Marcilio NR, et al. Recent advances in the development of supported carbon membranes for gas separation. *International Journal of Hydrogen Energy*. 2017;42(39):24830-24845. DOI:10.1016/j.ijhydene.2017.08.071
22. Amirkhanov DM, Alekseeva OK, Kotenko AA, Kruchinina EV, et al. Analysis of the current state of processes for obtaining composite carbon gas-selective membranes formed under conditions of controlled carbonization of polymers. *Membrani*. 2006;4(32):19-39. (In Russ.)

23. Saufi SM, Ismail AF. Fabrication of carbon membranes for gas separation – a review. *Carbon*. 2004;42(2):241-259. DOI:10.1016/j.carbon.2003.10.022
24. Lei L, Pan F, Lindbråthen A, Zhang X, et al. Carbon hollow fiber membranes for a molecular sieve with precise-cutoff ultramicropores for superior hydrogen separation. *Nature Communications*. 2021;12(1):268. DOI:10.1038/s41467-020-20628-9
25. Zhang C, Kumar R, Koros WJ. Ultra-thin skin carbon hollow fiber membranes for sustainable molecular separations. *AIChE Journal*. 2019;65(8):e16611. DOI:10.1002/aic.16611
26. Haider S, Lie J, Lindbråthen A, Hägg M-B. Pilot-scale production of carbon hollow fiber membranes from regenerated cellulose precursor-part II: carbonization procedure. *Membranes*. 2018;8(4):97. DOI:10.3390/membranes8040097
27. Ghorpade RV, Lee S, Hong SC. Effect of different itaconic acid contents of poly(acrylonitrile-co-itaconic acid)s on their carbonization behaviors at elevated temperatures. *Polymer Degradation and Stability*. 2020;181:109373. DOI:10.1016/j.polymdegradstab.2020.109373
28. Wu S, Gao A, Wang Y, Xu L. Modification of polyacrylonitrile stabilized fibers via post-thermal treatment in nitrogen prior to carbonization and its effect on the structure of carbon fibers. *Journal of Materials Science*. 2018;53(11):8627-8638. DOI:10.1007/s10853-017-1894-8
29. Gutmann P, Moosburger-Will J, Kurt S, Xu Y, et al. Carbonization of polyacrylonitrile-based fibers under defined tensile load: influence on shrinkage behavior, microstructure, and mechanical properties. *Polymer Degradation and Stability*. 2019;163:174-184. DOI:10.1016/j.polymdegradstab.2019.03.007
30. Saha B, Schatz GC. Carbonization in polyacrylonitrile (PAN) based carbon fibers studied by ReaxFF molecular dynamics simulations. *The Journal of Physical Chemistry B*. 2012;116(15):4684-4692. DOI:10.1021/jp300581b
31. Yushkin AA, Efimov MN, Vasilev AA, Bogdanova YuG, et al. Modification of polyacrylonitrile membranes by incoherent IR radiation. *Petroleum Chemistry*. 2017;57(4):341-346. DOI:10.1134/S0965544117040089
32. Yushkin AA, Efimov MN, Vasil'ev AA, Ivanov VI, et al. Effect of IR radiation on the properties of polyacrylonitrile and membranes on its basis. *Polymer Science, Series A*. 2017;59(6):880-890. DOI:10.1134/S0965545X17060104
33. Lee WH, Bae JY, Yushkin A, Efimov M, et al. Energy and time efficient infrared (IR) irradiation treatment for preparing thermally rearranged (TR) and carbon molecular sieve (CMS) membranes for gas separation. *Journal of Membrane Science*. 2020;613:118477. DOI:10.1016/j.memsci.2020.118477
34. Renschler CL, Sylwester AP, Salgado LV. Carbon films from polyacrylonitrile. *Journal of Materials Research*. 1989;4(2):452-457. DOI:10.1557/JMR.1989.0452
35. Chernikova EV, Poteryaeva ZA, Shlyakhtin AV, Prokopov NI, et al. Effects of synthesis conditions and the mechanism of homopolymerization of acrylonitrile on the thermal behavior of the resulting polymer. *Polymer Science Series B*. 2013;55(1-2):1-13. DOI:10.1134/S1560090412110012
36. Yushkin AA, Efimov MN, Malakhov AO, Karpacheva GP, et al. Creation of highly stable porous polyacrylonitrile membranes using infrared heating. *Reactive and Functional Polymers*. 2021;158:104793. DOI:10.1016/j.reactfunctpolym.2020.104793
37. Devasia R, Nair CPR, Sadhana R, Babu NS, et al. Fourier transform infrared and wide-angle X-ray diffraction studies of the thermal cyclization reactions of high-molar-mass poly(acrylonitrile-co-itaconic acid). *Journal of Applied Polymer Science*. 2006;100(4):3055-3062. DOI:10.1002/app.23705
38. Matveev D, Vasilevsky V, Volkov V, Plisko T, et al. Fabrication of ultrafiltration membranes from non-toxic solvent dimethylsulfoxide: benchmarking of commercially available acrylonitrile co-polymers. *Journal of Environmental Chemical Engineering*. 2022;10(1):107061. DOI:10.1016/j.jece.2021.107061
39. Ju A, Guang S, Xu H. Effect of comonomer structure on the stabilization and spinnability of polyacrylonitrile copolymers. *Carbon*. 2013;54:323-335. DOI:10.1016/j.carbon.2012.11.044
40. Ouyang Q, Cheng L, Wang H, Li K. Mechanism and kinetics of the stabilization reactions of itaconic acid-modified polyacrylonitrile. *Polymer Degradation and Stability*. 2008;93(8):1415-1421. DOI:10.1016/j.polymdegradstab.2008.05.021
41. McKelvey S. Phase separation, vitrification, and the manifestation of macrovoids in polymeric asymmetric membranes. *Journal of Membrane Science*. 1996;112(1):29-39. DOI:10.1016/0376-7388(95)00197-2
42. Bilyukevich AV, Hliavitskaya TA, Nevar TN. Influence of spinning modes on the structure and properties of polyethersulfone hollow-fiber ultrafiltration membrane. *Membranes and Membrane Technologies*. 2022;4(4):195-205. DOI:10.1134/S2517751622040023
43. Bilyukevich AV, Plisko TV, Usosky VV. The formation of polysulfone hollow fiber membranes by the free fall spinning method. *Petroleum Chemistry*. 2016;56(5):379-400. DOI:10.1134/S0965544116050042
44. Kujawski W, Adamczak P, Narebska A. A fully automated system for the determination of pore size distribution in microfiltration and ultrafiltration membranes. *Separation Science and Technology*. 1989;24(7-8):495-506. DOI:10.1080/01496398908049787
45. Faraji S, Yardim MF, Can DS, Sarac AS. Characterization of polyacrylonitrile, poly(acrylonitrile-co-vinyl acetate), and poly(acrylonitrile-co-itaconic acid) based activated carbon nanofibers. *Journal of Applied Polymer Science*. 2017;134(2):app.44381. DOI:10.1002/app.44381
46. Araújo T, Parnell AJ, Bernardo G, Mendes A. Cellulose-based carbon membranes for gas separations – unraveling structural parameters and surface chemistry for superior separation performance. *Carbon*. 2023;204:398-410. DOI:10.1016/j.carbon.2022.12.062
47. Yushkin AA, Balynin AV, Nebesskaya AP, Chernikova EV, et al. Acrylonitrile-acrylic acid copolymer ultrafiltration membranes for selective asphaltene removal from crude oil. *Membranes*. 2023;13(9):775. DOI:10.3390/membranes13090775

48. Kim D, Kwon Y, Lee J-H, Kim S-J, et al. Tailoring the stabilization and pyrolysis processes of carbon molecular sieve membrane derived from polyacrylonitrile for ethylene/ethane separation. *Membranes*. 2022;12(1):93. DOI:10.3390/membranes12010093

49. Hameed N, Sharp J, Nunna S, Creighton C, et al. Structural transformation of polyacrylonitrile fibers during stabilization and low temperature carbonization. *Polymer Degradation and Stability*. 2016;128:39-45. DOI:10.1016/j.polymdegradstab.2016.02.029

Information about the authors / Информация об авторах

Ala L. Yaskevich, Cand. Sc. (Chem.), Leading Researcher, Institute of Physical Organic Chemistry, National Academy of Sciences of Belarus (IPOC), Minsk, Belarus; ORCID 0000-0003-4542-2680; e-mail: Yaskevich1909@gmail.com

Tatsiana A. Hliavitskaya, Cand. Sc. (Chem.), Leading Researcher, IPOC, Minsk, Belarus; ORCID 0000-0002-5236-7061; e-mail: thliavitskaya@gmail.com

Alexey A. Yushkin, Cand. Sc. (Chem.), Leading Researcher, A.V. Topchiev Institute of Petrochemical Synthesis, Russian Academy of Sciences (TIPS RAS), Moscow, Russian Federation; ORCID 0000-0002-0118-1515; e-mail: Halex@ips.ac.ru

Svetlana A. Pratsenko, Cand. Sc. (Chem.), Leading Researcher, IPOC, Minsk, Belarus; ORCID 0000-0002-6358-6251; e-mail: membrana@ifoch.bas-net.by

Evgenii A. Nazarov, Researcher, IPOC, Minsk, Belarus; e-mail: nazevgeny@gmail.com

Mikhail N. Efimov, Cand. Sc. (Chem.), Leading Researcher, TIPS RAS, Moscow, Russian Federation; ORCID 0000-0001-7996-474X; e-mail: efimov@ips.ac.ru

Dmitry G. Muratov, Cand. Sc. (Eng.), Leading Researcher, TIPS RAS, Moscow, Russian Federation; ORCID 0000-0002-4865-288X; e-mail: muratov@ips.ac.ru

Tatiana V. Plisko, Cand. Sc. (Chem.), Head of Laboratory, IPOC, Minsk, Belarus; ORCID 0000-0002-6534-7596; e-mail: plisko.v.tatiana@gmail.com

Alexandr V. Bilydukevich, D. Sc. (Chem), Academician, Director of IPOC, Minsk, Belarus; ORCID 0000-0003-3662-9970; e-mail: uf@ifoch.bas-net.by

Яскевич Ала Леонидовна, кандидат химических наук, старший научный сотрудник, Институт физико-органической химии Национальной академии наук Беларуси (ИФОХ НАН Беларуси), Минск, Республика Беларусь; ORCID 0000-0003-4542-2680; e-mail: Yaskevich1909@gmail.com

Глевицкая Татьяна Александровна, кандидат химических наук, старший научный сотрудник, ИФОХ НАН Беларуси, Минск, Республика Беларусь; ORCID 0000-0002-5236-7061; e-mail: thliavitskaya@gmail.com

Юшкин Алексей Александрович, кандидат химических наук, старший научный сотрудник лаборатории полимерных мембран, Институт нефтехимического синтеза им. А. В. Топчиева РАН (ИНХС РАН), Москва, Российская Федерация; ORCID 0000-0002-0118-1515; e-mail: Halex@ips.ac.ru

Праценко Светлана Анатольевна, кандидат химических наук, старший научный сотрудник, ИФОХ НАН Беларуси, Минск, Республика Беларусь; ORCID 0000-0002-6358-6251; e-mail: membrana@ifoch.bas-net.by

Назаров Евгений Артурович, младший научный сотрудник, ИФОХ НАН Беларуси, Минск, Республика Беларусь; e-mail: nazevgeny@gmail.com

Ефимов Михаил Николаевич, кандидат химических наук, ведущий научный сотрудник, ИНХС РАН, Москва, Российская Федерация; ORCID 0000-0001-7996-474X; e-mail: efimov@ips.ac.ru

Муратов Дмитрий Геннадьевич, кандидат технических наук, ведущий научный сотрудник, ИНХС РАН, Москва, Российская Федерация; ORCID 0000-0002-4865-288X; e-mail: muratov@ips.ac.ru

Плиско Татьяна Викторовна, кандидат химических наук, заведующий лабораторией, ИФОХ НАН Беларуси, Минск, Республика Беларусь; ORCID 0000-0002-6534-7596; e-mail: plisko.v.tatiana@gmail.com

Бильдюкевич Александр Викторович, доктор химических наук, академик, директор ИФОХ НАН Беларуси, Минск, Республика Беларусь; ORCID 0000-0003-3662-9970; e-mail: uf@ifoch.bas-net.by

Received 04 July 2024; Accepted 30 August 2024; Published 22 October 2024



Copyright: © Yaskevich AL, Hliavitskaya TA, Yushkin AA, Pratsenko SA, Nazarov EA, Efimov MN, Muratov DG, Plisko TV, Bilydukevich AV, 2024. This article is an open access article distributed under the terms and conditions of the Creative Commons Attribution (CC BY) license (<https://creativecommons.org/licenses/by/4.0/>).

Structure control of metal-carbon composites with different nanotopological configurations and electrical conductivity characteristics in a laser experiment

© Dmitry N. Bukharov^a✉, Darya D. Tumarkina^a, Alexey O. Kucherik^a, Alexey G. Tkachev^b, Sergei M. Arakelian, Irina V. Burakova^b, Alexander E. Burakov^b

^a Vladimir State University,

87, Gorky St., Vladimir, 600000, Russian Federation,

^b Tambov State Technical University, Bld. 2, 106/5, Sovetskaya St., Tambov, 392000, Russian Federation

✉ buharovdn@gmail.com

Abstract: The paper examines the control of functional characteristics, particularly electronic transport properties, in inhomogeneous surface nanostructures of a topological class on a solid substrate, with a focus on enhancing electrical conductivity and controlling its modes in cluster-type metal-carbon composites. From the perspective of general solid-state physics, particularly for granular metals, the discussion centers on structural microcrystalline defects, specifically at the nanoscale in this case. The study involves the modeling of the formation of such systems with nanocluster structures within the context of digital materials science, demonstrating several experimental results. This is done under conditions of introducing nanotubes into a non-conductive matrix as additives with an optimal concentration, or conversely, introducing metal atoms (typically noble metals) into a nanotube system. A two-stage process is considered, involving laser ablation of various targets, including the initial stage of obtaining nanoparticles and nanoclusters with a sufficiently large number of atoms in colloidal systems in specific liquids. In the second stage, subsequent deposition onto a solid, usually dielectric, surface is implemented to create a matrix with the desired geometry and specified nanocluster topology. The studied effects and the possibility of controlling them using laser methods hold great promise for the development of micro- and nanoelectronics components and systems based on new physical principles. Trends and tendencies in the synthesis of high-temperature superconducting states in topological structures of various classes are also discussed.

Keywords: laser ablation; nanocluster models; carbon nanofibers; fractal structures; electrical conductivity; self-healing of cracks; 1-D metal-carbon assemblies of different organizations.

For citation: Bukharov DN, Tumarkina DD, Kucherik AO, Tkachev AG, Arakelyan SM, Burakova IV, Burakov AE. Structure control of metal-carbon composites with different nanotopological configurations and electrical conductivity characteristics in a laser experiment. *Journal of Advanced Materials and Technologies*. 2024;9(3):207-235. DOI: 10.17277/jamt.2024.03.pp.207-235

Управление структурой металлоуглеродных композитов разной нанотопологической конфигурации и характеристики электропроводимости в лазерном эксперименте

© Д. Н. Бухаров^a✉, Д. Д. Тумаркина^a, А. О. Кучерик^a, А. Г. Ткачев^b, С. М. Аракелян, И. В. Буракова^b, А. Е. Бураков^b

^a Владимирский государственный университет имени Александра Григорьевича и Николая Григорьевича Столетовых, ул. Горького, 87, Владимир, 600000, Российская Федерация,

^b Тамбовский государственный технический университет, ул. Советская, 106/5, пом. 2, Тамбов, 392000, Российская Федерация

✉ buharovdn@gmail.com

Аннотация: Рассмотрены в неоднородных поверхностных наноструктурах топологического класса на твердом теле вопросы управления функциональными характеристиками, в частности, электронными транспортными свойствами для задач повышения электропроводимости и управления ее режимами в металлоуглеродных

композитах кластерного типа. В аспекте общих положений физики твердого тела, в частности, для гранулированных металлов, речь идет о структурных мелкокристаллических дефектах, в данном случае – наномасштабных. В условиях внедрения нанотрубок в непроводящую матрицу как присадки с оптимальной концентрацией, или наоборот – атомов металлов (обычно – благородных) в систему из нанотрубок проведено моделирование формирования подобных систем с нанокластерными структурами в аспекте цифрового материаловедения с демонстрацией ряда экспериментальных результатов. Рассмотрена двухэтапная схема с лазерной абляцией различных мишеней, в том числе, и через первый этап получения наночастиц и нанокластеров с достаточно большим числом атомов в коллоидных системах в определенных жидкостях. На втором этапе реализуется последующее их осаждение на твердотельную, как правило, – диэлектрическую, поверхность – с получением матрицы требуемой геометрии с заданной топологией нанокластеров. Исследуемые эффекты и возможность управления ими лазерными методами имеют большую перспективу при разработке элементов и систем микро- наноэлектроники на новых физических принципах. Обсуждаются тренды и тенденции в синтезе высокотемпературных состояний в сверхпроводимости в топологических структурах разного класса.

Ключевые слова: лазерная абляция; модели нанокластеров; углеродные нановолокна; фрактальные структуры; электропроводимость; самозарастание трещин; 1-D металлоуглеродные ансамбли разной организации.

Для цитирования: Bukharov DN, Tumarkina DD, Kucherik AO, Tkachev AG, Arakelyan SM, Burakova IV, Burakov AE. Structure control of metal-carbon composites with different nanotopological configurations and electrical conductivity characteristics in a laser experiment. *Journal of Advanced Materials and Technologies*. 2024;9(3):207-235. DOI: 10.17277/jamt.2024.03.pp.207-235

Introduction

The issue of the sharp increase in electrical conductivity of various materials, including understanding the physical principles to achieve high-temperature superconducting states, has long been a key topic in many fundamental interdisciplinary studies [1].

Typically, this involves finding the appropriate elemental chemical composition and physicochemical properties of synthesized objects and solid solutions (see, for example, [2]). However, the structural configuration of these materials is also of crucial importance, especially for metal-carbon composites with various nanocluster forms, sizes, and additives, particularly carbon nanotubes (cf. [3]). The focus here is on thin-layered/multilayered surface structures of solid samples with objects of different dimensionalities – from 0D to 3D – and their combinations, which in our case are obtained experimentally through laser ablation of target surfaces with selected compositions [4].

When discussing the electronic spectra of nanocluster structures on the scale of nanometers for metals and semiconductors within the realized matrix, they can be considered similarly to conventional solid bodies. Despite this, the properties of nanocluster structures significantly differ from those of bulk samples due to the large surface area in nanocluster arrays and potential charge separation at the interphase boundary, which leads to shifts in atomic levels [3, 5]. Size effects and contact potential differences at the interfaces, such as those between gold atoms on a graphite substrate of highly oriented pyrolytic graphite due to differing Fermi levels, can result in an excess number of electrons in gold

clusters (cf. [6]). The interactions that arise between these elements are also important.

In this regard, the following features of electrophysics in such compounds, which contain metallic (usually noble metals) and semiconductor nanoparticles, can be noted. Their spatial configuration and distribution are determined by controlled conditions during the selected laser experiment, which promote the emergence of correlated charge topological states in the system with defects/vacancies, leading to a sharp increase in electrical conductivity – by many orders of magnitude in some cases [7, 8]. This is determined both by the individual characteristics of isolated nanoclusters and by their interactions with neighboring clusters and with substrates of various types. We use the term «electrical conductivity» rather than the more commonly accepted «electrical conductance» to emphasize that we are referring to a discrete nanocluster structure.

Let us list a number of conditions for the manifestation of these phenomena.

Firstly, this concerns the possibility of realizing states in topological nanostructures with characteristics analogous to those found in topological insulators. These states are associated with specific boundary conditions, surface areas between constituent elements, and the trajectories of charge carriers moving through vacant regions (cf. [9]). Crucially, the topological parameters function similarly to thermodynamic parameters in phase transitions, particularly with regard to temperature. Thus, in the presence of certain surface state configurations within the matrix of nano-objects, they influence electronic states, which may become

correlated, leading to a significant improvement in electrophysical properties (cf. [10]). For instance, in such systems, electrical conductivity is realized through electron transfer along various trajectories within this matrix. However, surface concentration and the density of electronic states compared to their number in the conduction band, as well as the presence and type of various impurities and vacancies, are also important factors [11].

In our experiments, we observed a reduction in electrical resistance by up to 10^4 times in planar thin-film nanocluster structures with a specific topology [12, 13]. This suggests potential approaches and trends in the study of high-temperature superconductivity. A characteristic of this effect is a significant decrease in the density of states near the Fermi level, known as the pseudogap state, which is typical, for example, of disordered semiconductors [14]. This could also involve nanoscale disorder within the nanocluster structure. Here, we do not address effects involving quasiparticles and exciton-polariton states. Essentially, this pertains to quantum size effects.

Secondly, there is a specific nature of physical states in highly heterogeneous nanostructures with fractal dimensionality, where significant increases in local fields can be realized (for nanometer-scale objects, up to 10^8 V·cm⁻¹ during laser ablation of a metal target using standard nanosecond laser radiation with pulse energy of around 0.1J) [15]. In such cases, the macroscopic functional properties, including electromagnetic characteristics, of these composite samples change dramatically. In metals/steels, this is typically discussed in terms of dendritic structures with varying organization [16]. Under these conditions, electron hopping processes between neighboring dendrite peaks, which are temperature-dependent, can occur. This thermally activated hopping conductivity involves variable hopping lengths (cf. [17]).

Thirdly, considering the generally increasing electrical polarizability in systems with carbon nanotube additives (with varying diameters and lengths, porous structures, and nanofibers) and the presence of 1D directions with high aspect ratios (length-to-diameter ratio up to tens of thousands), electrical resistance in such regular configurations for a given direction of charge propagation can significantly decrease [18]. However, the effect in a nanostructured matrix depends on the specific organization of charge distribution and the uniform orientation of the 1D structures in the ensemble, forming a chain (in the simplest case – a percolation chain, essentially with a functional dependence

similar to metallic conductivity) [19]. This can result in high specific electrical conductivity, comparable to that of an isolated carbon nanotube, reaching approximately 10^6 S·m⁻¹ [20]. This changes the material's classification based on its electrical conductivity. Significant experimental results with practical applications can be expected in the near future.

Crucially, it is the addition of carbon nanotubes, rather than other well-conducting additives, that leads to this sharp increase in electrical conductivity. However, the possibility of controlled electrical resistance at their contact points is also important [21]. This is especially significant for the sensitivity of sensor systems using carbon nanotubes and nanofibers. If there is no direct contact between neighboring such objects, charge transfer occurs, for example, through a tunneling mechanism, which exhibits a specific temperature dependence (cf. [22]).

Fourthly, even under stochastic processes in nanostructured materials, various extreme states can occur in the dynamic characteristics of charge carriers, particularly during their movement along a separatrix, bypassing scattering centers (cf. [15, 23]). This also affects the electrical conductivity.

Another topic worth considering is the twisted and intertwined ensembles of nanotubes, such as bundles and/or sponge-like structures, as well as the shape of individual carbon nanotubes that do not conform to the ideal cylindrical form. When dealing with an inhomogeneous distribution of carbon nanotubes, it is important to account for their interactions, such as Van der Waals forces [3, 24]. All of this leads to nonlinear effects in electrical conductivity, which exhibits a non-ohmic dependence and requires quantum analysis for understanding, considering a hybrid mechanism of conductivity – both within each cluster and within the matrix on which they are situated. This also depends on the concentration of clusters and the effect of charge tunneling between them, modeled as quantum wells and barriers under conditions of thermally activated hopping processes (cf. [25]).

In this partially review-based article (largely based on our own research), we have examined all of these issues to some extent in the context of controlling conductivity characteristics.

1. Basic physical principles and methodologies

In all cases involving spatially inhomogeneous heterogeneous media at the micro- and nanoscale, it is necessary to employ various models with numerical simulations and calculations for charge carriers (see section 2 below for general principles,

and section 3 for carbon nanocomposites). This applies both to diffusion processes of their propagation and to classical percolation mechanisms (where the threshold becomes negligible with the high aspect ratio of carbon nanotubes) with conductive channels [26, 27]. These channels also emerge in contacts between heterogeneous nanocluster blocks. These simple models accurately reflect the overall trend but sometimes fail to account for significant features, particularly the imperfections and inhomogeneity of carbon nanotube chains that are in contact with each other. Therefore, numerical modeling is required, incorporating additional physical concepts and using high-level programming languages (cf. [28]).

For quantum electronic states, the well-known core-shell model is constructive, allowing for single-electron states in various types of topologies within the created nanostructures [29]. In this case, it becomes possible to control the bandgap width, the depth of impurity levels, the density of electronic states near the Fermi levels, and the emergence of various resonances (e.g., plasmonic resonances in metallic objects) as a result of changes in topological features. These conductivity processes can also be threshold-based, demonstrating step-like trigger behavior (cf. [4, 7, 30]). Moreover, their charge state can be controlled in a specific manner, which is important for various practical applications. Sensor systems with nanofibers in a distributed double-cylinder structure model, analogous to the localized core-shell model, are particularly promising here [31].

The topic of this study is of particular interest in the production of artificial diamond crystals, especially within metal-carbon nanocomposite systems, which we examine in this article under laser irradiation. These crystals can crystallize into various crystallographic forms with possible different types of inclusions. The additives with carbon nanotubes, as well as the processes of surface graphitization of the diamond itself, are of fundamental importance in controlling properties such as the electrical conductivity of these structures.

Universal phenomena of twinning can occur in these materials, either with or without changes in the shape of crystal fragments. Two mechanisms of twinning are distinguished – diffusionless and diffusion-based mechanisms, analogous to the nonlinear process of mechanical twinning during martensitic phase transformations. This topic has been studied for nearly 130 years, with particular emphasis in the latter half of this period. A modern review of the research status in this field is presented, for example, in [32], but several unresolved issues

remain even when considering multifactorial models. These issues pertain to the following phenomena.

The diffusionless mechanism involves the formation of oriented regions and/or layers with the alignment of the crystal lattices of the new and old phases along their boundary of contact, with a specific arrangement of atoms. For diamond, such twinning along the (111) plane, for example, generally does not create defects in the lattice structure.

The other mechanism – the diffusion-based one – is associated with the nucleation of crystallization centers followed by the attachment of individual atoms or small groups of atoms, whose diffusion determines the growth rate of the new phase crystals within the original structure and/or in the growing crystal. In this process, the modification of the crystal structure occurs due to the relative movement of atoms over interatomic distances. This phenomenon is typically considered to be associated with changes in the concentration of the original components; however, this does not apply to the transformation of graphite into diamond or the graphitization of diamond.

To briefly characterize the difference between these two twinning mechanisms, in martensitic transformations, the lattice modification involves the displacement of atoms relative to each other over distances no greater than interatomic distances, without an exchange of positions.

These patterns are generally characteristic of diamond-like compounds within this crystallographic class, which also includes compounds with varying elemental compositions.

The discussion of this twinning phenomenon is important for us because it depends on external influences and thermodynamic conditions, and we are specifically examining laser methods of such influence. In our case, we are dealing with controlled mechanisms under different modes of laser irradiation of samples, with adjustable and selectable spatial-temporal characteristics of the laser radiation – such as laser pulse duration, laser beam parameters, and the duration or scanning time of its impact on the object. This specificity of the laser experiment is crucial for the development of physical processes.

These conditions can be considered a type of laser ablation from the target surface under certain experimental conditions, leading to the formation of dislocations and stresses in areas with twinned layers, which significantly determine the functional characteristics of the samples obtained after this treatment. In some cases, this may result in the formation of quantum dots, graphene/ribbon structures, and diamond-like crystalline micro-objects

with variable lattice states (cf. [12]). Such objects are analogous to photonic crystals widely used in topological photonics, as well as lattice states with vacancies in which atoms of various elements can be embedded (cf. [3, 12, 33]), enabling different twinning mechanisms. This process can be described in terms of topological twinning.

Additionally, the properties of nanocatalysts containing metallic nanoparticles, particularly those used in the synthesis of nanotubes with record yields on an industrial scale, strongly depend on the size and shape of the nanoparticles and their associated charge effects, which influence the catalytic activity of the structures used [34].

In this context, laser ablation methods involving the agglomeration and/or fragmentation of metallic nano-objects appear to be highly promising and versatile, particularly due to the correlated relationship between the electrical and catalytic properties of the synthesized nanostructures and the specified optimal parameters.

Here, we focus on two-stage schemes involving laser ablation of various targets, including an initial stage where nanoparticles and nanoclusters with a relatively large number of atoms are produced in colloidal systems within specific liquids. In the second stage, these particles are subsequently deposited onto a solid, typically dielectric, surface, resulting in a matrix with the required geometry and topology of nanoclusters on the solid surface [4, 15, 33]. Of particular interest is the deposition of nanoparticles from the colloid onto conductive material substrates, such as highly oriented pyrolytic graphite plates (cf. [3, 35]). The difference in the experiment between these two types of substrates – conductive and non-conductive – lies in the characteristics of the charged states of nanostructures on the substrates [36]. For non-conductive substrates with metallic nanoparticles, they become charged only in ensembles with a certain quantity of them. For conductive substrates, the charged nanoparticles remain isolated (cf. [3]).

In general, the charge and field states of nanoparticles depend on their mutual arrangement. We will present various configurations of similar structures obtained in our laser experiments as a result of several technological stages; one outcome, in particular, is the sintering of a prepared nanotube ensemble on a plate doped with gold atoms (see section 4). Such systems may be of interest in the development of sensor films based on the electrical conductivity of nanocomposites, which utilize charge transfer between the contacting elements of the composite with different work functions. Of special

importance here is the laser-induced graphitization of diamond, which is a dielectric but begins to exhibit semiconductor properties with tunable characteristics in certain induced structures [3, 37].

The technology of laser fragmentation used in sample production allows, on one hand, the formation of ultrathin atomic-scale layers. On the other hand, it enables the synthesis of isolated quantum dots, which can be the basis for creating laser diode sources in desired spectral ranges. This refers to quantum-sized nanostructures of different classes. Of particular interest are quantum cascade lasers, which involve transitions between electronic states within a quantum well of a single band, rather than the usual electron-hole recombination system (with transitions between the conduction and valence bands) (cf. [15, 38]).

However, in this work, we will focus solely on the structural and topological aspects of controlling electronic transport properties to enhance electrical conductivity and manage its modes in such structures. In the context of general principles of solid-state physics, particularly for granular metals, we can discuss structural fine-crystalline defects, which in this case are nanoscale. We will also consider (see section 3.5) a certain structural helical model for electrical conductivity in a specific stable configuration. An analogous configuration may be achievable in a laser experiment with a specific strategy: scanning the laser beam with a selected laser pulse duration.

When it comes to embedding nanotubes into a non-conductive matrix as additives with optimal concentration, or conversely, embedding metal atoms (usually noble metals) into a nanotube system, the interactions between them become important. In section 4, we will examine the second case of such a composite – sintering a nanotube powder with gold atoms using graphite-shungite.

2. Modeling of nanocluster complexes using noble metals in colloidal systems under laser exposure

We present a universal model for synthesized nanoclusters on a solid substrate surface. This model can be applied to clusters of any composition, but for clarity and further discussion, we will consider a system of noble metals (cf. [15]).

Colloidal systems of noble metal nanoparticles (Ag, Au) were formed by exposing bulk targets (composition: Au – 99.9 %, Ag – 99.9 %) placed in liquid media to laser radiation of moderate intensity (up to $10^6 \text{ W}\cdot\text{cm}^{-2}$) at a wavelength of $1.06 \mu\text{m}$. To deposit nanoclusters from the solution onto a substrate, we used a method of thermomodiffusion

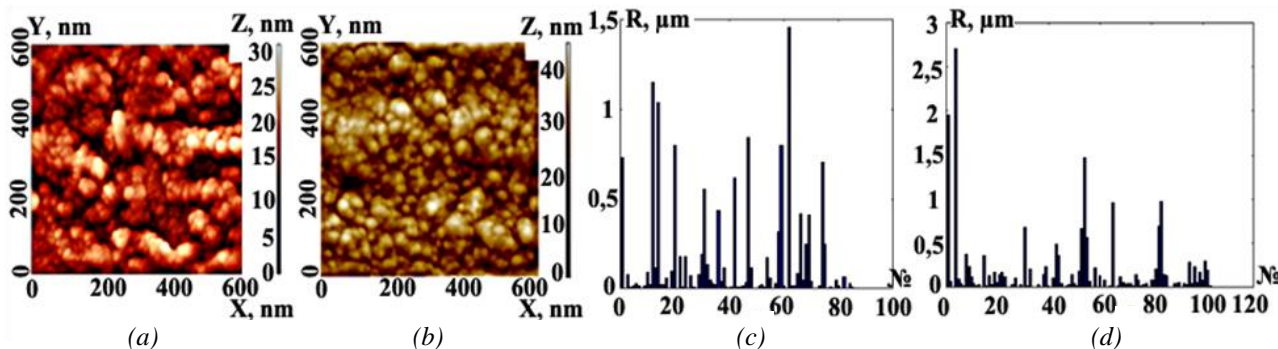


Fig. 1. AFM images of bimetallic (Ag/Au) nanocluster systems at a laser beam scanning speed of $1.2 \text{ mm}\cdot\text{s}^{-1}$ after 15 (a) and 20 (b) passes. The size distribution (spatial scales are shown on the axes) of the objects in the samples: for Fig. 1a – with the histogram (c) and for Fig. 1b – with the histogram (d); the vertical axis indicates the object sizes R , and the horizontal axis indicates the numbers of the studied objects

deposition onto glass from a colloidal solution obtained by intensively mixing noble metal nanoparticles (Ag, Au, and/or Ag/Au mixture, with an average particle size of 100 nm) with glycerin [39]. After laser exposure, the colloidal systems were studied using a Horiba LB-550 particle size analyzer based on dynamic light scattering. Images of the nanostructures deposited on the substrate were captured using a Quanta 200 3D scanning electron microscope and an Integra-Aura probe nanolaboratory.

The study of the sample surface (Fig. 1), conducted using the MATLAB Image Processing Toolbox [40], revealed the clustered nature of the nanoparticle system, with well-defined agglomerates ranging in size from 1 to 3 μm and average heights from 10 to 40 nm, as seen in the images obtained using atomic force microscopy (AFM) (Fig. 1a, b).

When deposited from single-component colloids (Ag or Au), the synthesized systems consisted of isolated fractal nanocluster dendrites with a disconnected surface topology (Fig. 2). Objects ranging from 10 to 300 nm were clearly visible. Their sizes exceeded those of the nanoparticles in the original colloidal system (5–20 nm). This observation indicates the thermodiffusion nature of the formation of nanocluster systems, with a preliminary aggregation process of the nano-objects in the colloidal solution prior to deposition on the substrate.

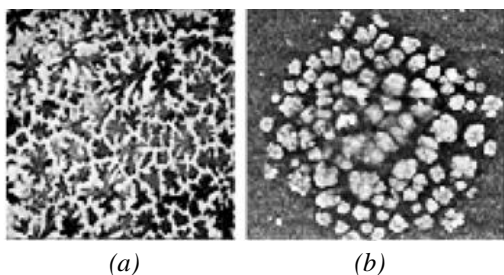


Fig. 2. AFM images of the Ag (a) and Au (b) nanocluster systems

When forming nanocluster systems from a two-component colloidal solution (Au/Ag at a concentration ratio of 50/50), samples with a more heterogeneous and sparse spatial structure of a cluster nature were obtained. However, the process resulted in the unification of objects into a single structure, similar to alloy formation, in this case with a connected surface topology. This observation suggests the presence of melting in the system with nano-objects during the formation of this unified cluster.

However, we did not consider the thermodynamic processes for this mechanism, which would require calculations of the entropy values for such alloys (this is a separate task, which we have conducted for diamond-like compounds, specifically in [12, 33]). Here, we were only interested in classifying them by their fractal dimension values. The fractal dimensions of the obtained samples were estimated using the box-counting method [41], which confirmed their dendritic nature. For example, the fractal dimension of the sample in Fig. 2a was $D = 1.898$, and for the sample in Fig. 2b, it was $D = 1.922$. These values are quite consistent with the estimates of fractal dimensions of dendritic structures known from the literature [42]. The accuracy of determining these numerical values of D corresponds to the standards accepted in fractal mathematics (cf. [23]).

The modeling of the cluster formation process was carried out within the framework of diffusion-limited aggregation (DLA) [43], which describes aggregates both in the colloidal system and in their structures deposited on a solid surface.

In general, the algorithm for forming DLA structures is implemented as Brownian motion of a particle within a computational domain containing a seed structure, followed by aggregation/attachment with a given probability. Various modifications of the

general DLA case allow for the consideration of thermal processes occurring during aggregation in colloidal systems. The DLA model and its transformation, taking into account additional factors, can be implemented using cellular automata techniques with von Neumann and/or Moore neighborhoods [44]. For instance, using the von Neumann neighborhood allows for the creation of samples with a heterogeneous structure, while the Moore neighborhood produces well-filled, homogeneous samples (see more details in the Appendix).

To describe convective flow in the region heated by laser radiation, it is convenient to use the standard Rayleigh-Bénard model (in the case of a point heater located at the bottom) for planar geometry within the Boussinesq approximation [45], accounting for its rotation by a certain angle. We employed this model to estimate the resulting nanocluster configurations in a controlled manner (cf. [15]) with the corresponding temperature field [46] on the substrate.

By varying the probability of agglomeration (adhesion) s , it is possible to model dendritic structures of various shapes (Fig. 3). For small values

of the adhesion probability, well-filled, fairly homogeneous clusters with a smooth boundary and a fractal dimension D of about 1.85–2.02 are formed. For large values of the adhesion probability s , heterogeneous clusters with a highly jagged boundary and a lower fractal dimension $D \sim 1.70$ –1.85 are formed. For instance, the model in Fig. 3 can be correlated with certain elements of the nanocluster system in the samples from Fig. 2a, b. In this case, there is a qualitative similarity between the topologies of the model and the experimental sample.

The conducted studies revealed the fractal nature (following a diffusion mechanism) of the structures, which corresponded to the selected approximation during modeling. The initial distribution of seed structures within the computational area, as well as the adhesion probability s , influences the shape of the aggregates. For instance, Fig. 4 shows 3D model images of DLA clusters in a.u. based on a cellular automaton in the von Neumann neighborhood. The cluster systems were formed within a sphere at the center of the computational area for the case $s < 1$ (Fig. 4a) and $s < 0.1$ (Fig. 4b), as well as in the case of aggregation from a point at the center (Fig. 4c and 4d).

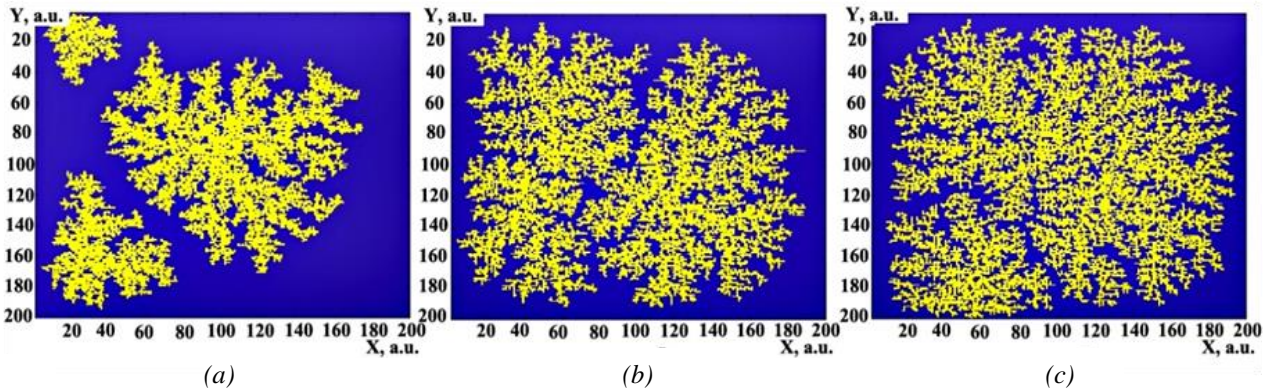


Fig. 3. A variety of fractal structures on a relative scale, generated by varying the adhesion probability s .

As an example, starting with three aggregation centers (clearly visible in Fig. 3a):

with a parameter value of $s = 0.1$, we have $D = 1.85$ (a); with $s = 0.5$, $D = 1.80$ (b); and with $s = 1$, $D = 1.79$ (c)

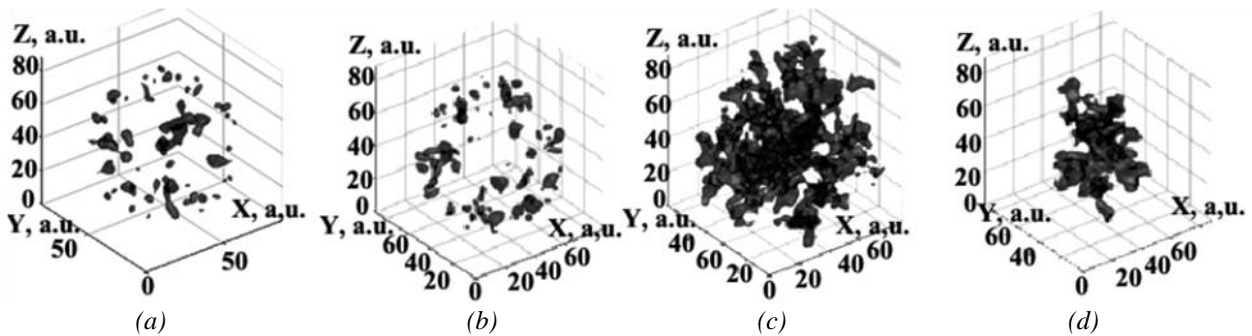


Fig. 4. DLA clusters: A seed within a sphere at the center, where an aggregate is formed with probability $s < 1$ (a); $s < 0.1$ (b). The seed is at the center, and the aggregate forms across the entire computational domain for two values $s < 1$ (c); $s < 0.1$ (d)

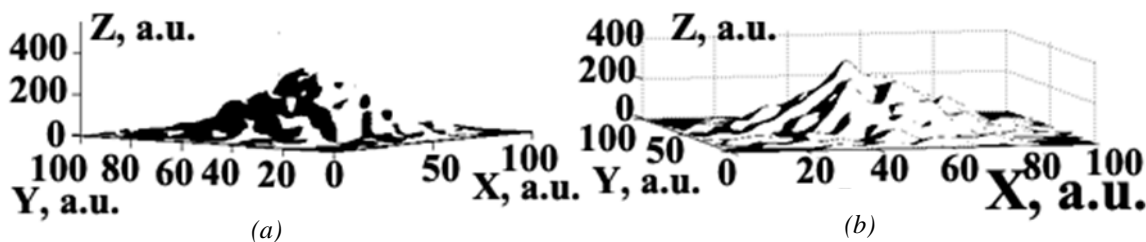


Fig. 5. DLA structure of clusters with varying height h , deposited on a surface: when $s = 1$ (a); when s depends on the current maximum height of the emerging structure (z – axis) with a maximum selected dendrite height of $H = 240$ a. u. (b)

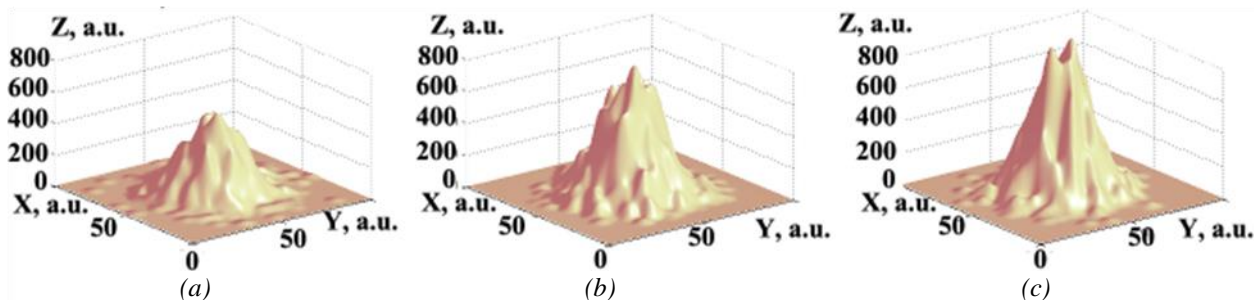


Fig. 6. Model of the deposited structure with $s=1$ (a); $s = 0.5$ (b); and with a continuous decrease over time of s values from the initial value of 1 to the final value of 0.001 (c)

Figure 5 shows model qualitative images of a system of fractal/dendritic nanoclusters in Cartesian coordinates in a.u., deposited from a colloidal solution onto a solid substrate. They were formed within the framework of the DLA model, where a horizontal plane (x, y) was chosen as the seed structure, and the value of s was set to 1 (Fig. 5a). The case was also considered where the variable value of s depended on the current maximum height h of the forming structure, as shown in the figure (Fig. 5b). This value increases to the required maximum height $h = H$ (see Fig. 6). In this model, we assume that $s = h/H$, so that over time, the value of s increases from 0 ($h = 0$) to 1 ($h = H$).

Figure 6 shows the qualitative dynamics of changes in the cluster structure when determining the value of the parameter s .

From Figure 6, it can be concluded that a high adhesion probability s allows the formation of structures that are not tall but have a wide base. Conversely, small values of s lead to cluster systems consisting of long, narrow “nanopeaks”.

The comparison of simulation results (Figs. 4–6) with the experiment (see Figs. 1 and 2) showed a qualitative agreement, indicating a good level of adequacy of the proposed model.

The computational experiments and their statistical analysis demonstrated that the DLA model allows the creation of fractal clusters with dimensions

ranging from 1.67 to (2.02 ± 0.03) when varying the adhesion probability s within the interval [1; 0.01] (Fig. 7). Values exceeding a dimension of 2 suggest the formation of 3D structures.

In turn, the temperature dependence of the fractal dimension D can be represented as (compare with [25, 45]):

$$D(T) \sim A_0 T^\alpha,$$

where A_0 and α are some empirical proportionality coefficients.

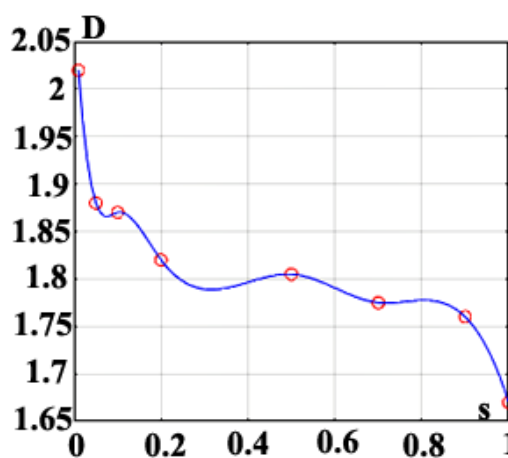


Fig. 7. The dependence of fractal dimension D on the adhesion probability s : points represent the calculated values, and the line represents the approximation, taking into account cubic spline interpolation in MATLAB [40]

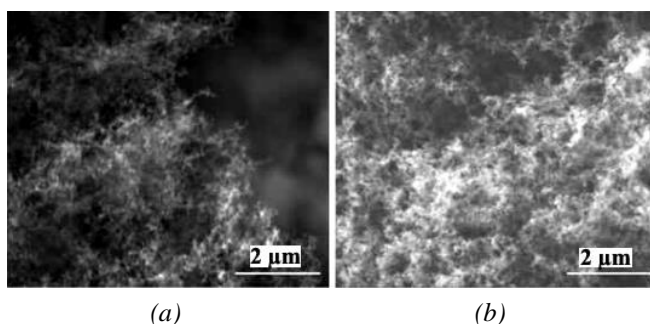


Fig. 8. SEM images of nanofibrous carbon structures subjected to the same laser beam but with different values of external electric voltage applied to the sample: 1 kV (a), 0.8 kV (b) [48]

The anisotropy of the computational domain can be defined through the temperature field in the laser beam (see [4]). Then, with the temperature distribution in the plane case on the substrate surface in the form of a system of isothermal regions, it becomes possible to estimate the adhesion probability for a wandering particle upon entering a given isothermal region (compare with [39]). In this case, the random displacements of the particle during its wandering are not equally probable. This method of accounting for anisotropy allows consideration of the direction of particle diffusion into the laser heating area as an increased probability of random displacements (see [46]).

3. Modeling the carbon nanofiber system

In this section, we will examine in detail models involving carbon materials based on nanofibers, which are promising, for example, in the development of nano-microelectronics components and systems [3, 15, 47].

One convenient method for synthesizing carbon nanofibers is by exposing the medium to laser radiation in the presence of an external electric field. Using this method, as described in [48], we obtained carbon nanofibers deposited on a metal plate (Fig. 8). The structure of the synthesized samples indicates the controllability of the topological characteristics of nano-objects by selecting appropriate experimental parameters: laser radiation characteristics and the intensity of the externally applied electric field. For instance, Figure 8 shows a sample nanofiber structure at various specified external voltages.

3.1. General principles

The obtained samples, under different values of control parameters, were studied using scanning probe microscopy (SPM) and Raman spectroscopy. The morphological properties were investigated

through fractal analysis of the dimensions of the nanofiber images obtained with a scanning electron microscope; this analysis was conducted using the box-counting method [49]. Depending on the deposition time and the power of the laser radiation source, it is possible to control the fractal dimension value. For example, it gradually increased from 1.45 to 1.9 with laser radiation power of 30 W; from 1.6 to 1.96 with a power of 50 W; and from 1.75 to 1.98 with a power of 100 W, while the deposition time under laser radiation remained constant in all cases.

As mentioned above, a convenient model that allows for generating structures with fractal dimensions and accounting for thermal processes is the DLA model [49, 50]. The nanofiber model in the DLA approximation was implemented as a cellular automaton with a Moore neighborhood [51] (see Appendix P.1). The influence of the medium's thermodynamic characteristics was accounted for in the aggregation/adhesion probability coefficient s , which was represented as a normalized diffusion coefficient within the interval (0; 1].

Figure 9 shows model images of nanowires (filamentary objects) with nanofragments (though in a. u., they depend on the control parameter – adhesion probability s and branches on their predominantly linear structure in the DLA approximation within a computational domain of 300×300 a. u. for 30,000 particles. In Figure 9a, the case of equal-probability displacement of diffusing nanoparticles with a constant $s=1$ is shown. Figure 9b presents a model of the nanowire system with small lateral displacements of the diffusing particles and a uniform decrease in the adhesion probability from 1 to 0.01. Figure 9c depicts a nanowire system with small lateral displacements of diffusing particles and a uniform decrease in the adhesion probability s , from 0.5 to 0.01. The case of small lateral displacements of diffusing particles allows for qualitatively accounting for the effect of the applied external electric field, where the structure growth occurs predominantly along the lines of the field's intensity. The above-mentioned change in adhesion probability corresponds to the cooling of the system after laser exposure, analogous to experimental conditions. In both cases, the generation process stopped when the nanowire reached the upper boundary of the computational domain. Comparing Figures 9a, 9b, and 9c, it can be concluded that the probability of random lateral displacements affects the shape of the nanowire. In the case of low lateral displacement probabilities, the nanowires generated are more vertically elongated with smaller and fewer lateral branches.

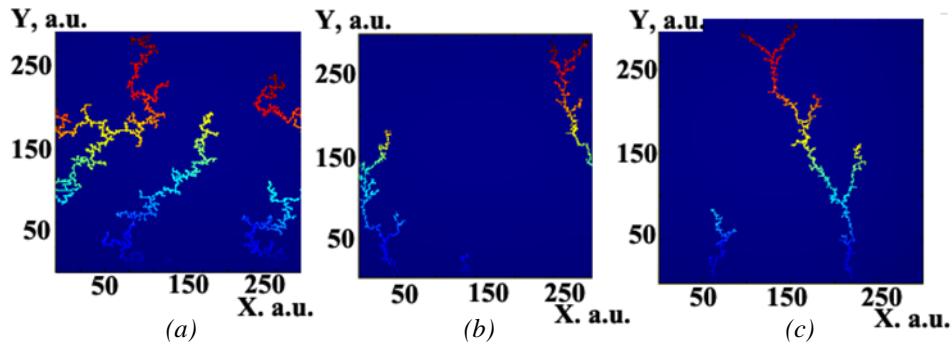


Fig. 9. Models of nanowire systems in the DLA approximation:

- (a) equal-probability displacements of diffusing particles with a constant value of $s = 1$;
 (b) small lateral displacements of diffusing particles with a uniform decrease in s from 1 to 0.01;
 (c) uniform decrease in s from 0.5 to 0.01

Switching to absolute units allowed for a comparison between the model and experimental results in terms of assessing the local lengths of the simulated fractal nanostructures. By setting the side length of the computational cell in the model to 10 nm, the maximum length of the nanowires was found to be between 3000 and 3900 nm in the case of equal-probability displacements. This may correspond to the generation of nanowires in the presence of a weak external electric field. The range of maximum lengths, from 3000 to 3400 nm, in the case of small lateral displacements is characteristic of nanowires generated under a stronger electric field.

These values qualitatively match the results of experimental measurements, and the models used can be useful for predicting and evaluating the geometric properties of nanowires (cf. [48]).

3.2. Laser-induced 1D carbon filamentary fractal structures on solid surfaces: models and experimental implementation

The electrophysics of systems with different spatial dimensionalities (from 0D to 3D) is related to symmetry factors and their modification under conditions of topological phase transitions. This determines various electronic states that depend on the shape, size, and spatial distribution of such objects, typically on the surface of a solid body (see, for example, [4, 52]). Recently, such systems have been intensively studied in terms of “strange” crystalline/metallic structures [53] and other specific objects [54], which are important for practical applications.

The key control parameters here are the dimensional ratios, such as the distance between clusters r compared to their size l , and/or similar ratios within each cluster for nanostructures within it. The physical significance lies in how deeply (h) into

a given topological object – a cluster or its elements – interactions from their surroundings penetrate. For the entire cluster array on the substrate, this concerns its extent L compared to the size of one cluster l , meaning the ratio of these parameters can be very large (cf. [15, 55]).

This is associated with pairwise interactions between nearest neighbors, which define nonequilibrium/strained states on their separating surfaces (cf. [56]). Specifically, as the surface area with negative surface tension increases, such states become thermodynamically more favorable in energy terms. Although the general process of forming these objects with negative surface tension is unstable, under extreme conditions—such as laser ablation in a liquid – it can be considered locally isobaric, fixing the configuration of objects and maintaining it when returning to normal conditions (cf. [15]). This significantly alters the functional characteristics of samples with a specific array of these structures, which is quite controllable.

Such surface effects in a thin layer were observed in our experiments [12, 13, 57], where, depending on the topology of the fractal surface cluster configurations, the electrical resistance of the sample could decrease significantly – up to 10^4 times – under similar resistance measurement schemes across the homogeneous surface area of the sample (see, for example [7]).

In this context, carbon (C) compounds, including their combinations with noble metals [58, 59], are of great importance. In particular, this includes long linear carbon chains LLCC [60], which exhibit unique properties. These structures form, for instance, when LLCCs are fixed at the edges between atoms of noble metals, such as two gold (Au) and/or silver (Ag) atoms, and they are stable. This involves actual phase transitions to a new allotrope form of carbon [4, 61].

A separate issue is the creation of metasurfaces based on such LLCCs (sp-electron configuration) [62] when they are deposited on the surface of a solid substrate by methods such as spraying-jet [57, 60].

In all cases, both cumulene bonds ($=C=C=C$)_n with a bond energy of 0.41 eV and polyynes bonds ($-C\equiv C-$)_n with a bond energy of 1 eV can arise, stabilized by a 1D structure; in our case, with noble metal atoms at their ends. These objects are particularly important for practical applications in conditions of spatial orientation in external fields [63].

In our work [64], we experimentally observed a sharp nonlinear increase in the magnitude of the electric current – by tens of times – compared to the value according to Ohm's law in such a compound (Au–C–Au): in a thin film with a thickness of 30 nm, for an applied external voltage of 1.5 V, the current was 0.5 A. This LLCC object was synthesized in a two-stage laser experiment [12, 13, 58, 60]: first, using laser ablation of a shungite sample to obtain a colloidal system with nanostructures, and then through laser deposition (considering fragmentation effects) from the colloid onto a solid substrate. The formation of LLCC objects was monitored using luminescence spectra and Raman spectroscopy. This effectively implemented a 4D technology for synthesizing such objects, where besides the three spatial parameters of the structures, the fourth parameter – time – was crucial, related to both the experimental fixation of the exposure time of the used system and the chosen duration of the laser radiation exposure (cf. [65]).

In the latter case, for example, nonequilibrium phase transitions of a certain type occur under

femtosecond light pulses, leading to the formation of structures with different dimensionalities [12, 65–68].

In our work, an experiment on the laser fragmentation of colloidal systems consisting of amorphous carbon was conducted under an applied external electric field of low intensity (voltage of 12 V with a distance of 3 mm between electrode microcontacts). In this case, strong polarization of the formed carbon molecules was observed, leading to the formation of extended wires when deposited on a substrate. Although these were not isolated wires but rather a tangle of these wires, their preferential growth (1D structure) still manifested in one direction along the field.

We modeled this process of geometric nematicity in the approximation of not a gaseous atomic carbon system, but an ensemble of forming C₂ and C₄ molecules – i.e., when we have 2 or 4 carbon atoms in the form of one linear molecular structure, as confirmed by luminescence and Raman spectra measurements. The final structures have spectra with maxima characteristic of objects with carbon chain lengths from 8 to 24 carbon atoms, as registered by transmission electron microscopy.

Figure 10 shows images of carbon structures obtained using transmission electron microscopy (TEM) (dark lines) under different scanning conditions at a laser beam speed v , depositing nanoparticles from the colloid onto the synthesized system on a dielectric quartz substrate with a fixed direction of the applied external electric field \vec{E}_0 .

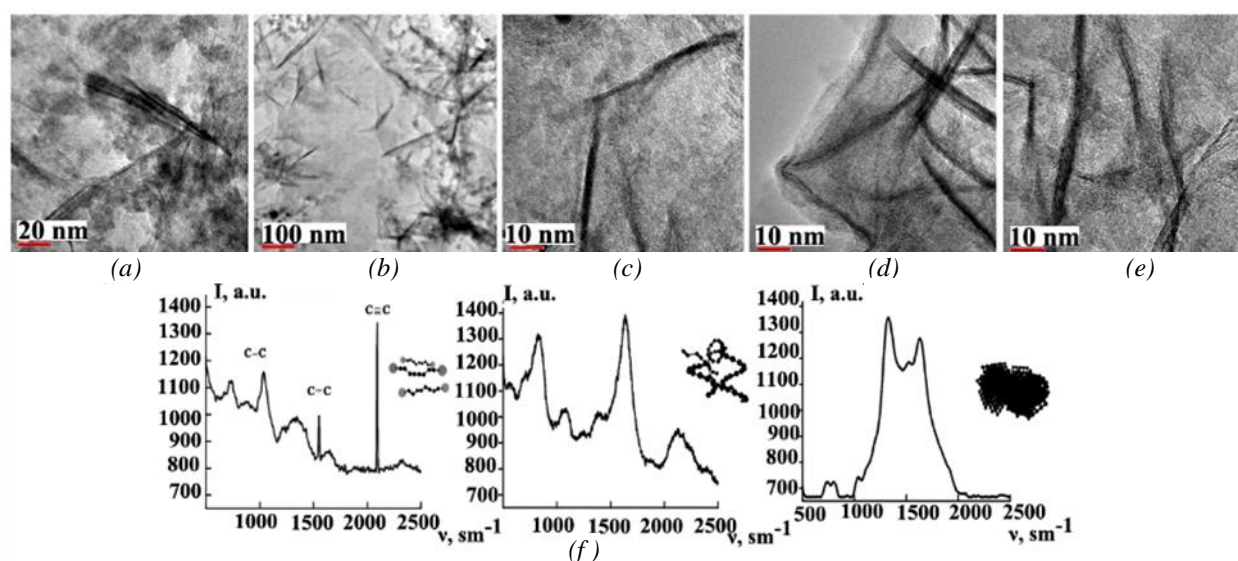


Fig. 10. TEM images of carbon LLCC structures at different scanning speeds v of the depositing laser beam and with a fixed direction of the applied external electric field \vec{E}_0 :

$v = 0.2 \text{ mm}\cdot\text{s}^{-1}$ (a), $v = 0.4 \text{ mm}\cdot\text{s}^{-1}$ (b), $v = 0.6 \text{ mm}\cdot\text{s}^{-1}$ (c), $v = 0.8 \text{ mm}\cdot\text{s}^{-1}$ (d), $v = 1 \text{ mm}\cdot\text{s}^{-1}$ (e). Modification of Raman spectra of different types of carbon structures in the colloid from which they are deposited onto the solid surface (f)

Although this LLCC ensemble structure generally only demonstrates 1D-directional dominance fragmentarily, it can manifest with bends and curves, as well as twists into certain configurations with bundles – so-called sponges (see below, Fig. 17). However, their spectral characteristics allow these objects to be identified as LLCCs (see [4]).

Thus, the existing inhomogeneities in the samples are not static objects but can change dynamically during the processes occurring at different scanning speeds of the laser beam across the object.

It should be noted that cracks may also appear on the substrate surface with the forming carbon structure for various reasons. Their development dynamics – exemplified by spontaneous healing – is discussed in the following section 3.3.

3.3. The process of crack self-healing

In the presence of an inhomogeneous cracked structure, the process of self-healing of existing inhomogeneities may occur under dynamic object movement conditions. This is modeled within the framework of the mechanism of particle self-diffusion.

Figure 11 presents a DLA model for the case of crack healing from three sides, with varying adhesion probability (s). This effect can be considered as the healing of crack ends.

Figure 12 presents a DLA model for the case of crack healing from two sides with varying adhesion probability (s). This effect can be viewed as healing from the center of the crack.

Figure 13 presents a DLA model for the case of crack healing from one side.

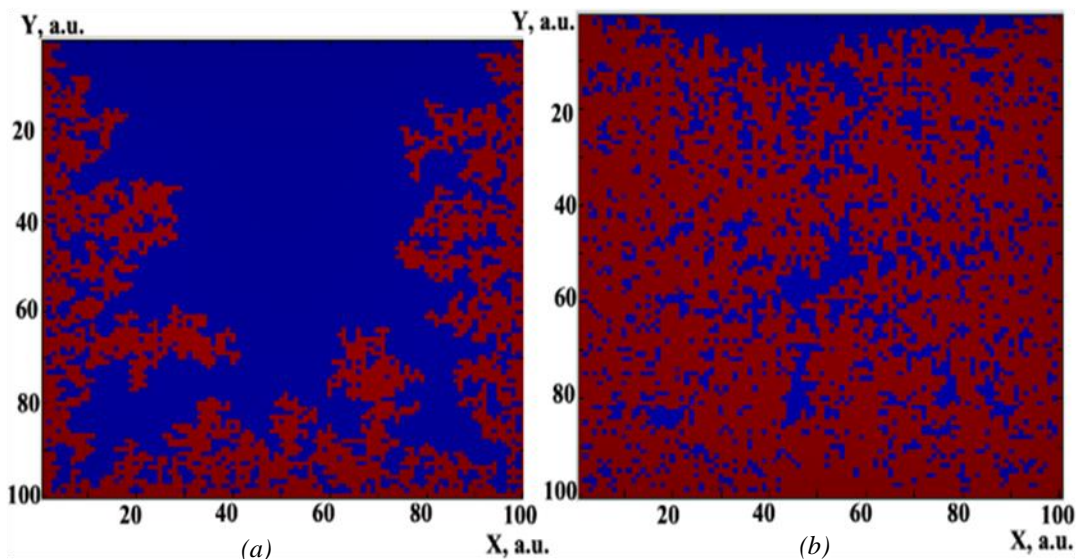


Fig. 11. Model of crack healing from three sides with varying adhesion probability (s): $s = 0.1$ (a); $s = 0.3$ (b)

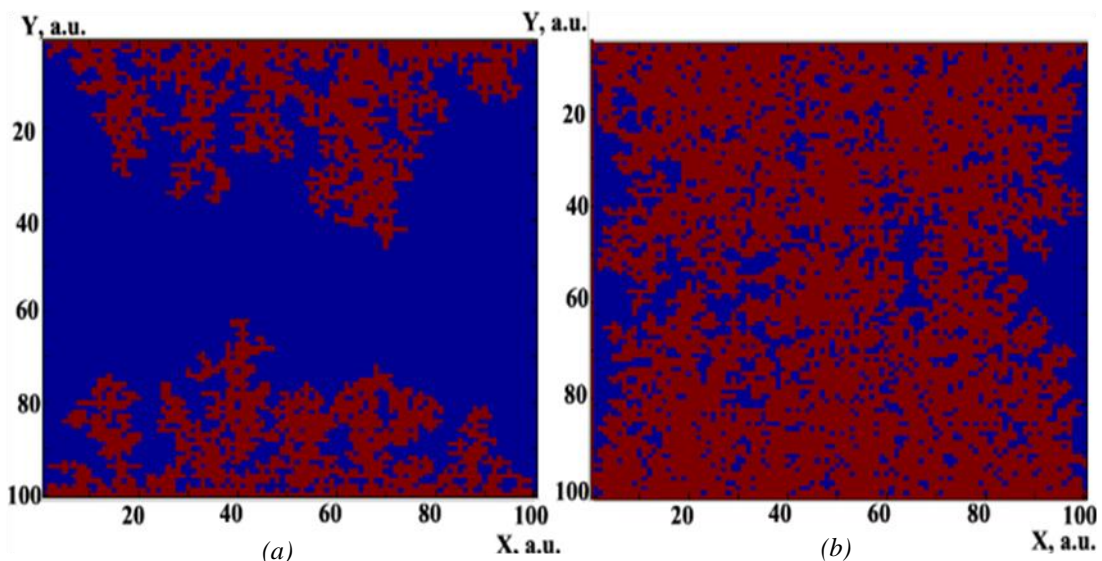


Fig. 12. Model of crack healing from two sides with varying adhesion probability (s): $s = 0.1$ (a); $s = 0.3$ (b)

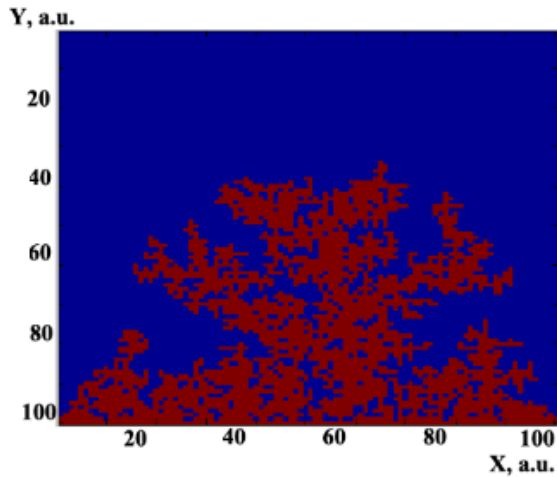


Fig. 13. Model of crack healing from one side at $s = 0.1$

Let us consider two physical models of such crack healing.

Deposition model. In the proposed models (see Appendix P.2), the computational domain is represented as a rectangular grid with dimensions $M \times L$, and particles are deposited along the vertical direction onto the previously formed structure according to specified rules, adhering to the nodes of the square grid. Over time, this process forms a cluster or aggregate with a specific geometry [69, 70].

Figure 14 shows the simulated profile from a side section of the crack, illustrating the boundaries where it contacts the surrounding material. Two crack healing structures $h(i)$ with a height of 250 a. u. over time $T = 100$ a. u. are shown, with a deposition rate of 100 (Fig. 14a) and 200 (Fig. 14b) particles per unit time (per second) within the framework of the ballistic deposition model.

A similar image is shown in Fig. 15 for another model – random deposition.

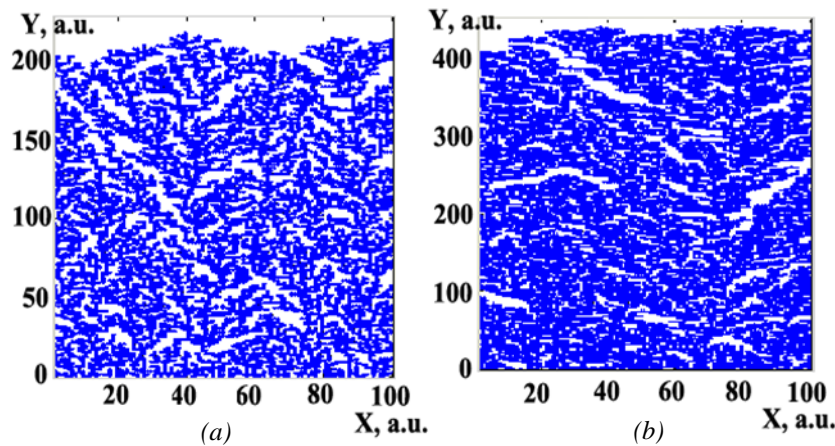


Fig. 14. Profile of the structure formed during crack healing within the ballistic deposition model at a deposition rate of 100 particles/s (a) and 200 particles/s (b)

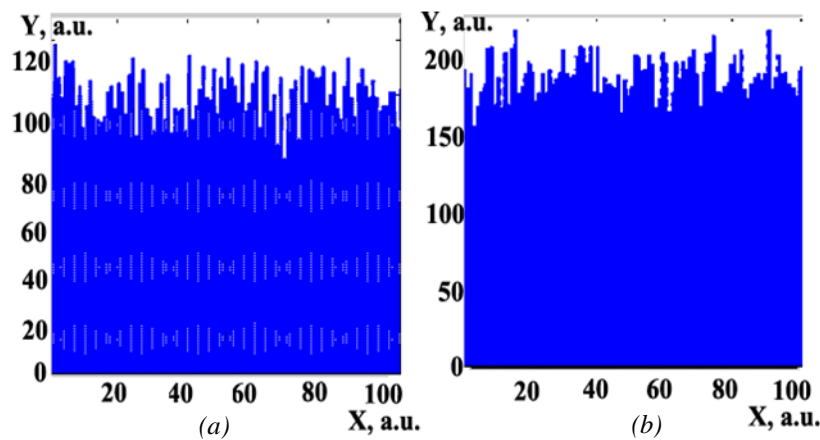


Fig. 15. Profile of the structure formed during crack healing within the random deposition model at a deposition rate of 100 particles/s (a) and 200 particles/s (b)

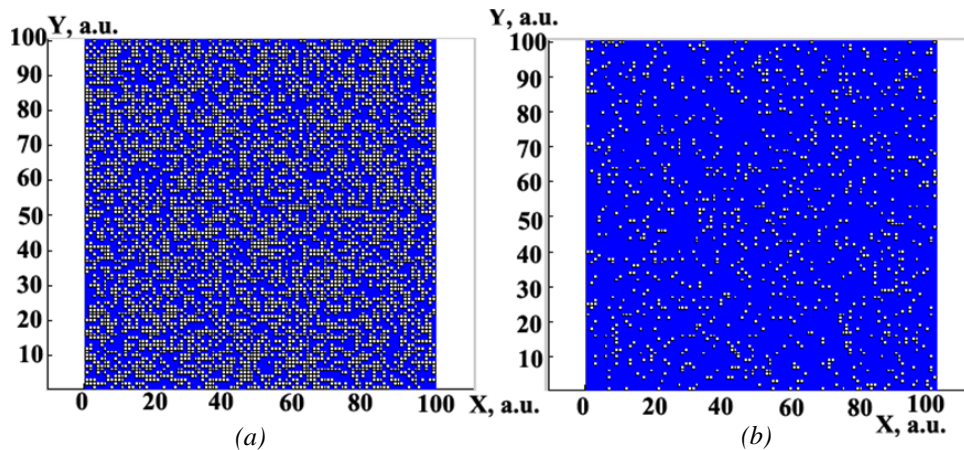


Fig. 16. Profile of the structure formed during crack healing within the cellular percolation model at $s = 0.5$ (a) and $s = 0.9$ (b) on a plane (in a. u. along the axes)

Percolation model. In this model, the crack is represented as an aggregate of defects. The process of particles seeping into the crack from the material is considered within the percolation approximation (cf. [71]).

Figure 16 shows a simulated profile (side section) of the structure formed during crack healing within the framework of the cellular percolation model, with variations in the percolation threshold, which is determined by the value of s .

3.4. Diffusion model of the structure of C–Au atoms in microsponge objects

As previously discussed, one of the convenient and straightforward methods for synthesizing carbon microstructures is laser deposition from a colloidal solution containing both carbon chains and noble metal nanoparticles, which act as catalysts for the synthesis. Using this method, we obtained experimental samples that were used to develop a structural model and evaluate its adequacy. The carbon microthread system (microsponge) samples were synthesized by laser exposure, using a ytterbium laser, on a colloidal system containing carbon chains (C) and gold nanoparticles (Au) in the presence of an external electric field (Fig. 17) [72].

Analysis of the conditions and results of the experimental synthesis led to the conclusion that the process influencing the shape of the sponge had a thermodiffusion nature. The investigation of the thread system's shape revealed its branched nature, characteristic of dendritic objects formed by diffusion processes. The sponge's shape was elongated in the direction of the electric field lines in the medium. This observation served as the criterion for selecting the appropriate modeling approach.

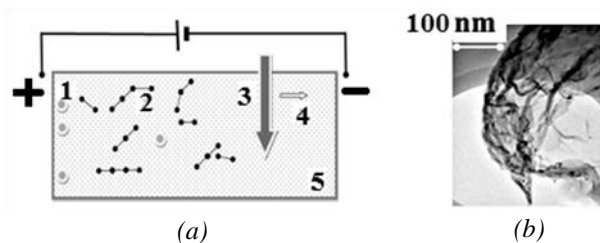


Fig. 17. Synthesis scheme and results: experimental setup with an external electric field (a): 1 – Au nanoparticles; 2 – C chains; 3 – direction of laser radiation exposure; 4 – direction of laser beam movement; 5 – cuvette with colloidal solution; (b) – obtained optical image of the C–Au sponge

Thus, the model (see Appendix P.3) was chosen within the framework of the diffusion approximation, based on the particle diffusion equation. The model equation was solved in a discrete form using the DLA approximation [62] through an iterative process [73, 74].

The proposed model was implemented in MATLAB using a.u. Calculations of the sponge structure were performed according to this approximation, followed by a comparison with experimental samples. In the model calculations, three types of C chains were generated: objects of length 2 a. u. were introduced into the computational domain with a probability of 70 %; length 4 a.u. with a probability of 20 %; and length 5 a. u. with a probability of 10 %. Their orientation was also specified – 90 % of the chains were vertical, and 10 % were horizontal. Figure 18 shows the model of a C–Au sponge branch for a computational domain of 300×300 a. u. with the specified parameters, as well as the variation in sticking probability s from 0.1 to 0.2 a. u. when a single Au particle is placed at the bottom boundary of the computational domain.

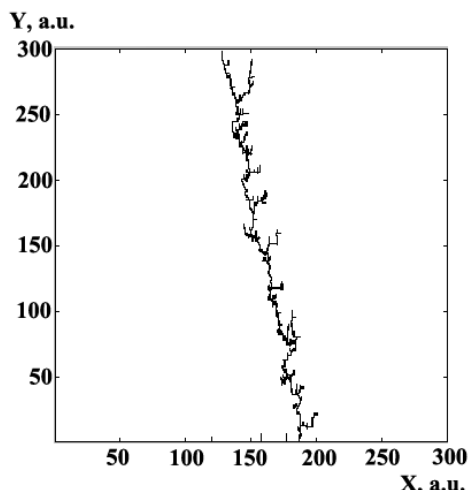


Fig. 18. Model of a C–Au sponge branch (explanations provided in the text)

The self-assembly of metal-carbon nanosponge structures was carried out by us in colloidal solutions under the influence of laser radiation and an external electric field (cf. [72]). The samples obtained in the experiments had a structure consisting of an array of nanothreads forming a sponge with micro/nano fragments, as shown in Fig. 17*b*.

Figure 19 shows a fragment of the formed random sponge structure with a system of nanothreads ranging in size from 2 to 300 μm .

Figure 20 presents a model image of a microfiber system forming a microsponge with a thread width of about 100 nm, varying the length and number of microthreads. In Figure 20*a*, the model shows short threads forming a rounded shape with a distinct small central area and long branches; 50 threads were generated for this formation. Figure 20*b* depicts a model of a sponge made of medium-length threads. The resulting figure, composed of 150 threads, is more uniform with a well-filled center and a larger area; the shape is approaching rectangular.

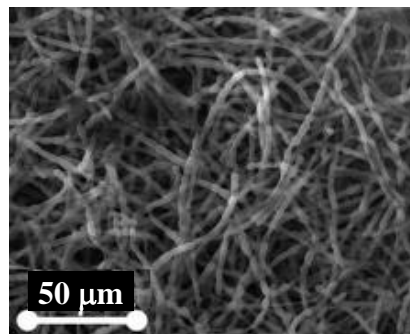


Fig. 19. Optical image of a fragment of the microsponge, part of the entire sponge shown in Fig. 17

Figure 20*c* shows an image of a sponge made of 300 threads – a rectangular shape without a distinct center and with short branches.

The simulation results qualitatively match the experimental results (Figs. 17*b*, 19).

As a model for describing individual threads in the microsponge, the Monte Carlo method [75] was considered. In this approach, objects of various sizes were introduced into the computational domain, where they made random movements and combined with a given probability. The combination of objects was considered within the framework of the Moore neighborhood (see Appendix P.4).

This approach may be useful for a first approximation in describing the experimental samples of C–Au microsponge formation.

3.5. Computer simulation of helicoidal microstructures

Helicoidal multilayer microstructures made of different materials are of interest in the context of digital materials science models due to their unique physical and functional properties (see, for example [76]).

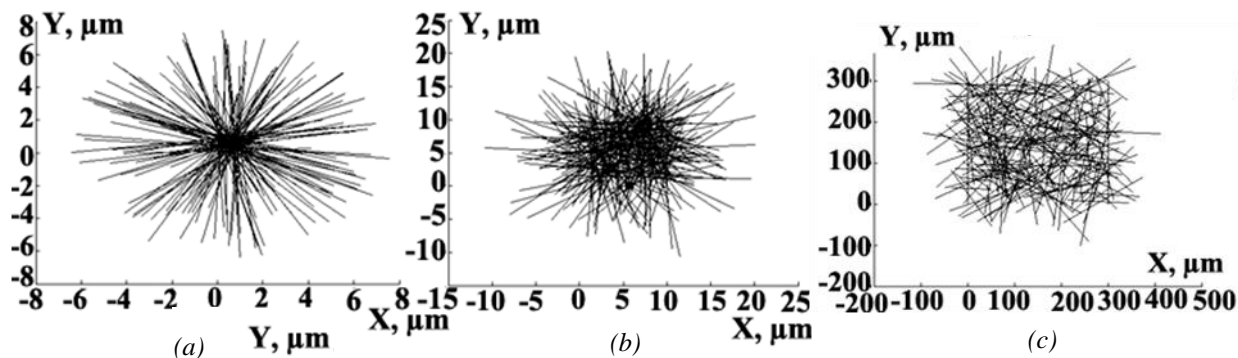


Fig. 20. Microsponge model with different thread lengths: 1–20 μm (a); 10–50 μm (b); 50–300 μm (c)

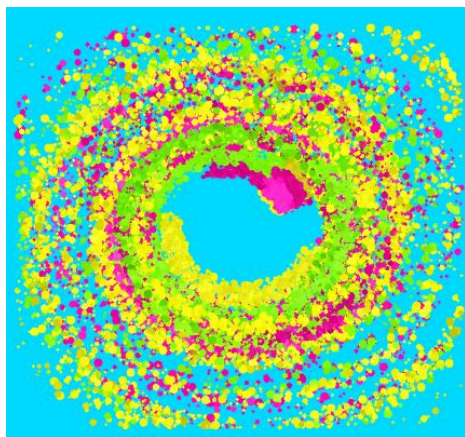


Fig. 21. Model of a helicoidal structure

The corresponding model (see Appendix P.5), which allows for the description of the structure of such objects, can be approximated as a random spiral [77]. This type of object is formed from a system of random spirals. These figures have randomly positioned centers and random radii r of the coils. They consist of points arranged along a spiral, considering random current rotation angles θ , with

their coordinates defined by simple expressions: $r = r(\theta)$; $x = r \cos(\theta)$; $y = r \sin(\theta)$ [78].

Figure 21 shows an image of such a random spiral structure formed by a system of rounded objects.

A diffusion model based on a cellular automaton was implemented in MATLAB on a square computational domain with a side length of 450 a. u. The probability of a cell being occupied was assumed to be 0.5, which, in the context of this helicoidal symmetry, corresponded to the presence of an external magnetic field in the experiment. We considered a magnetic field strength of 100 Oersted (cf. [79]).

Calculations of the resulting helicoidal structures were performed using the proposed model. To account for their formation, a spiral was considered as the initial structure from which growth occurred to produce helicoidal objects. The shape of the elements forming the structure was varied in the calculation. The final figure was composed of single elements forming horizontal, vertical, and diagonal chains; for specificity, these chains were made of two and four elements (Fig. 22).

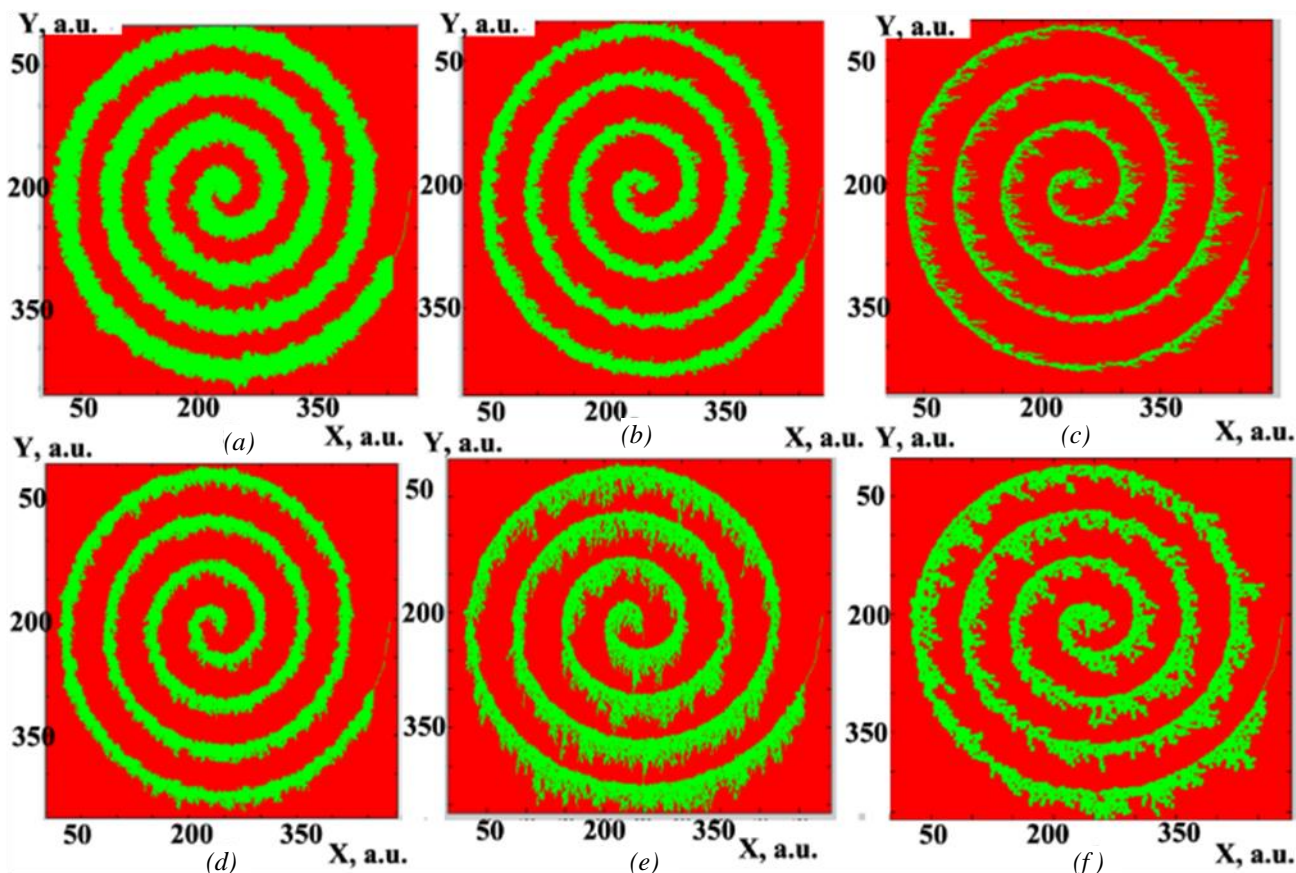


Fig. 22. Models of helicoidal structures: for initial horizontal fractal segments composed of elements with a unit length of 1 (a), as well as lengths of 2 (b) and 4 (c). For initial vertical lines: lengths of 2 (d) and 4 (e). For diagonal lines: length of 4 (f)

The modeling procedure discussed for such systems is quite versatile and could serve as an additional approach to 1D structures in various systems with a fixed nematic configuration.

4. Metal-carbon structures on a solid surface – a system of carbon nanotubes with gold atoms

In our experiment, we successfully achieved the sintering of carbon nanotubes with gold atoms using a modified form of graphite, shungite, followed by the creation of thin-layer structures on a solid surface. The sintering was conducted in a liquid environment where shungite powder was intensely mixed with a colloidal gold solution under the influence of ultrasound. The resulting system was then irradiated with laser radiation to deposit it onto a solid substrate. A series of TEM images is shown in Fig. 23.

A simulation model within the framework of the DLA approach can be used to describe this metal-carbon nanotube structure. Analysis of the transmission electron microscope images indicates that the synthesized nanotubes have a curved shape. Structures with this shape can be synthesized using a random walk model due to diffusion on the plane through random changes in the coordinates (x, y) of the moving model particles on the plane.

$$x_n = x_0 + \sum_{i=1}^n \gamma_i; \quad y_n = y_0 + \sum_{i=1}^n \delta_i,$$

where x_0, y_0 are the coordinates of the starting point of the diffusion walk, γ and δ are the horizontal and vertical steps, respectively, and n is the number of steps. The movement of a single model particle generates an individual nanotube.

In the central part of the simulation area, the effect of a laser beam with a specified relative

diameter $r = \mu d$ was modeled, where μ is the scaling factor, and d is the diameter of the model particle. Then, outside the laser-affected area, the relationship was evaluated as:

$$\gamma_i = \delta_i = \sqrt{2D\tau} r_n \Delta_c,$$

where $D = \frac{k_b T}{3\pi\epsilon d}$, D is the diffusion coefficient, k_b is

the Boltzmann constant, ϵ is the dynamic viscosity, T is the temperature, τ is the time step, r_n is a normally distributed random number, and Δ_c is the step reduction factor: $\Delta_c = 1/r_c$, where r_c is a random integer from the interval $[1, N_c]$, and $[1, N_c]$ is the number of modeled nanotubes.

In the laser-affected area, the step length for both the horizontal and vertical directions was evaluated as $\alpha\gamma_i$ and $\alpha\delta_i$ respectively, where $\alpha > 1$ is the coefficient describing the acceleration of the model particle due to laser exposure.

Figure 24a shows an image of a model structure of a bundle of nanotubes deposited from an aqueous colloidal solution. Figure 24b provides an assessment of the lengths of the formed structures.

Electrophysical Characteristics. Current-voltage characteristics (IV curves) were measured using a four-probe setup [81] with an RT-70V device in a simple configuration, where the colloid we produced was deposited onto an aluminum target. Measurements were conducted in two modes: (1) “contact” mode, where one probe is in contact with the surface of the substrate and the second probe is on the deposited layer, and (2) «tunnel» contact mode, where the second probe is lifted a small distance (approximately 0.1 nm) above the surface. This setup is typical for a Schottky diode, meaning we have an n -type semiconductor layer on top of a metal layer.

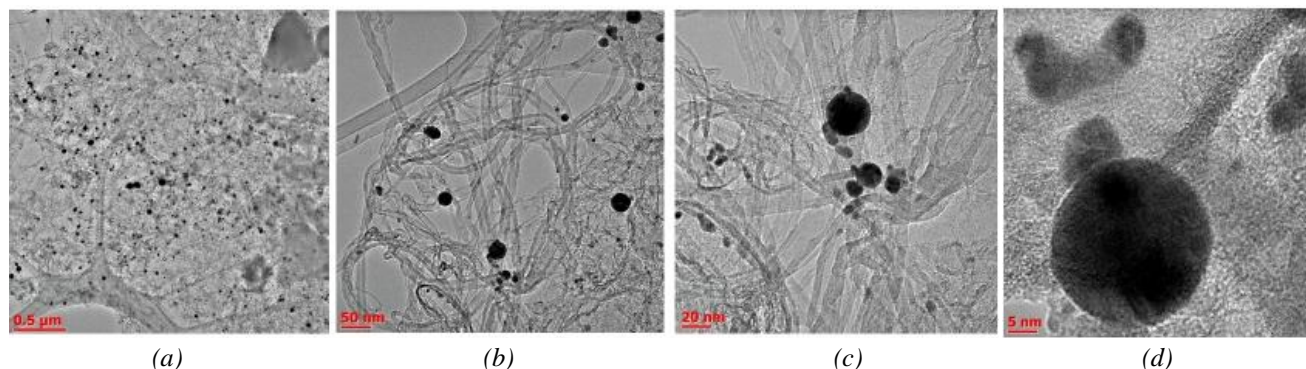


Fig. 23. TEM images of a thin-film system of carbon nanotubes (elongated strands) with gold atoms (dark clustered inclusions) on a solid-state quartz substrate with shungite (general background).

Images *a–d* correspond to different magnifications in the TEM

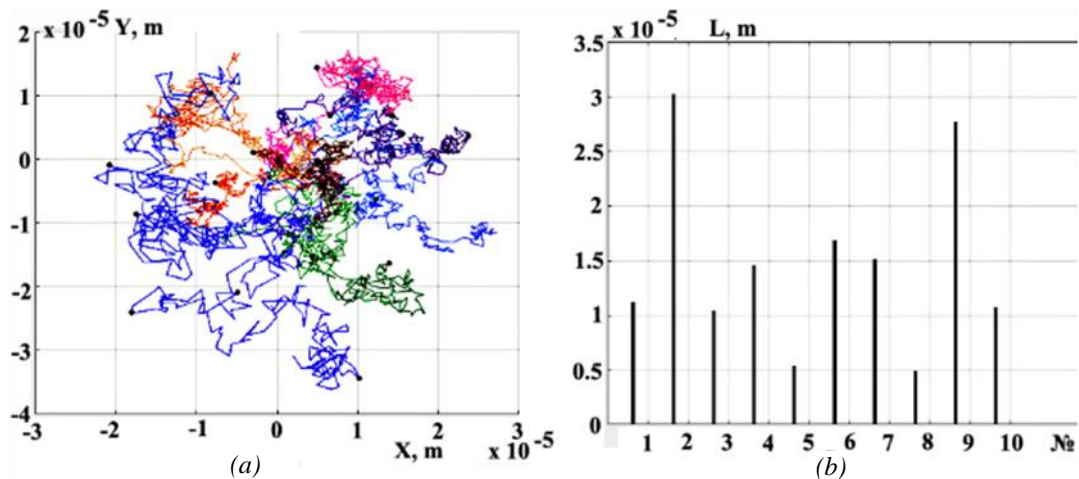


Fig. 24. Model of a nanotube bundle: the structure consists of 10 nanotubes, with model gold atoms marked by dots (a); histogram of the length distribution of the model nanotubes, where N is the nanotube number (b)

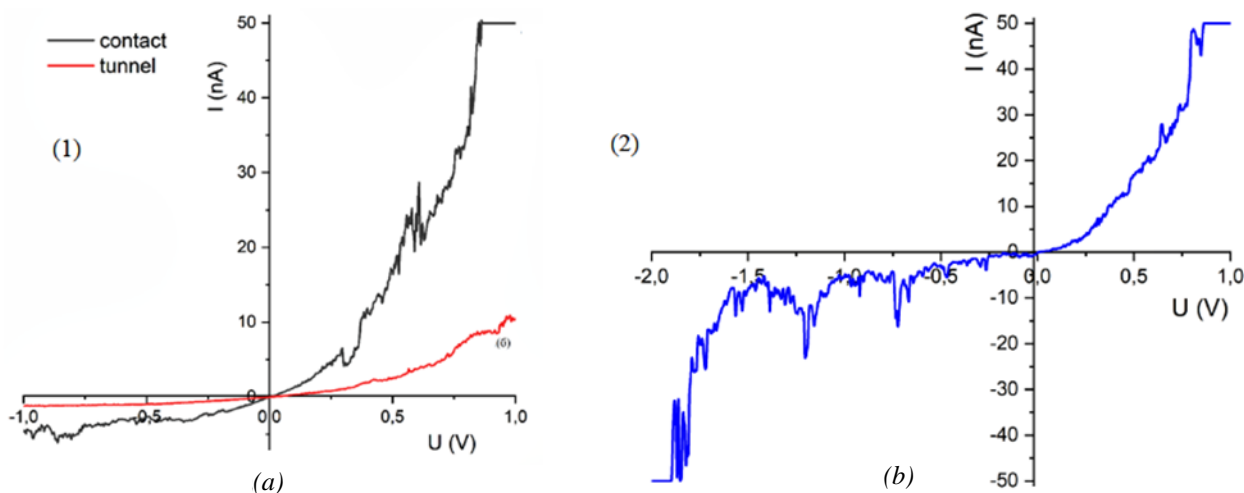


Fig. 25. (1) IV characteristics – the dependence for the two measurement configurations (see text): a – contact; b – tunnel; (2) – IV characteristics with a change in the polarity of the applied microcontacts

The voltage range parameters were $[-1; 1]$ V, chosen because, for metal IV characteristics in this range, the behavior should remain linear. This holds true for both the contact scheme and the tunnel mode. The system was not driven to the breakdown state during reverse current measurements. The IV curves obtained for one of the samples in the two configurations mentioned are shown in Fig. 25. A significantly nonlinear behavior is observed in the IV curves. This non-ohmic behavior is fundamentally important in the development and creation of electronic systems of the trigger type using metal-carbon nanocomposites.

The increase in the effect generally depended on the topological features of the formed nanostructures – specifically, the number of dendrites/fractals, as well as the degree of their filling and connectivity within the entire system. Conductivity increased when a greater number of clusters formed in the

longitudinal direction compared to the transverse direction. This fact influences the magnitude of the current jump shown in Fig. 25.

It was also found that the type of topology formed in the laser setup can be controlled and predetermined. This capability is determined by the selected characteristics of the laser radiation – such as power, beam diameter, scanning speed across the surface, and exposure time to the system. Additionally, in the structures we obtained, conductivity increased with rising temperature T according to the following relationship:

$$\sigma \sim \frac{1}{\exp(\varphi/kT)}$$

where k is the Boltzmann constant and φ is the activation energy of conductivity [17].

The dependencies obtained require separate, detailed consideration, taking into account various

factors, including the complex sintering process, where different adsorption effects on the gold atoms must be considered. These effects alter their electrophysical and physicochemical properties, including binding energy, adhesion probabilities, thermally activated efficiency, and other parameters. We will note only a few distinctive characteristics observed in the obtained dependencies (cf. [3, 34]).

First, the presence of regions with zero conductivity may indicate the emergence of a bandgap similar to that in semiconductors, meaning that in such structures, the gold atoms undergo a transition from metallic conductivity to semiconducting behavior. This is a non-trivial process.

Second, the observed jumps in measured tunneling conductivity suggest the influence of topological factors, particularly the emergence of excess charge states on the surface of nanostructures depending on their shape and size. Here, processes such as resonant electron transitions at contacts of different polarity and mutual polarization effects between neighboring nanoparticles and their surroundings may play a decisive role. This alters the characteristics of the thermally activated effects responsible for the sample's conductivity.

The physics of isolated gold nanoparticles combined with carbon nanotubes, especially in a thin-film structure with shungite, represents one of the promising areas in modern topological electrophysics of metal-carbon composites, with applications in various nanoelectronics tasks. Even more interesting are the fractal structures synthesized in the laser experiment, which can be controllably implemented.

In this context, it is useful to briefly consider a model of electric field enhancement on fractal structures, such as those shown in Fig. 3, which, in the simplest model representation, consist of elements in the form of long branches with fractal segments at their ends. The electric field intensity at the tip of an individual fractal structure can be expressed as

$$E(r) = \frac{1}{4\pi\epsilon_0} \frac{q}{R^3} r,$$

where R is the radius of the tip. Let's assume the tip can be approximated by a sphere with such a radius R . Then, the field intensity at the tip is estimated as

$E_b(R) \sim \frac{1}{R^2}$. Regarding the enhancement G at the end of an isolated tip, it can be calculated using the ratio $G = E_b/E_f$, where $E_f \sim \frac{1}{R_f^2}$, and R_f is the radius

of the minimum coverage circle in the calculation procedure used. In experiments, this corresponds to natural averaging over a spatial area on the sample's surface when measuring the electrophysical parameters in each local area using a microcontact with a certain finite cross-section (which determines the technical limitation on the local measurement accuracy).

To estimate the relative enhancement in structures like those in Fig. 3, within the considered framework, it is necessary to adopt a numerical model of the fractal object with specific characteristics. Our analysis shows that effective enhancement can be achieved for the following structural features of the fractal with the parameters: the relative diameter of the minimum coverage circle should be, in arbitrary units, 16 a. u., for example, with the fractal object having 8 long branches, 34 ends, and an average tip radius of 0.5 a. u. Then, the localized conditional enhancement at the end of an individual long branch would theoretically be 256, while the total integral enhancement over the calculation area, as measured in the experiment with the finite coverage area of the structure, is estimated to increase the electric field strength by 5 orders of magnitude (for the specified parameters, this amounts to $8.7 \cdot 10^4$).

Thus, we have demonstrated that in model samples, within the proposed approximation, it is possible to achieve relative enhancement of the electric field by several orders of magnitude, considering the entire perimeter of the branched fractal figure within a specific coverage area when measured with a microcontact. This effect is similar to the well-known phenomenon of giant Raman scattering (SERS) enhancement on rough surfaces, used, in particular, for detecting extremely low concentrations of dyes on such surfaces (cf. [4, 8, 9, 15, 80]).

5. Laser ablation of diamond surfaces and defect structures in them

Carbon composites, similar to systems with carbon nanotubes, can also include diamond-like materials, in which graphitization processes occur, determining their electrophysical characteristics. Absorption spectra for different carbon materials are well known and are shown in Fig. 26 [81]. As seen, diamond exhibits a narrow absorption peak around 200 nm compared to other diamond-like forms shown in the same figure.

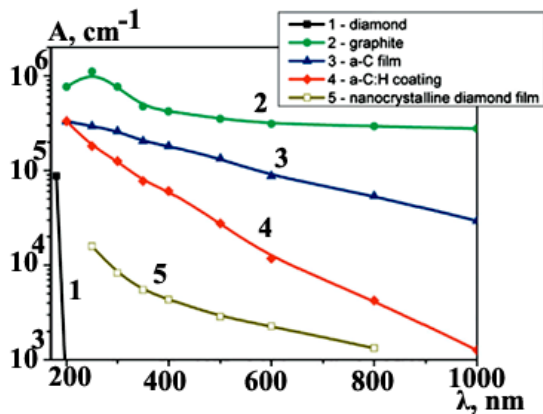


Fig. 26. Dependence of the optical absorption coefficient (A , in cm^{-1}) on the wavelength of laser radiation λ (in nm) for various carbon nanomaterials. The peak around 200 nm corresponds to diamond

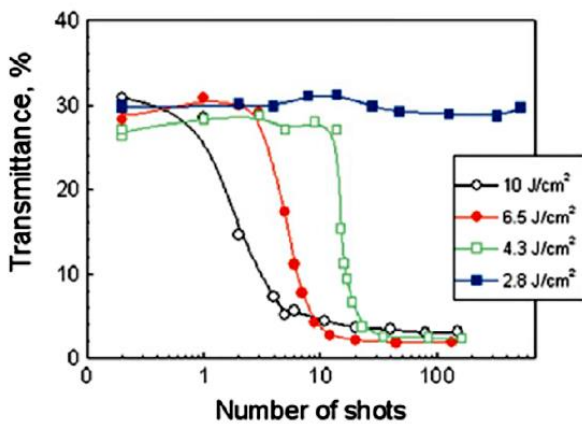


Fig. 27. Dependence of the optical transmittance coefficient of diamond on the energy density of laser irradiation and the number of laser pulses applied

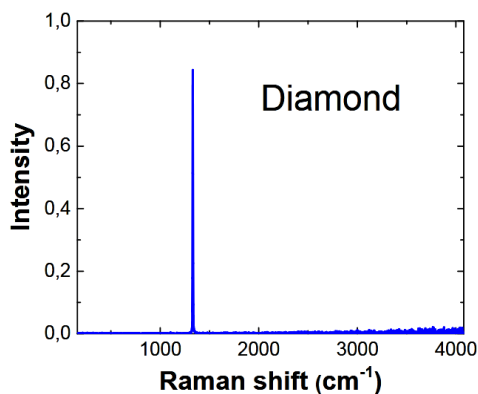


Fig. 28. Raman scattering spectrum for the surface of a diamond sample after laser ablation with graphitization of the irradiated area

For diamond, under the influence of picosecond-duration pulsed laser radiation, its transmittance is highly dependent on the laser irradiation mode (number of pulses, energy density) – Fig. 27 [81].

It can be seen that at high laser energy densities, the transmittance coefficient sharply decreases even with a small number of irradiation pulses.

This effect is associated with the graphitization of diamond, which is confirmed by the Raman scattering spectrum shown in Fig. 28, following surface laser ablation of the diamond sample [82].

The thermally induced phase transformation process from diamond to graphite begins at the surface and gradually spreads deeper into the diamond crystal. Using pulsed laser irradiation [83–86] allows the localization of the diamond-to-graphite transformation process within a submicron region, which can be moved inside the crystal in any desired direction by appropriately focusing the laser beam within the diamond sample. Ultimately, this technology enables the creation of three-dimensional conductive microstructures of various shapes within the diamond volume.

To assess the accuracy of the modeling, it is easy to compare the fractal dimensions in the images of models with those in real samples using the methodology described in Section 2.

The proposed model for analyzing the graphitization process during the development of a diffusion process, considered within the framework of a cellular automaton algorithm, allows for an evaluation of the influence of experimental laser synthesis control parameters on the graphitization effect in diamond. The connection between the model and these experimental parameters arises through the value of the occupancy probability (s) of a cell in the calculation area as a function of the relative temperature. For example, studies of the structure of graphitized areas obtained through pulsed laser exposure indicate that one of the controlling parameters is pulse duration, an increase of which leads to an increase in the critical speed of the laser beam focus movement within the sample. This effect is accompanied by the appearance of discontinuities.

Figure 29 shows models of graphitization areas constructed based on the diffusion model, where the graphitization area began to spread from different starting objects: from a straight line (Fig. 29a); from a system of points (Fig. 29b); from a system of fractal cracks (Fig. 29c), constructed using DLA approximation (Fig. 29d – final structure). In the center of the calculation area for Figs. 29a and 29b, the occupancy probability s (which determined the growth of the graphitization structure) was set to be twice as high as in other parts. This allowed for the creation of structures with a predetermined growth direction.

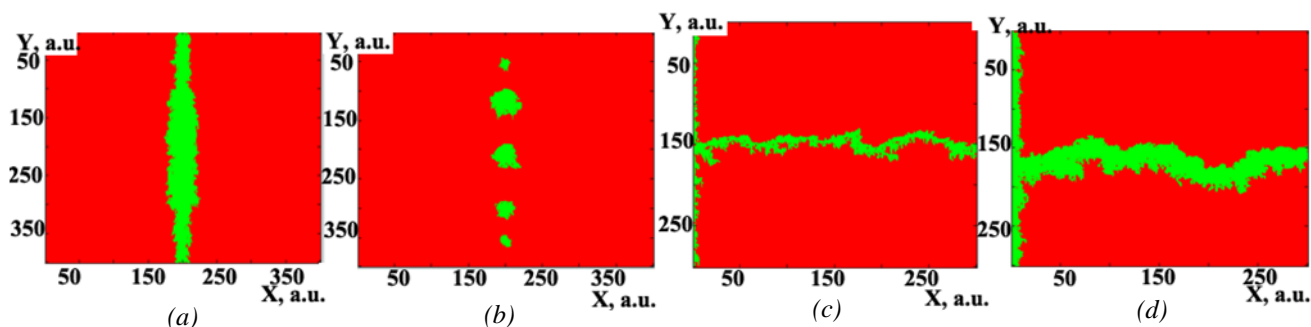


Fig. 29. Simulation results of the graphitized area for different initial structures with an occupancy probability of $s = 0.0073$: a straight line (a); a system of points (b); DLA model of a fractal crack system (c); the final structure of the graphitized area corresponding to the initial fractal crack system (d)

Similar but more branched and heterogeneous structures can also be generated within the DLA model. Figure 30 shows such models considering various initial conditions. The implementation of random walks during the iterative process in the DLA model allows the generation of structures with a more pronounced desired growth direction. For example, the models shown in Fig. 30 exhibit predominant growth toward the right.

In addition to surface laser ablation of diamond crystals, bulk transformation in a laser field is also possible [85, 87, 84]. These 3D microstructures within the diamond can naturally be created by moving the sample through the focus of the laser beam (see [86]). Raman microspectroscopy has shown that the laser-modified material is a mixture of amorphous and graphitic structures. This is further confirmed by the measurement of the electrical conductivity of such samples [88].

However, a complete transformation of bulk sp^3 -diamond into sp^2 -carbon structure, during this laser-induced phase transition, is hindered by the emergence of compressive and tensile stresses due to the significant density difference between these two allotropes of carbon. As a result, the resulting electrically conductive structures typically consist of numerous micro- and nanoscale sp^2 -carbon inclusions within a sp^3 -diamond matrix. According to [88], this occurs via a percolation mechanism.

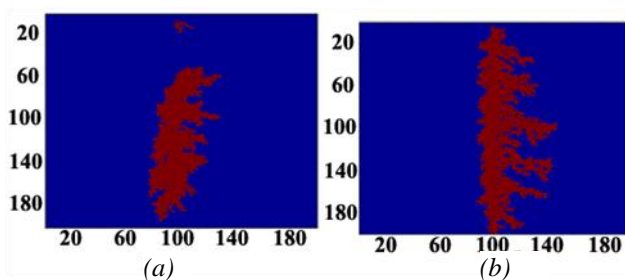


Fig. 30. DLA model results of the graphitized area for different initial structures with $s = 0.1$: two regions (a); a straight line (b)

Furthermore, one of the allotropic modifications of diamond is the natural mineral lonsdaleite (hexagonal diamond). For a long time, it was believed that lonsdaleite, which has also been synthesized artificially, could only exist in diamonds as defects and twins [89]. However, this involves different twinning mechanisms, particularly the shifting and displacement of layers in the martensitic class.

Indeed, it has been found that the crystal structure of lonsdaleite is hexagonal with lattice parameters $a = 2.52 \text{ \AA}$, $c = 4.12 \text{ \AA}$ [89]. The difference between diamond and lonsdaleite lies in the packing sequence of the layers. The diamond crystal lattice (denoted as 3C) has a layer sequence indexed by the crystal lattice elements ABCABC [89], while the lonsdaleite crystal lattice (denoted as 2H) has a layer sequence of ABAB. Packing defects that arise in the diamond lattice during growth contain lonsdaleite interlayers. The theoretical density of lonsdaleite is the same as that of diamond ($3.51 \text{ g}\cdot\text{cm}^{-3}$).

Figure 31 shows a fragment of a diamond crystal containing numerous defects [89], with the zone axis [110] visible. Two systems of $\{111\}$ planes with an interplanar distance of 0.206 nm can be seen. The characteristic planes (1-11) and (1-1-1) of diamond form a 70° angle. Dashed black lines indicate structural changes caused by packing defects. Additionally, incoherent twin boundaries are marked with asterisks in Fig. 31. The difference between such boundaries and traditional twins is the lack of a clear boundary, instead displaying broken lines marked with asterisks. Rectangles denote fragments of the diamond sample with a lonsdaleite lattice. The rectangular fragments of lonsdaleite are rotated by 70° . In such a structure, they could be formed through a twinning mechanism via mirror reflection from a plane symmetrically located between adjacent $\{111\}$ planes in the diamond crystal. Considering the [110] zone axis as the mirror reflection plane, it could be

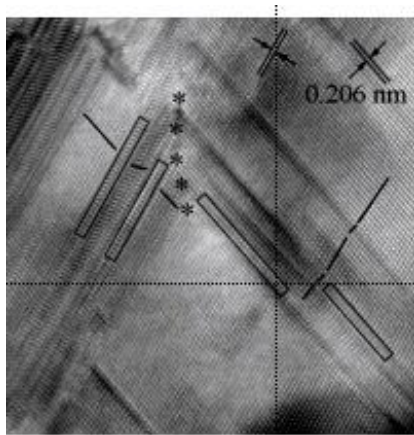


Fig. 31. Structure of Diamond-Lonsdaleite

the (3-308) plane in hexagonal close-packed (HCP) coordinates, which corresponds to (101) or (-3304) in face-centered cubic (FCC) coordinates. Indeed, they belong to the [110] HCP zone axis and form angles of 35.30° and 35.25° with (001)-HCP and (-3302)-FCC, respectively. The established twinning planes (3-308) HCP and (-3304) HCP are typically not characteristic of crystals with an HCP lattice structure.

The zone axis [110] is shown. Two systems of {111} planes are visible with an interplanar distance of 0.206 nm. Dashed black lines indicate changes in structure caused by packing defects. Rectangles denote fragments of lonsdaleite, and asterisks mark incoherent twin boundaries.

In addition to individual layers of lonsdaleite in diamond packing, relatively large lonsdaleite fragments are sometimes observed [89]. Besides lonsdaleite, 4H polytypes (repeated layers of CBCA...; known as 4H polytypes in diamond) and 6H (layer sequence ABCACB...) were also discovered.

These structures hold great promise for creating semiconductor materials with controllable electronic states and achieving specific electrophysical characteristics in various conditions.

Furthermore, during the synthesis of nanotwinned topological polycrystalline bulk materials from onion-like structures, nanodiamonds with twinned structures were obtained from isolated onion-like blocks, for which potassium chloride particles were used [90]. Under conditions of high pressure and high temperature, these were observed to transform into martensite.

Reference [90] also argues that the properties of homoepitaxial diamond films (111) are influenced by the presence of twins, as well as packing defects, impurities, and dislocations.

Thus, various diamond-like structures, especially those with twinning, represent a distinct branch of

modern diamond nanotechnology (cf. [3]). Overall, twinning theory is essential for applications; it requires both microscopic and macroscopic examination, which, however, falls outside the scope of this article.

6. Conclusion

In this partially review-based article, we examined the modeling of various topological configurations in metal-carbon nanocomposites with carbon nanotubes based on our results. The review focused on the potential of digital materials science technologies to control the electrophysical characteristics of these topologically synthesized structures in laser experiments.

These laser methods are relatively simple and inexpensive (even when using femtosecond laser irradiation that develops nonequilibrium nonlinear effects in the target) compared to traditional methods of growing nanofilms. In particular, this includes comparing laser methods with the synthesis of semiconductor compounds and hybrid porous nanomaterials, including high-entropy alloys. In laser schemes, this can be done with virtually no restrictions on composition or thickness, down to a few nanometers, unlike the conventional methods of molecular beam epitaxy and metal-organic chemical vapor deposition.

Moreover, by controlling various laser modes, it is possible not only to create topological systems of a specific configuration but also to manage undesirable processes such as aggregation, dispersion, and fragmentation of nanoclusters (which can also be influenced by temperature factors), and to control their mobility during the synthesis of nanostructures with the desired concentration of components.

Despite the initial development of non-stationary nonequilibrium processes during their formation, these objects can remain stable in terms of stabilizing quasi-equilibrium quantum states. This is due to their topological features, which, for example, lead to changes in thermophysical and thermodynamic characteristics during phase transitions, making them irreversible or at least giving them hysteresis. It is important to note that the deformation process of an object's structure (especially in crystal lattices and/or 2D structures) can be likened to the effect of magnetic fields.

The discussed effects and the possibility of controlling them with laser methods hold great promise for the development of micro-nanoelectronics elements and systems based on new physical principles. In the near future, significant experimental results are expected in this area,

including the identification of trends in the synthesis of high-temperature states in superconductivity within topological structures of different classes.

7. Funding

This research was conducted as part of the state assignment to VSU “Development of methods for surface laser modification of synthetic diamond films and wide-bandgap compositions based on it for controlling the optical and electrophysical properties of structured materials” (FZUN-2023-0003).

8. Conflict of interests

The authors declare no conflict of interest.

References

1. Kresin VZ, Ovchinnikov YuN. «Giant» strengthening of superconducting pairing in metallic nanoclusters: large enhancement of T_c and potential for room-temperature superconductivity. *Uspekhi fizicheskikh nauk = Physics-Uspekhi*. 2008;51:427-435. DOI:10.1070/PU2008v051n05ABEH006531
2. Troyan IA, Semenok DV, Ivanova AG, Kvashnin AG, et al. High-temperature superconductivity in hydrides. *Uspekhi fizicheskikh nauk = Physics-Uspekhi*. 2022;65:748-761. DOI:10.3367/UFNe.2021.05.039187
3. Trahtenberg LI, Melnikov MYa. *Metal/semiconductor containing nanocomposites*. Moscow: Tehnosfera; 2016. 624 p. (In Russ.)
4. Garnov SV, Abramov DV, Bukharov DN, Khudaiberganov TA, et al. Electrophysics of carbon 1D structures obtained in a laser experiment: models and demonstration. *Uspekhi fizicheskikh nauk = Physics-Uspekhi*. 2024;67:109-128. DOI:10.3367/UFNe.2023.12.039620
5. Bukharov DN, Kucherik AO, Arakelian SM. Nanocluster fractal electrical conductivity in thin films on a solid surface: dimensional models of different configurations and demonstration of results in a laser experiment. *Journal of Advanced Materials and Technology*. 2023;8(3):227-251. DOI:10.17277/jamt.2023.03.pp.227-251
6. Kozhushner MA, Bodneva VL, Trahtenberg LI. Theory of sensory effect in detecting reducing gases. *Zhurnal fizicheskoy khimii = Russian Journal of Physical Chemistry A*. 2012;86(6):1397-1404. (In Russ.)
7. Arakelyan SM, Buharov DN, Kucherik AO, Hudajberganov TA. Dynamic and quantum effects in cluster low-dimensional multilayer solid-state nanostructures for the element base of micro- and nanoelectronics. *Izvestiya Rossiyskoy akademii nauk. Seriya fizicheskaya = Bulletin of the Russian Academy of Sciences: Physics*. 2022;86(6):834-840. (In Russ.)
8. Belysheva TV, Gatin AK, Grishin MV, Ikim MI, et al. Structure and physicochemical properties of nanostructured films of metal oxides - a sensitive layer of gas sensors. *Khimicheskaya fizika = Russian Journal of Physical Chemistry B*. 2015;34(9):56-67. DOI:10.7868/S0207401X15090046 (In Russ.)
9. Kulbachinsky VA. *Physics of nanosystems*. Moscow: Fizmatlit; 2021. 768 p. (In Russ.)
10. Zuev DA, Lotin AA, Novodvorsky OA, Lebedev FV, et al. Pulsed laser deposition of ITO thin films and their characteristics. *Fizika i tekhnika poluprovodnikov = Semiconductors*. 2012;46(3):425-429. (In Russ.)
11. Kozhushner MA, Trakhtenberg LI. Conductivity of composites containing ferromagnetic nanoparticles. The role of the magnetic field. *Zhurnal eksperimental'noy i teoreticheskoy fiziki = Journal of Experimental and Theoretical Physics*. 2010;138(6):1144-1152. (In Russ.)
12. Khorov K, Kochuev D, Chkalov R, Prokoshev V, Arakelian S. Nonlinear dynamic processes in laser-induced transitions to low-dimensional carbon nanostructures in bulk graphite unit. *New Trends in Nonlinear Dynamics – Proceedings of the 1st International Nonlinear Dynamics Conference, NODYCON 2019: 1, Rome, 17-20 February 2019*. Springer Nature: Switzerland; 2020. p.131-140.
13. Gehrke MN, Bukharov DN, Istratov AV, Novikova OA, et al. Study of the structure and electrical conductivity of thin bimetallic granular films. *Izvestiya Rossiyskoy akademii nauk. Seriya fizicheskaya = Bulletin of the Russian Academy of Sciences: Physics*. 2017;81(12):1572-1575. (In Russ.)
14. Trakhtenberg LI, Gerasimov GN, Gromov VF, Belysheva TV, Ilegbusi OJ. Effect of composition on sensing properties of $\text{SnO}_2 + \text{In}_2\text{O}_3$ mixed nano-structured films. *Sensors and Actuators B: Chemical*. 2012;169:32-38. DOI:10.1016/j.snb.2012.01.064
15. Arakelyan SM, Kucherik AO, Prokoshev VG, Rau VG, Sergeev AG. *Introduction to femtonanophotonics. Fundamentals and laser methods for controlled production and diagnostics of nanostructured materials*. Moscow: Logos; 2015. 744 p. (In Russ.)
16. Marukovich EH, Stetsenko VYu, Stetsenko AV. Nanostructured crystallization of metals. *Lit'ye i metallurgiya*. 2021;2:23-26. (In Russ.)
17. Kavokin A, Kutrovskaya S, Kucherik A, Osipov A, et al. The crossover between tunnel and hopping conductivity in granulated films of noble metals. *Superlattices and Microstructures*. 2017;111:335-339. DOI:10.1016/j.spmi.2017.06.050
18. Eletsy AV, Knizhnik AA, Potapkin BV, Kenny HM. Electrical characteristics of polymer composites containing carbon nanotubes. *Uspekhi fizicheskikh nauk = Physics-Uspekhi*. 2015;185:225-270. DOI:10.3367/UFNr.0185.201503a.0225 (In Russ.)
19. Bauhofer W, Kovacs JZ. A review and analysis of electrical percolation in carbon nanotube polymer composites. *Composites Science and Technology*. 2009;69(10):1486-1498. DOI:10.1016/j.compscitech.2008.06.018
20. Eletsy AV. Transport properties of carbon nanotubes. *Uspekhi fizicheskikh nauk = Physics-Uspekhi*. 2009;52(3):209-224. DOI:10.3367/UFNr.0179.200903a.0225 (In Russ.)
21. Cardoso P, Silva J, Paleo AJ, Van Hattum FWJ, et al. The dominant role of tunneling in the conductivity of

carbon nanofiber epoxy composites. *Physica Status Solidi (A)*. 2010;207(2):407-410. DOI:10.1002/pssa.200925334

22. Salvato M, Cirillo M, Lucci M, Orlanducci S, et al. Charge transport and tunneling in single-walled carbon nanotube bundles. *Physical Review Letters*. 2008;101(24):246804. DOI:10.1103/PhysRevLett.101.246804

23. Malinetsky GG, Potapov AB, Podlazov AV. *Nonlinear dynamics. Approaches, results, hopes*. Moscow: URSS; 2016. 280 p. (In Russ.)

24. Grimaldi C, Mionić M, Gaal R, Forró L, Magrez A. Electrical conductivity of multi-walled carbon nanotubes-SU8 epoxy composites. *Applied Physics Letters*. 2013;102(22):223114. DOI:10.1063/1.4809923

25. Arakelian SM, Bucharov DN, Emel'yanov VI, Zimin SP, et al. Bimodal ensemble of nanoparticles on the surface of epitaxial lead telluride films under continuous laser radiation. *Journal of Surface Investigation. X-ray, Synchrotron and Neutron Techniques*. 2015;9(6):1156-1163. DOI:10.1134/S1027451015060063

26. Sarychev AK, Shalaev VM. *Electrodynamics of metamaterials*. Moscow: Scientific world; 2011. 224 p. (In Russ.)

27. Celzard A, McRae E, Deleuze C, Dufort M, et al. Critical concentration in percolating systems containing a high-aspect-ratio filler. *Physical Review B*. 1996;53(10):6209-6214. DOI:10.1103/PhysRevB.53.6209

28. Hu N, Masuda Z, Yamamoto G, Fukunaga H, Hashida T, Qiu J. Effect of fabrication process on electrical properties of polymer/multi-wall carbon nanotube nanocomposites. *Composites Part A: Applied Science and Manufacturing*. 2008;39(5):893-903. DOI:10.1016/j.compositesa.2008.01.002

29. Charlier J-C, Blase X, Roche S. Electronic and transport properties of nanotubes. *Reviews of Modern Physics*. 2007;79(2):677-732. DOI:10.1103/RevModPhys.79.677

30. Terenzi A, Natali M, Petrucci R, Rallini M, et al. Analysis and simulation of the electrical properties of CNTs/epoxy nanocomposites for high performance composite matrices. *Polymer Composites*. 2015;38(1):105115. DOI:10.1002/pc.23565

31. Penazzi G, Carlsson JM, Diedrich C, Olf G, et al. Atomistic modeling of charge transport across a carbon nanotube-polyethylene junction. *The Journal of Physical Chemistry C*. 2013;117(16):8020-8027. DOI:10.1021/jp312381k

32. Pavlushin A, Konogorova DV. Crystallogenic prerequisites for the emergence of a unique form of diamond "Matryoshka" – the effect of capture of a diamond inclusion by a twin of diamond crystals. *Geohimiya*. 2023;68(3):271-284. DOI:10.31857/S001675252303010X (In Russ.)

33. Khorkov KS, Prokoshev VG, Arakelian SM. Laser-induced methods for obtaining carbon nanomaterials in liquid nitrogen under femtosecond radiation. *Journal of Advanced Materials and Technologies*. 2021;6(2):101-112. DOI:10.17277/jamt.2021.02.pp.101-112

34. Mishchenko SV, Tkachev AG. *Carbon nanomaterials. Production, properties, application*. Moscow: Mechanical Engineering; 2008. 320 p. (In Russ.)

35. Ellert OG, Tsodikov MV, Nikolaev SA, Novotortsev VM. Bimetallic nanoalloys in heterogeneous catalysis of industrially important reactions: synergetic effects and structural organization of the active components. *Russian Chemical Reviews*. 2014;83(8):718-732. DOI:10.1070/RC2014v083n08ABEH004432

36. Lu W, Chou T-W, Thostenson ET. A three-dimensional model of electrical percolation thresholds in carbon nanotube-based composites. *Applied Physics Letters*. 2010;96(22):223106. DOI:10.1063/1.3443731

37. Logakis E, Pandis Ch, Peoglos V, Pissis P, et al. Electrical/dielectric properties and conduction mechanism in melt processed polyamide/multi-walled carbon nanotubes composites. *Polymer*. 2009;50(21):5103-5111. DOI:10.1016/j.polymer.2009.08.038

38. Yu Y, Song G, Sun L. Determinant role of tunneling resistance in electrical conductivity of polymer composites reinforced by well dispersed carbon nanotubes. *Journal of Applied Physics*. 2010;108(8):084319. DOI:10.1063/1.3499628

39. Antipov AA, Arakelyan SM, Bukharov DN, Kutrovskaya SV, et al. Laser synthesis of micro-nanoparticles in liquid media. *Khimicheskaya fizika i mezoskopiya*. 2012;14(3):401-407. (In Russ.)

40. Gonsales R, Woods R, Eddins S. *Digital image processing in the MATLAB*. Moscow: Tekhnosfera; 2006. 616 p. (In Russ.)

41. Gonzato G. A practical implementation of the box counting algorithm. *Computers & Geosciences*. 1998;24(1):95-100. DOI:10.1016/S0098-3004(97)00137-4

42. Ryzhikova YuV, Ryzhikov SB. Fractal properties of self-organizing dendritic structures. *Uchenye zapiski fizicheskogo fakul'teta Moskovskogo Universiteta*. 2018;(5):1850401. (In Russ.)

43. Mroczka J, Woźniak M, Onofri FRA. Algorithms and methods for analysis of the optical structure factor of fractal aggregates. *Metrology and Measurement Systems*. 2012;19(3):359-370. DOI:10.2478/v10178-012-0039-2

44. Lobanov AI. Models of cellular automata. *Komp'yuternyye issledovaniya i modelirovaniye*. 2010;2(3):273-293. (In Russ.)

45. Samarskiy AA, Vabishchevich PN. *Computational heat transfer*. Moscow: URSS; 2020. 784 p. (In Russ.)

46. Bukharov DN. Thermal diffusion model of a system of lead telluride nanoclusters. *Nanoelectronics, nanophotonics and nonlinear physics. Collection of works of the XVIII All-Russian Conference of Young Scientists*. Saratov: "Techno-Décor" publ. house; 2023. 227 p. (In Russ.)

47. Nechaev, YS. On the nature, kinetics and limiting values of hydrogen sorption by carbon nanostructures. *Uspekhi ifizicheskikh nauk = Physics-Uspekhi*. 2006;176(6):581-610. DOI:10.3367/UFNr.0176.200606b.0581 (In Russ.)

48. Prudnikov M, Linnik AI, Shalaev RV, Rumyantsev VV, et al. Features of the formation and modification of nanostructured carbon nitride films. *Nanosistemy: fizika, khimiya, matematika*. 2012;3(6):134-145. (In Russ.)

49. Ampilova NB. Algorithms for fractal image analysis. *Komp'yuternyye instrumenty v obrazovanii*. 2012;(2):19-24. (In Russ.)
50. Bukharov DN, Arakelyan SM, Kucherik AO, Novikova OA, Samyshkin VD. Mathematical modeling of the structure and optical properties of the fractal island metal nanofilm. *Journal of Physics: Conference Series*. 2020;1439(1):012050. DOI:10.1088/1742-6596/1439/1/012050
51. Belankov AB, Stolbov VYu. Application of cellular automata for modeling the microstructure of a material during crystallization. *Sibirskiy Zhurnal industrial'noy matematiki = Journal of Applied and Industrial Mathematics*. 2005;8(2(22)):12-19. (In Russ.)
52. Dong X, Oganov AR, Cui H, Zhou X-F, Wang H-T. Electronegativity and chemical hardness of elements under pressure. *Proceedings of the National Academy of Sciences*. 2022;119(10):e2117416119. DOI:10.1073/pnas.2117416119
53. Berghoff D, Bühler J, Bonn M, Leitenstorfer A, et al. Low-field onset of Wannier-Stark localization in a polycrystalline hybrid organic inorganic perovskite. *Nature Communications*. 2021;12(1):5719. DOI:10.1038/s41467-021-26021-4
54. Frey P, Rachel S. Realization of a discrete time crystal on 57 qubits of a quantum computer. *Science Advances*. 2022;8(9):eabm7652. DOI:10.1126/sciadv.abm7652
55. Sun L-H, Ounaies Z, Gao X-L, Whalen CA, Yang Z-G. Preparation, characterization, and modeling of carbon nanofiber/epoxy nanocomposites. *Journal of Nanomaterials*. 2011;2011:1-8. DOI:10.1155/2011/307589
56. Magomedov MN. On the baric fragmentation of a crystal. *Physics of the Solid State*. 2003;45(5):908-910. DOI:10.1134/1.1575343
57. Arakelian S, Kutrovskaya S, Kucherik A, Osipov A, et al. Laser-induced synthesis of nanostructured metal-carbon clusters and complexes. *Optical and Quantum Electronics*. 2016;48(11):505. DOI:10.1007/s11082-016-0776-7
58. Cannella CB, Goldman N. Carbyne fiber synthesis within evaporating metallic liquid carbon. *The Journal of Physical Chemistry C*. 2015;119(37):21605-21611. DOI:10.1021/acs.jpcc.5b03781
59. Kutrovskaya SV, Arakelian SM, Kucherik AO, Osipov AV, Garnov SV. Long linear carbon chain – laser-induced structures and possible applications. *Laser Physics*. 2019;29(8):085901. DOI:10.1088/1555-6611/ab183a
60. Kucherik AO, Arakelyan SM, Garnov SV, Kutrovskaya SV, et al. Two-step laser-induced synthesis of linear carbon chains. *Kvantovaya elektronika = Quantum Electronics*. 2016;46(7):627-633. (In Russ.)
61. Landau LD, Lifshits EM. *Theoretical physics*. Statistical physics. Moscow: Fizmatlit; 2002. 616 p. (In Russ.)
62. Kutrovskaya S, Samyshkin V, Lelekova A, Povolotskiy A, et al. Field-Induced assembly of *sp-sp*² carbon sponges. *Nanomaterials*. 2021;11(3):763. DOI:10.3390/nano11030763
63. Wang Q, Shen Y, Pan B, Hao Y, et al. Strong interplay between stripe spin fluctuations, nematicity and superconductivity in FeSe. *Nature Materials*. 2016;15(2):159-163. DOI:10.1038/nmat4492
64. Kucherik A, Arakelian S, Vartanyan T, Kutrovskaya S, et al. Laser-induced synthesis of metal – carbon materials for implementing surface-enhanced Raman scattering. *Optics and Spectroscopy*. 2016;121(2):263-270. DOI:10.1134/S0030400X16080105
65. Downer MC, Ahn H, Reitze DH, Wang XY. Dielectric function and electrical resistivity of liquid carbon determined by femtosecond spectroscopy. *International Journal of Thermophysics*. 1993;14(3):361-370. DOI:10.1007/BF00566036
66. Arakelian SM, Kucherik AO, Khudaberganov TA, Bukharov DN, et al. Nanophysics in laser-induced cluster systems: topological quantum states in electrical conductivity and features of optical spectra – theory and experiment for dimensional effects. *Optical and Quantum Electronics*. 2020;52(4):202. DOI:10.1007/s11082-020-02308-6
67. Kucherik AO, Osipov AV, Arakelian SM, Garnov SV, et al. The laser-assisted synthesis of linear carbon chains stabilized by noble metal particle. *Journal of Physics: Conference Series*. 2019;1164:012006. DOI:10.1088/1742-6596/1164/1/012006
68. Forgerini FL, Marchiori R. A brief review of mathematical models of thin film growth and surfaces: A possible route to avoid defects in stents. *Biomatter*. 2014;4(1):e28871. DOI:10.4161/biom.28871
69. Bukharov DN, Kucherik AO, Arakelyan SM, Lotin AA. Modeling of a profile of a PbTe semiconductor nanofilm. *Journal of Physics: Conference Series*. 2019;1331(1):012002. DOI:10.1088/1742-6596/1331/1/012002
70. Family F, Vicsek T. Scaling of the active zone in the Eden process on percolation networks and the ballistic deposition model. *Journal of Physics A: Mathematical and General*. 1985;18(2):L75-L81. DOI:10.1088/0305-4470.18.2.005
71. Moskalev PV. Analysis of the structure of a percolation cluster. *Zhurnal tekhnicheskoy fiziki = Technical Physics*. 2009;79(6):1-7. (In Russ.)
72. Kucherik A, Samyshkin V, Prusov E, Osipov A, et al. Formation of fractal dendrites by laser-induced melting of aluminum alloys. *Nanomaterials*. 2021;11(4):1043. DOI:10.3390/nano11041043
73. Sander LM. Diffusion-limited aggregation: A kinetic critical phenomenon. *Contemporary Physics*. 2000;41(4):203-218. DOI:10.1080/001075100409698
74. Jagota M, Tansu N. Conductivity of nanowire arrays under random and ordered orientation configurations. *Scientific Reports*. 2015;5(1):10219. DOI:10.1038/srep10219
75. Chu ChSh. Computer modeling of thin film growth processes during thermal vacuum deposition. *Izvestiya Vuzov Rossii. Radioelektronika*. 2016;6:22-31. (In Russ.)
76. Kuzmicheva GM. Nanosized systems with titanium (IV) oxides. Receipt. Characterization. Properties. *Tonkiye khimicheskkiye tekhnologii*. 2015;10(6):5-36. (In Russ.)

77. Savin AV, Sakovich RA, Mazo MA. Using spiral chain models for study of nanoscroll structures. *Physical Review B*. 2018;97(16):165436. DOI:10.1103/PhysRevB.97.165436

78. Kulagin AE, Shapovalov AV. Analytical description of the diffusion in a cellular automaton with the Margolus neighbourhood in terms of the two-dimensional Markov chain. *Mathematics*. 2023;11(3):584. DOI:10.3390/math11030584

79. Bukharov DN, Skryabin IO, Arakelyan SM. Model of the microscroll structure. *Journal of Physics: Conference Series*. 2019;1331(1):012019. DOI:10.1088/1742-6596/1331/1/012019

80. Burlakov RB, Kovivchak VS. On the issue of measuring the resistivity of conductive layers using the four-probe method. *Vestnik Omskogo Universiteta*. 2014;2(72):59-68. (In Russ.)

81. Apostolova T, Kurylo V, Gnilitskiy I. Ultrafast laser processing of diamond materials: A Review. *Frontiers in Physics*. 2021;9:650280. DOI:10.3389/fphy.2021.650280

82. Tikhomirov S, Kimstach T. Raman spectroscopy – a promising method for studying carbon nanomaterials. *Analitika*. 2011;(6):28-32. (In Russ.)

83. Shimizu M, Shimotsuma Y, Sakakura M, Yuasa T, et al. Periodic metallo-dielectric structure in diamond. *Optics Express*. 2009;17(1):46-54. DOI:10.1364/OE.17.000046

84. Kononenko TV, Komlenok MS, Pashinin VP, Pimenov SM, et al. Femtosecond laser microstructuring in the bulk of diamond. *Diamond and Related Materials*. 2009;18(2-3):196-199. DOI:10.1016/j.diamond.2008.07.014

85. Kononenko TV, Konov VI, Pimenov SM, Rossukanyi NM, et al. Three-dimensional laser writing in diamond bulk. *Diamond and Related Materials*. 2011;20(2):264-268. DOI:10.1016/j.diamond.2010.12.013

86. Sun B, Salter PS, Booth MJ. High conductivity micro-wires in diamond following arbitrary paths. *Applied Physics Letters*. 2014;105(23):231105. DOI:10.1063/1.4902998

87. Shimotsuma Y. Three-dimensional nanostructuring of transparent materials by the femtosecond laser irradiation. *Journal of Laser Micro/Nanoengineering*. 2006;1(3):181-184. DOI:10.2961/jlmn.2006.03.0006

88. Lagomarsino S, Bellini M, Corsi C, Fanetti S, et al. Electrical and Raman-imaging characterization of laser-made electrodes for 3D diamond detectors. *Diamond and Related Materials*. 2014;43:23-28. DOI:10.1016/j.diamond.2014.01.002

89. Kulnitsky BA, Perezhogin IA, Blank VD. Polytypes and twins in the diamond – lonsdaleite system. *Izvestiya vysshikh uchebnykh zavedeniy. Seriya Khimiya i khimicheskaya tekhnologiya = ChemChemTech*. 2015;5(58):48-50. (In Russ.)

90. Ying P, Gao Y, Zhang B, Wu Y, et al. Synthesis of twin-structured nanodiamond particles. *AIP Advances*. 2020;10(1):015240. DOI:10.1063/1.5141035

Different DLA calculation schemes with Moore and/or von Neumann Neighborhoods

P.1. Algorithm for fiber model construction

The algorithm for constructing the fiber model in the DLA approach was developed from the following steps (Fig. P.1): (1) At the initialization stage, a starting structure consisting of a system of seed particles located on the lower boundary was generated within the calculation area with a uniform grid, and the fiber size (maximum number of particles in the calculation area) was set; (2) A specified number of particles were generated at the upper boundary of the calculation area; (3) These particles performed random shifts downward and sideways with equal or different probabilities; (4) If they approached an occupied cell within the Moore neighborhood (Fig. P.1b), they aggregated with the occupied cell; otherwise, they continued moving; (5) Steps 2-4 were repeated.

The criterion for stopping the iterative process was the fiber reaching the required size, when the number of particles in the calculation area reached the set value, or when the nanowire reached the upper boundary of the calculation area.

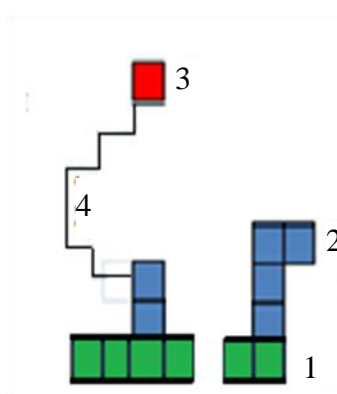


Fig. P.1a. DLA fiber model calculation scheme: 1 – starting structure, 2 – aggregated particles, 3 – new particle, 4 – random shifts. Explanations are provided in the text

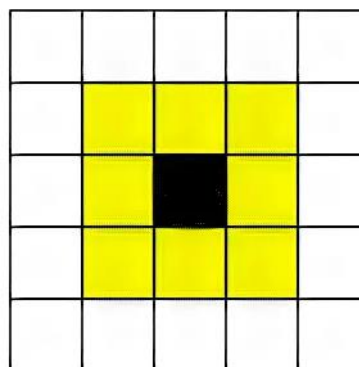


Fig. P.1b. Moore neighborhood of 8 objects

P.2. Two models of growth over inhomogeneity – random growth during particle deposition in percolation

To describe the algorithm, two functions are used: the average surface height $\overline{h(t)}$, which defines the baseline position for the surface of the sample being studied, and its roughness, $W(t)$.

In the first random growth model, all growth columns are filled randomly (Fig. P.2a). Then, after the random deposition of N particles, the height of the deposited structure h can be calculated using the equation:

$$h = \sqrt{Nf(1-f) + (Nf)^2},$$

where $f = 1/L$ is the probability of filling a given column, and L is the width of the calculation area, i.e., $h^i = h^{i-1} + 1$, where i is the time step [68].

In the other model of ballistic percolation deposition, a particle is fixed at the point of first contact with the already deposited structure, following the nearest neighbor rule (Fig. P.2b). In this case, the height is determined by the heights of the nearest left and right columns, and the height is calculated as the maximum of the neighboring columns' heights:

$$h_j = \max\{h_{j-1}, h_j + 1, h_{j+1}\},$$

where j is the number of the column being considered [69]. Unlike the previous model (Fig. P.2a), in this case, the particle can attach to the side surface of the already formed structure (Fig. P.2a) [70]. This means that the possibility of growth along the local normal to the surface is considered, which can lead to the expansion of local protrusions on the growth front surface, thus enhancing surface growth in the lateral direction.

The percolation structure is represented as a square grid of size $m \times m$ a. u. The cells of this grid contain either 0 (empty site) or 1 (occupied site). Each cell in the model is occupied by a particle with probability s , independent of the state of neighboring cells. For each grid cell, a random number α is generated. If $\alpha \leq s$, the value in the cell is set to 1; otherwise, it is 0 (cf. with [71]). Here, the parameter s represents the percolation threshold, above which a particle is not fixed in the cell.

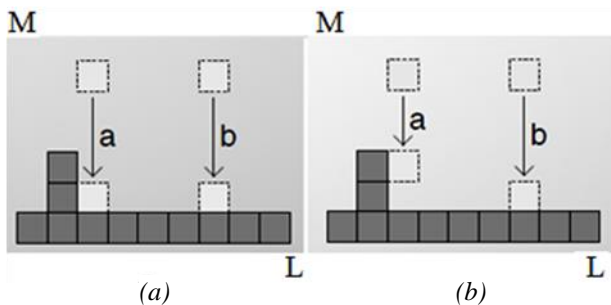


Fig. P.2. Diagram of both (a) Random and (b) Ballistic the deposition processes for Deposited Particles – also, the moving particles labeled as letters both a and b

P.3. DLA model in the iterative algorithm

The initial state of the system was described by placing model particles, such as Au particles, along the lower boundary, serving as aggregation centers. Each iteration began by introducing a new model particle into the calculation area. The particle was introduced at a random location along the upper boundary, within its central third. This simulates the experiment where a laser beam with a diameter of 1/3 of the calculation area length is applied. Then, the standard DLA procedure was followed (Fig. P.3).

The random walk of the particle occurred from the upper boundary of the calculation area, where a notional cathode was located, to the lower boundary, where a notional anode was located. If an occupied area appeared in the Moore neighborhood of the wandering particle, it would aggregate with that area with a given probability.

To describe the random walk, a uniform grid was applied to the calculation area. Thus, the random walk was formed by a series of single-cell movements across the calculation area with a specified probability. Periodic boundary conditions were used along the sides, causing the particle to reflect off them. At the lower boundary, an adhesion condition was applied, fixing the particle in place. Varying the probabilities of individual random movements allowed for consideration of growth direction. Aggregation of the wandering particle occurred with a given probability when it encountered an occupied cell in the Moore neighborhood. In terms of physics, the aggregation probability can be understood as a conditional surface tension coefficient in the system, inversely proportional to temperature, normalized to the phase transition temperature [73].

To model experimental samples, a random nanowire model was proposed [74], where a system of random lines of equal thickness was generated on a two-dimensional calculation area. Each line was assigned a random length L from the interval $[L_{min}; L_{max}]$; the area had a width w . A line was defined by two points (x_1, y_1) and (x_2, y_2) with random coordinates as follows:

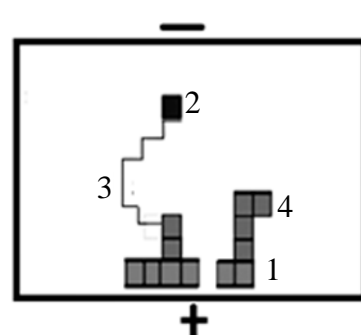


Fig. P.3. Model Diagram (One Iteration of the DLA Process):
 1 – Au particles, 2 – C chain, 3 – its random walk,
 4 – previously formed structure.
 The signs (+) and (-) correspond to the direction of the applied external electric field

$$\begin{aligned}
 x_c &= rw; & y_c &= rL; & \theta &= 2\pi r; \\
 x_2 &= x_c + L\cos(\theta)/2; & y_2 &= y_c + L\sin(\theta)/2; \\
 x_1 &= x_c - L\cos(\theta)/2; & y_1 &= y_c - L\sin(\theta)/2,
 \end{aligned}$$

where r is a random number with a uniform distribution, and θ is the angle of rotation of the wire segment.

P.4. Model for an individual microsponge

Figure P.4 presents calculations based on the proposed model: laser radiation was assumed to act on the lower boundary, where the anode (charge (+)) was located. Objects of different sizes were generated, moving with a given speed toward the upper boundary, where the cathode (charge (-)) was located.

The calculation area was conventionally divided into three subregions: two with a side length of 33 a. u., and the uppermost one with a length of 34 relative units. In these areas, the object movement speeds decreased to 3 a. u., 2 a. u., and 1 relative a. u., respectively. The probability of object merging was 20 %. The sizes of the model objects

varied from 1 to 5 a. u. For example, Fig. P.4a shows the case of forming a sponge from small elements; Fig. P.4b illustrates the formation of individual elongated threads; in Fig. P.4c, several small sponges are generated; and in Fig. P.4d, most objects have merged into one large elongated sponge.

P.5. Helicoidal structure model

The diffusion model of a helicoidal structure was based on solving the diffusion equation in a discrete area using cellular automaton techniques [78]. The structure was synthesized iteratively, starting from an initial shape, where a cell in the calculation area would become occupied with a given probability if it had a neighboring occupied cell within the Moore neighborhood (considering 8 adjacent cells, as shown in Fig. P.5). The main parameter of the model was the probability of a cell being occupied. This relative model parameter can be related to a physical parameter of the system, such as the intensity of an external magnetic field in the corresponding experimental geometry.

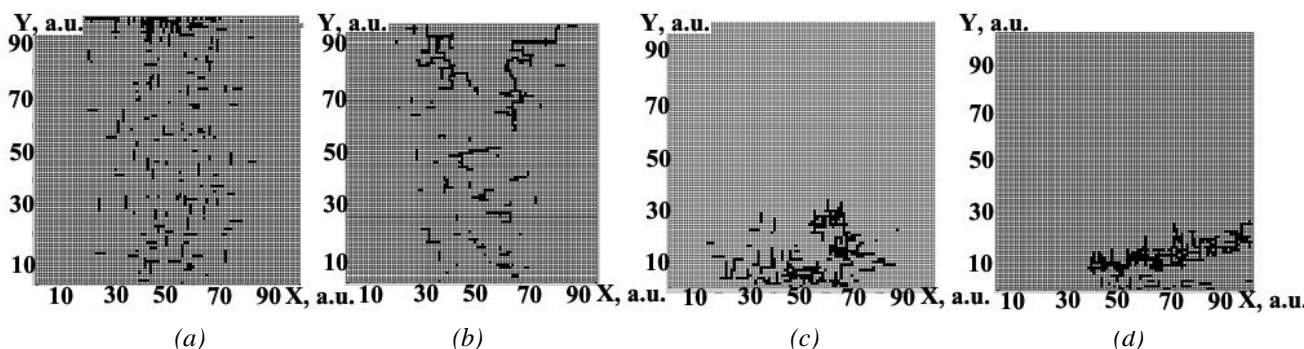


Fig. P.4. Model of a sponge system made from individual threads (in the horizontal plane relative to the boundary): a system of small sponges made of short threads, located near the upper boundary of the calculation area (a); a system of vertically elongated sponges, made of individual long threads, localized near the upper boundary of the calculation area (b); a system of small sponges with a relatively uniform structure, localized near the lower boundary of the calculation area (c); a system of sponges made from one large elongated object, located near the lower boundary of the calculation area (d)

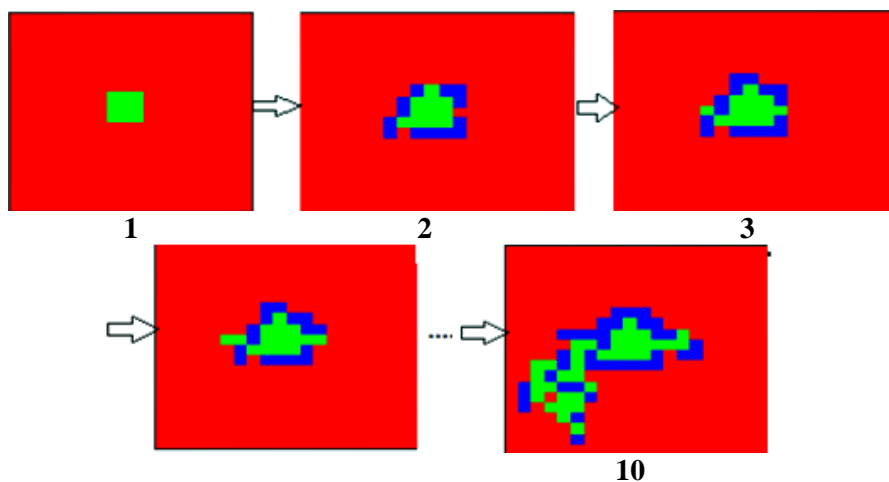


Fig. P.5. Model diagram: the resulting helical structure after performing 1–10 iterations, starting from the initial shape numbered 1 (explanations are provided in the text).

Information about the authors / Информация об авторах

Dmitry N. Bukharov, Cand. Sc. (Phys. and Math.), Associate Professor, Vladimir State University (VLSU), Vladimir, Russian Federation; ORCID 0000-0002-4536-8576; e-mail: buharovdn@gmail.com

Darya D. Tumarkina, Teaching Assistant; VISU, Vladimir, Russian Federation; ORCID 0009-0007-5496-4234; e-mail: tumarkina.darya@mail.ru

Alexey O. Kucherik, D. Sc. (Phys. and Math.), Associate Professor, Vice-Rector for Research and Digital Development, VISU, Vladimir, Russian Federation; ORCID 0000-0003-0589-9265; e-mail: kucherik@vlsu.ru

Alexey G. Tkachev, D. Sc. (Eng.), Professor, Head of the Department, Tambov State Technical University (TSTU), Tambov, Russian Federation; ORCID 0000-0001-5099-9682; e-mail: nanotam@yandex.ru

Sergei M. Arakelian, D. Sc. (Phys. and Math.), Professor, Independent Researcher, Vladimir, Russian Federation; ORCID 0000-0002-6323-7123; e-mail: arak@vlsu.ru

Irina V. Burakova, Cand. Sc. (Eng.), Associate Professor, TSTU, Tambov, Russian Federation; ORCID 0000-0003-0850-9365; e-mail: iris_tamb68@mail.ru

Alexander E. Burakov, Cand. Sc. (Eng.), Associate Professor, TSTU, Tambov, Russian Federation; ORCID 0000-0003-4871-3504; e-mail: m-alex1983@yandex.ru

Бухаров Дмитрий Николаевич, кандидат физико-математических наук, доцент, Владимирский государственный университет имени А. Г. и Н. Г. Столетовых (ВлГУ), Владимир, Российская Федерация; ORCID 0000-0002-4536-8576; e-mail: buharovdn@gmail.com

Тумаркина Дарья Денисовна, ассистент преподавателя, ВлГУ, Владимир, Российская Федерация; ORCID 0009-0007-5496-4234; e-mail: tumarkina.darya@mail.ru

Кучерик Алексей Олегович, доктор физико-математических наук, доцент, проректор по научной работе и цифровому развитию, ВлГУ, Владимир, Российская Федерация; ORCID 0000-0003-0589-9265; e-mail: kucherik@vlsu.ru

Ткачев Алексей Григорьевич, доктор технических наук, профессор, заведующий кафедрой, Тамбовский государственный технический университет (ТГТУ), Тамбов, Российская Федерация; ORCID 0000-0001-5099-9682; e-mail: nanotam@yandex.ru

Аракелян Сергей Мартиросович, доктор физико-математических наук, профессор, независимый исследователь, Владимир, Российская Федерация; ORCID 0000-0002-6323-7123; e-mail: arak@vlsu.ru

Буракова Ирина Владимировна, кандидат технических наук, доцент, ТГТУ, Тамбов, Российская Федерация; ORCID 0000-0003-0850-9365; e-mail: iris_tamb68@mail.ru

Бураков Александр Евгеньевич, кандидат технических наук, доцент, ТГТУ, Тамбов, Российская Федерация; ORCID 0000-0003-4871-3504; e-mail: m-alex1983@yandex.ru

Received 30 April 2024; Accepted 28 June 2024; Published 22 October 2024



Copyright: © Bukharov DN, Tumarkina DD, Kucherik AO, Tkachev AG, Arakelyan SM, Burakova IV, Burakov AE, 2024. This article is an open access article distributed under the terms and conditions of the Creative Commons Attribution (CC BY) license (<https://creativecommons.org/licenses/by/4.0/>).

Территория распространения – Российская Федерация, зарубежные страны
Distributed in the Russian Federation and foreign countries

Computer layout: Olga V. Mochalina, TSTU, Tambov, Russian Federation
Компьютерный дизайн и верстка: Мочалина О. В., ТГТУ, Тамбов, Россия

Оригинал-макет подготовлен в Издательском центре ФГБОУ ВО «ТГТУ»,
392032, Тамбовская обл., г. Тамбов, ул. Мичуринская, д. 112А

Подписано в печать 04.10.2024. Дата выхода в свет 22.10.2024.
Формат 60×90/8. Усл. печ. л. 10,50. Уч.-изд. л. 10,75. Тираж 100 экз. Цена свободная. Заказ № 025.
СМИ журнал “Journal of Advanced Materials and Technologies”
(Журнал современных материалов и технологий) выпуск 2024. Том 9, № 3

Материалы журнала доступны по лицензии Creative Commons “Attribution” («Атрибуция») 4.0 Всемирная (CC BY 4.0)
All the materials of the “Golden Horde Review” are available under the Creative Commons License “Attribution” 4.0 International (CC BY 4.0)

